Positron and Positronium Interactions with Atoms and Molecules

A thesis submitted to the University College London for the degree of
Doctor of Philosophy

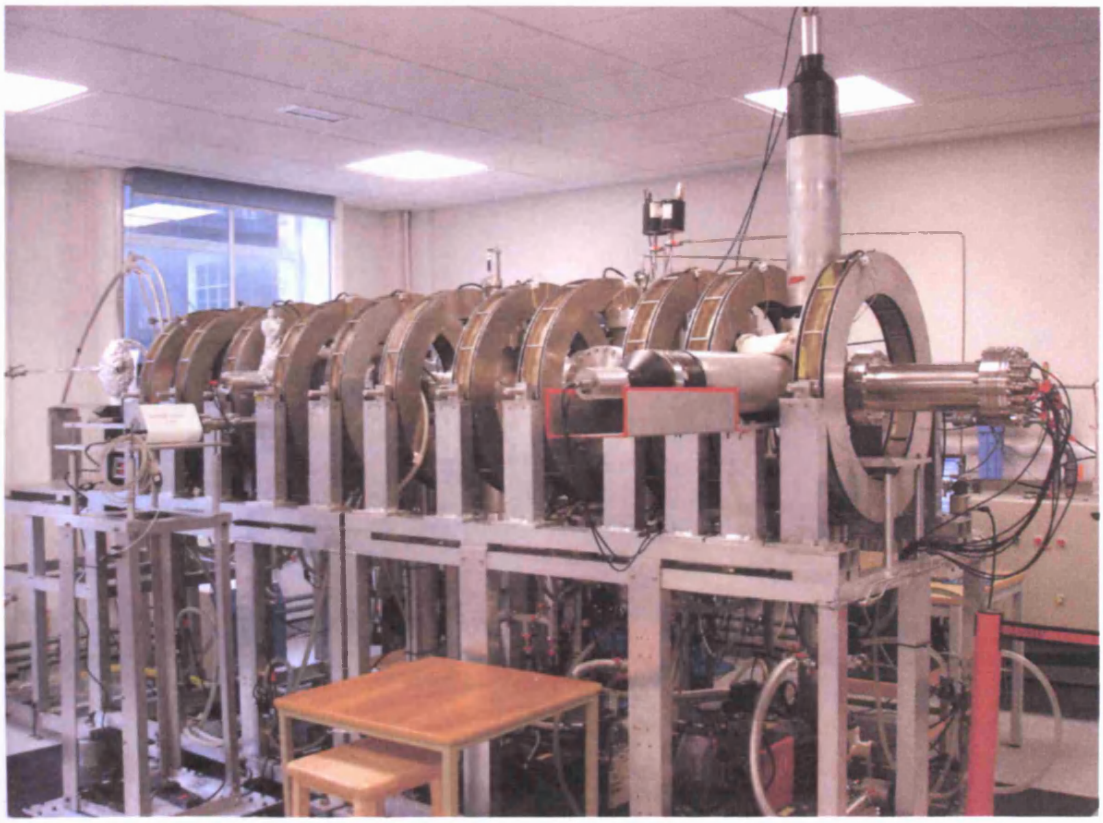

Josephine Erica Beale
Department of Physics and Astronomy
University College London

November 2007

ProQuest LLC
789 East Eisenhower Parkway
P.O. Box 1346
Ann Arbor, MI 48106-1346

Acknowledgments

I would like to thank my supervisor Prof. Nella Laricchia for giving me guidance during my PhD and for enabling me to have this opportunity to investigate a fundamental atom and work with some great people. I would also like to thank Dan Murtagh, Simon Brawley, Dave Cooke, Dr Dawn Leslie and Dr Cristiana Arcidiacono with whom I have shared an office over the past few years for being there and giving me a helping hand when I have needed it, especially Dr Dawn Leslie and Dr Cristiana Arcidiacono. I would like to extend my thanks to Dr Simon Armitage who was the Post Doc when I first started, for teaching me the fundamentals of working with the positronium beam.

Thanks go to Dr Dawn Leslie, Dr Cristiana Arcidiacono and Dr Andrew Garner for proof reading my thesis and to Rafid Jawad for his help with electronic equipment. Finally, I would like to thank my husband David Coltman, my Gran, my Dad, my Brother and my husband's family, as well as my friends, for the support they have given me while doing this PhD. I would especially like to thank David for reading through the chapters.

Abstract

Positronium is the lightest known atom, consisting of an electron and its antiparticle the positron. Because of its light mass (comparable with that of the electron and positron, rather than conventional atoms), recoil effects are expected to play an important role in its scattering from atomic and molecular targets.

Up until recently positronium beam experiments have been restricted to total cross-section measurements from simple target atoms and molecules i.e. molecular hydrogen, molecular nitrogen, helium and argon where trends have been noted. Therefore, the aim of the project has been to look at more complex targets to supplement existing data and to investigate further positronium total cross-section measurements for molecular oxygen and xenon started by Garner *et al* (1998) and Leslie (PhD thesis, 2005), as well as to compare with corresponding data for other projectiles and theoretical determinations. This has been achieved by looking at neon, xenon, molecular oxygen and water. The total cross-section for positron-water has also been measured in order to investigate the general performance of the system in the presence of water vapour.

Also, as an extension of the fragmentation study by Armitage *et al* (2002) and Leslie (2005), the yields of residual electrons and positrons from positronium-xenon impact at an energy of 30eV have been examined to ascertain contributions from target ionization. Both the integrated cross-section and longitudinal energy distributions have been measured.

Finally, due to the lack of data for water interacting with positrons and positronium, and to complete the work of Arcidiacono (PhD thesis, 2006), both doubly differential ionization cross-sections of water molecules by 100 and 153eV positron impact and total cross-sections of water molecules for positronium impact have been measured.

Contents

Heading			Page number
Acknowledgments			2
Abstract			3
Contents			4
Figure Captions			8
Table Captions			15
Chapter 1: Introduction			16
1.1	Historical Background		16
1.2	Fundamental Properties of Positrons and Positronium		17
	1.2.1	Positrons	17
	1.2.2	Positronium	19
1.3	Early Techniques		21
	1.3.1	Lifetime technique	21
	1.3.2	ACAR	22
	1.3.3	Doppler Broadening	22
1.4	Slow Positron Beam Development		23
	1.4.1	Positrons in Solids	24
	1.4.2	Positron Moderators	25
1.5	Positron Interactions with Atoms and Molecules		27
1.6	Positronium Interactions with Atoms and Molecules		32
	1.6.1	Development of Positronium Beams	32
	1.6.2	Positronium Scattering from Atoms and Molecules	34
	1.6.3	Fragmentation of Positronium in Collision with Helium Atoms	37
1.7	Motivation for Present Work		41
Chapter 2: Positronium Beam Techniques			42
2.1	Introduction		42
2.2	Positron Beam Production		44
	2.2.1	Positron Source	44
	2.2.2	Cryostat and Moderator Arrangement	44
	2.2.3	Procedure for Growing Rare Gas Solid Moderators	45

2.2.4	Energy Spread of Argon Moderated Positron Beam	49
2.3	Transporting the Positron Beam	50
2.3.1	Magnetic Field	50
2.3.2	Wien Filter	51
2.4	Vacuum System	52
2.4.1	Source Region	52
2.4.2	Experimental Region	53
2.4.3	Vacuum System Protection	54
2.5	Positronium Beam Production	54
2.5.1	Introduction	54
2.6	Experimental Region	55
2.6.1	Gas Cells	55
2.6.2	CEMA (end-of-flight detector)	56
2.6.3	Gamma-Ray Detectors	57
2.7	Electronic Circuits for the Detection of Positrons and Positronium	58
2.7.1	CEMA/NaI Coincidence Detection System	58
Chapter 3: Positronium and Positron Total Cross-Sections		61
3.1	Introduction	61
3.2	Experimental Methods	61
3.2.1	Method for Ps-O_2, Ne and Xe	62
3.2.2	Method for e^+-H_2O and Ps-H_2O	62
3.3	Length of the Effective Scattering Cell	64
3.3.1	Cell Length for O_2, Ne and Xe	64
3.3.2	New Scattering Cell and Cell Length for H_2O	67
3.4	Results, Comparisons and Discussion	68
3.4.1	Ne	68
3.4.2	O_2	70
3.4.3	Xe	73
3.4.4	e^+-H_2O	76
3.4.5	Ps-H_2O	79
3.4.6	Comparison of Ps Total Cross-Sections for the Inert Atoms	81
3.4.7	Comparison of Ps Total Cross-Sections for the Molecular Gases	82
3.4.8	Comparison of Ps Total Cross-Sections with Available Theories and Momentum Transfer Cross-Sections	83

3.4.9 Comparison of Ps Total Cross-Sections with those of H Atom, e^+ and e^- 84
3.5 Summary 87
Chapter 4: Projectile Fragmentation and Target Ionization Cross-Sections by Positronium Impact 88
4.1 Introduction 88
4.2 Scattering Cell for Fragmentation and Target Ionization Studies 89
4.3 Method for Determining the Longitudinal Energy Distributions of e^- and e^+ from Ps-Xe Collisions 92
4.4 Method for Determining Integrated Cross-Sections for Ps Fragmentation and Target Ionization 97
4.5 Results and Comparison with Theory 101
4.5.1 Longitudinal Energy Distributions 101
4.5.2 Integrated Cross-Section 104
4.6 Summary 105
Chapter 5: Doubly Differential Ionization Cross-Sections for Positrons in Collision with H_2O Molecules 106
5.1 Introduction and Motivation 106
5.2 Positron Beam Production 109
5.2.1 Introduction 109
5.2.2 Positron Source and Tungsten Moderator 109
5.2.3 Transporting the Positron Beam 111
5.2.4 Vacuum System 112
5.3 Detection of Positrons and Ions 113
5.3.1 Introduction 113
5.3.2 Tandem Parallel Plate Analyzer 113
5.3.3 Channeltron (CEM1) 115
5.3.4 Energy Calibration for the Parallel Plate Analyzer 115
5.3.5 Ion Extractor and Gas Inlet 117
5.4 Electronics and Experimental Method 121
5.5 Results 123
5.6 Summary 127
Chapter 6: Conclusions and Outlook 128
6.1 Summary and Conclusions 128
6.2 Outlook and Suggestions for Future Work 130

Appendix A: Determination of Detection Probability of Forward Scattered Positrons 131

Appendix B: CPO Simulation of the Scattering Cell used for Positronium Fragmentation Studies 134

References 136

Figure Captions

Figure Caption — Page number

Chapter 1: Introduction

Figure 1.1: 16

An early cloud chamber photograph, taken by Anderson (1932a), which revealed the existence of the positron.

Figure 1.2: 18

Feynmann diagrams of a) one, b) two, c) three and d) four gamma-ray decay modes.

Figure 1.3: 20

Energy distribution of gamma-rays emitted from o-Ps annihilation.

Figure 1.4: 21

Energy level diagrams for hydrogen and positronium.

Figure 1.5: 21

Decay scheme for ^{22}Na.

Figure 1.6: 23

Energy distribution of positrons emitted from a ^{22}Na source and a tungsten moderator (centred at 3eV).

Figure 1.7: 25

Simplified illustration of the interaction of positrons near the surface of a metal.

Figure 1.8: 26

The single-particle potential for a thermalized positron near a metal surface, where V_{corr} is due to the conduction electrons and V_0 is due to the ion cores.

Figure 1.9: 27

Conical geometry for a source and moderator arrangement.

Figure 1.10: 29

Schematic illustration of the behaviour of total scattering cross-sections for positron and electron impact with xenon.

Figure 1.11: 31

Doubly differential ionization cross-sections for positrons scattered at ~0° after collision between a) 100eV positrons and argon and b) 150eV positrons and argon.

Figure 1.12: 31

TDCS for electrons scattered at ~0° after collision between 100eV positrons and molecular hydrogen: hollow squares – Kövér *et al* (1998); curves – Berakdar (1998) folded with the experimental resolutions. The curve labeled "without capture" is also shown. The inset shows the experimental results in a linear plot.

Figure 1.13: 34

Positronium beam production efficiency measurements for H_2 – Garner *et al* (1996) and N_2 – Leslie *et al* (2002).

Figure 1.14: 35

Available experimental and theoretical data for the total and momentum transfer cross-section of positronium in collision with N_2, Ar, H_2 and He.

Figure 1.15: 38

Theoretical data for the absolute differential cross-section for the residual positrons and electrons from positronium in collision with helium atoms at 33eV.

Figure 1.16: 39

Experimental and theoretical values for the fragmentation cross-section of positronium in collision with helium atoms.

Figure 1.17: 40

Experimental and theoretical data for the absolute differential cross-section for the residual positrons from positronium in collision with helium atoms.

Chapter 2: Positronium Beam Techniques

Figure 2.1: 43

Schematic of the positronium beamline.

Figure 2.2: 44

Schematic of the cold head and cold finger.

Figure 2.3: 46

Example of an Ar solid moderator.

Figure 2.4: 48

Examples of solid Ar moderators with a surface coating of: a) air and b) see legend for coatings.

Figure 2.5: 49

Normalized e^+-beam energy-profiles for the coated solid Ar moderators as per legend.

Figure 2.6: 50

a) An example of a slow e^+ beam energy profile and b) an Ar moderator energy profile distribution.

Figure 2.7: 52
Schematic of the Wien Filter.
Figure 2.8: 53
Schematic of the Ps beam vacuum system.
Figure 2.9: 56
Schematic of the gas cells: scattering cell shown is for total cross-section measurements.
Figure 2.10: 57
Schematic of CEMA.
Figure 2.11: 57
Schematic diagram of the position of the NaI detector with respect to CEMA.
Figure 2.12: 59
Block diagram of the electronics for the CEMA/NaI coincidence detection system.
Figure 2.13: 60
Typical CEMA/NaI coincidence spectra for a) incident e^+ beam, b) incident Ps beam and c) background.
Chapter 3: Positronium and Positron Total Cross-Sections
Figure 3.1: 64
A schematic diagram of the setup used to purify the distilled H_2O.
Figure 3.2: 66
a) An example of a e^+ beam energy profile for V_s=57V and b) corresponding e^+-Ne total cross-section. Insets are expanded regions of interest.
Figure 3.3: 67
Example of a plot used for the determination of the effective length for the scattering cell for Ne with V_s=57V and CR1, R2=64V.
Figure 3.4: 68
A schematic diagram of the scattering cell used for Ps-H_2O and e^+-H_2O total cross-sections without the apertures. The dotted lines represent the internal diameters. Inset shows the arrangement for the cells.
Figure 3.5: 69
Cross-sections for Ps scattering from Ne.
Figure 3.6: 70
Total cross-section for Ps, e^+ and e^- scattering from Ne.
Figure 3.7: 71

Total cross-section for Ps, e^+ and e^- scattering from O_2.

Figure 3.8: 74

Cross-sections for Ps scattering from Xe.

Figure 3.9: 75

Ps lifetime spectra in silica aerogel (Saito and Hyodo, 2006). Spectra labeled vacuum obtained without Xe are shown by a continuous line (B=0T) and dots (B=1T). Spectra obtained after Xe introduced are shown by crosses (B=0T) and triangles (B=1T).

Figure 3.10: 76

Total cross-section for Ps, e^+ and e^- scattering from Xe.

Figure 3.11: 77

Total cross-sections for e^+ colliding with H_2O.

Figure 3.12: 79

Dependence of the detection probability upon scattering angle at each incident e^+ energy investigated.

Figure 3.13: 80

Total cross-sections for Ps and e^+ colliding with H_2O molecules.

Figure 3.14: 81

Total cross-sections for Ps, e^+ and e^- colliding with H_2O molecules.

Figure 3.15: 82

Total cross-sections for Ps scattering from He, Ne, Ar and Xe.

Figure 3.16: 83

Total cross-sections for Ps scattering from H_2, N_2, O_2 and H_2O.

Figure 3.17: 85

Summary of total cross-sections for Ps scattering from He, Ne, Ar, Xe, H_2, N_2, O_2 and H_2O compared with available theories and momentum transfer cross-sections.

Figure 3.18: 86

Total cross-sections for Ps scattering from He, Ne, Ar, Xe, H_2, N_2, O_2 and H_2O compared with those of other projectiles: H atom, e^+ and e^-.

Chapter 4: Projectile Fragmentation and Target Ionization Cross-Sections by Positronium Impact

Figure 4.1: 90

Schematic of the scattering cell for Ps fragmentation studies (not to scale).

Figure 4.2: 91

Plot of the variation of an applied potential (-100V) with respect to the distance along the cell body.

Figure 4.3: 92

Schematic diagram of the e^- repeller.

Figure 4.4: 92

Schematic diagram of the residual field analyzer for residual e^- measurements

Figure 4.5: 94

Schematic diagram showing the potentials applied during measurements of the residual e^+.

Figure 4.6: 94

Schematic diagram showing the potentials applied during measurements of the residual e^-.

Figure 4.7: 95

Plots of the measurements under the various gas conditions for the production and scattering cells used to find the number of e^+/ e^- from Ps fragmentation and target ionization (where A and B represent the regions of interest for determining the integrated cross-section).

Figure 4.8: 96

Longitudinal energy distribution for the residual e^+ from Ps fragmenting on Xe atoms (arbitrary scale).

Figure 4.9: 96

Longitudinal energy distribution for the residual e^- from Ps fragmenting on Xe atoms (arbitrary scale).

Figure 4.10: 100

Geometry of the scattering cell (not to scale). The grey/purple region represents Ps outside the detection solid angle.

Figure 4.11: 103

Longitudinal energy distribution for the residual e^+ from Ps fragmenting on Xe atoms compared with theory.

Figure 4.12: 103

Longitudinal energy distribution for the residual e^- from Ps fragmenting on Xe atoms and possible target ionization compared with theory.

Figure 4.13: 104

Absolute integrated fragmentation and target ionization cross-section for Ps in collision with Xe atoms.

Chapter 5: Doubly Differential Ionization Cross-Sections for Positrons in Collision with H_2O Molecules

Figure 5.1: 108

Schematic of the experimental arrangement.

Figure 5.2: 110

Schematic of the source and moderator arrangement.

Figure 5.3: 114

Schematic diagram of the cross-section of the Parallel Plate Analyzer (not to scale).

Figure 5.4: 116

Beam energy profiles for 150.4, 97.4, 56.8, 37.8 and 27.8V moderator potentials.

Figure 5.5: 117

Calibration curve obtained using the energy profiles shown in figure 5.4.

Figure 5.6: 118

Schematic of the extraction and ion detection systems (not to scale).

Figure 5.7: 120

Probability of extracting H^+ with a given kinetic energy.

Figure 5.8: 120

H^+ kinetic energy distributions from two states of H_2O that undergo dissociative autoionization: a) H^++OH state and b) H^++O+H state (Cordaro *et al*, 1986).

Figure 5.9: 120

a) The convoluted H^+ kinetic energy distribution from the two states of H_2O of Cordaro *et al* (1986) and b) the extraction efficiency for H^+ within the electrostatic system.

Figure 5.10: 121

Schematic diagram of the electronics and data collection used for the DDCS.

Figure 5.11: 122

T-o-F spectrum of charged H_2O ions for a scattered e^+ energy of 37.4eV.

Figure 5.12: 125

DDCS at 0° for e^+ (100 and 153eV) – H_2O collisions of the following ions: H_2O^+, OH^+, H^+. ○ and ○ represent the H^+ DDCS corrected for the extraction efficiency. The arrows indicate the corresponding ionization limit (E_+-E_{th}).

Figure 5.13: 126

Comparison of the DDCS for e^+ scattered at ~ 0° following collision between 100eV e^+ and: • H_2O (this study) and • Ar (Kövér *et al*, 1993), respectively. The arrows indicate the corresponding ionization limit (E_+-E_{th}).

Figure 5.14: 126

The branching ratio for 100eV impact energy: a) H^+/H_2O^+ – • present data uncorrected and • present data corrected for the extraction efficiency, and b) OH^+/H_2O^+ • present data. The horizontal line represents the average value of branching ratio for e^- impact and the arrow indicates the ionization limit (E_+-E_{th}).

Figure 5.15: 127

The branching ratio for 153eV impact energy: a) H^+/H_2O^+ – • present data uncorrected and • present data corrected for the extraction efficiency, and b) OH^+/H_2O^+ – • present data. The horizontal line represents the average value of branching ratio for e^- impact and the arrow indicates the ionization limit ($E_+ - E_{th}$).

Appendix A: Determination of Detection Probability of Forward Scattered Positrons

Figure A.1: 131

The e^+ beam energy profile with V_s=20V. Inset is an expanded view of the region of interest.

Figure A.2: 132

Figure A.2: Diagram to clarify pitch angle and the longitudinal energy of the scattered e^+ detected at CEMA.

Figure A.3: 133

Dependence of the detection probability upon pitch angle at each incident e^+ energy investigated.

Appendix B: CPO Simulation of the Scattering Cell used for Positronium Fragmentation Studies

Figure B.1: 135

CPO-3D simulation of Ps fragmentation on the exit aperture of the cell (scaled by 1.75): e^- start from exit aperture and are shown by the coloured paths. Simulated for an applied potential of -100V on the cell and the apertures are held at ground.

Table Captions

Table Caption — Page number

Chapter 1: Introduction

Table 1.1: 20

Ground-state positronium properties: [a]Al-Ramadhan and Gidley, 1994; [b]Khriplovich and Yelkhovsky, 1990; [c]Asai *et al*, 1995; and [d]Adkins *et al*, 1992.

Table 1.2: 24

Time scales for positron and positronium in matter (see Schultz and Lynn, 1988).

Table 1.3: 28

Status of experimental interactions with positrons (Surko *et al*, 2005; Laricchia *et al*, 2003; and Charlton and Humberston, 2001).

Table 1.4: 32

Status of experimental interactions with positronium (Armitage *et al*, 2006; Leslie PhD thesis, 2005; and Laricchia *et al*, 2003).

Chapter 3: Positronium and Positron Total Cross-Sections

Table 3.1: 67

The scattering cell length and half-width-half-maxima for Ne, Xe and O_2.

Table 3.2: 72

The integrated cross-section of the metastable excited singlet states for e^- impact on molecular oxygen.

Table 3.3: 79

The half-width-half-maxima of the angular distributions of the detection probability displayed in figure 3.12.

Chapter 4: Projectile Fragmentation and Target Ionization Cross-Sections by Positronium Impact

Table 4.1: 89

The residual energies for the three main ionization processes available for Ps-Xe impact at 30eV.

Chapter 1: Introduction

1.1 Historical Background

The first experimental evidence of pair production and the existence of the positron (e^+), the antimatter counterpart of the electron (e^-), was provided by Anderson (1932a and b, 1933) whilst investigating cosmic radiation. Anderson's experimental apparatus consisted of a cloud chamber, which contained a thin lead plate and the entire apparatus was placed in a magnetic field. Whilst surveying the cosmic radiation he observed tracks, such as those shown in figure 1.1. From the study of these tracks, it was established that they were due to particles with an equal but opposite charge to the electron. A year later, Blackett and Occhialini (1933) confirmed that the charge-to-mass ratio of the particle (positron) was of the same order of magnitude as for the electron.

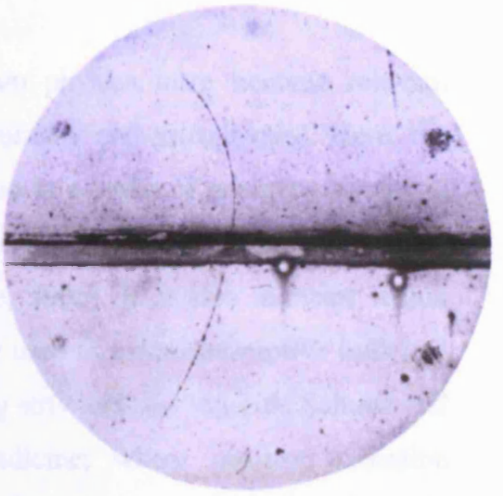

Figure 1.1: An early cloud chamber photograph, taken by Anderson (1932a), which revealed the existence of the positron.

The discovery of the positron by Anderson provided confirmation for Dirac's relativistic theory of quantum mechanics (1930a). Dirac's theory required both positive and negative solutions for the total relativistic energy for a free electron. This meant that electrons could fall from a positive energy level to a negative energy level, emitting a quantum of the appropriate energy. As this is not observed experimentally, Dirac proposed that a vacuum consists of an infinite sea of electrons occupying negative energy levels (from $-m_0c^2$ to $-\infty$) in accordance with the Pauli Exclusion Principle. This meant that electrons with positive energy would be stopped from falling into negative energy level states. Hence, if an electron occupying a negative energy level within the infinite sea is excited through the absorption of a quantum, it would jump to an unoccupied positive energy level. This would leave a hole in the negative energy level, which would then act as a positively charged electron with a positive energy (a positron).

In 1934, Mohorovicic predicted the existence of a quasi-stable bound state called positronium (Ps), arising from the Coulomb attraction between the positron and electron. The first quantum mechanical description of the structure of positronium was provided by Ruark (1945) and its binding energy and lifetime were calculated by Wheeler (1946). The first detection of positronium was made by Deutsch (1951) whilst studying positron lifetimes in gases.

Since the 1950's positron and positronium physics have become relevant across various branches of science, including astronomy and astrophysics. Here, the radiation from positron-electron annihilation is used as a probe of energetic events in our Galaxy providing unique details about the region from which it arises (Leventhal, 1992; Kinzer *et al*, 2001; Paul, 2004; and Milne, 2006). It is also relevant within condensed matter physics, where positrons may be used as a non-destructive bulk and surface probe for materials, especially for detecting structural defects (see Schultz and Lynn, 1988; and Coleman, 2002) and in medicine, where positron emission tomography (PET) has become a well-established medical technique for dynamic imaging and diagnosing cancer (Ott, 2003; and Czernin and Phelps, 2002). Within atomic physics, the advent of monoenergetic positron beams has enabled the attainment of collision data and hence comparative studies with electrons, protons and anti-protons, which have yielded information on the effects that mass and charge-sign have on collision dynamics (Knudsen and Reading, 1992). The production of positronium beams has allowed direct measurements of positronium cross-sections in collisions with atoms and molecules to be made (Garner *et al*, 1996; Armitage *et al*, 2006).

In the following sections of this chapter, fundamental properties of positrons and positronium are discussed, as well as recent studies of positron and positronium scattering from atoms and molecules.

1.2 Fundamental Properties of Positrons and Positronium

1.2.1 Positrons

The positron has the same mass and spin as the electron but its electrical charge, and hence magnetic moment, is of opposite sign. It is stable in vacuum with a

lifetime of more than $2x10^{22}$years (Bellotti *et al*, 1983). The positron may encounter an electron and annihilate with it resulting in the emission of gamma-rays, which due to energy conservation, must have a total energy equal to the rest mass energy (i.e. 1.022MeV) plus any kinetic energy of the positron/electron pair. The number of gamma-rays that are emitted is determined by the charge parity, P_C, of the annihilating system, which must be conserved. For a system containing n gamma-rays:

$$P_C = (-1)^n, \tag{1.1}$$

and for the electron-positron system:

$$P_C = (-1)^{L+S}, \tag{1.2}$$

where L is the total orbital angular momentum of the electron/positron system and S is its total spin (Yang, 1950). Therefore, an odd or even number of gamma-rays is released through annihilation depending on the total angular momentum of the positron/electron pair.

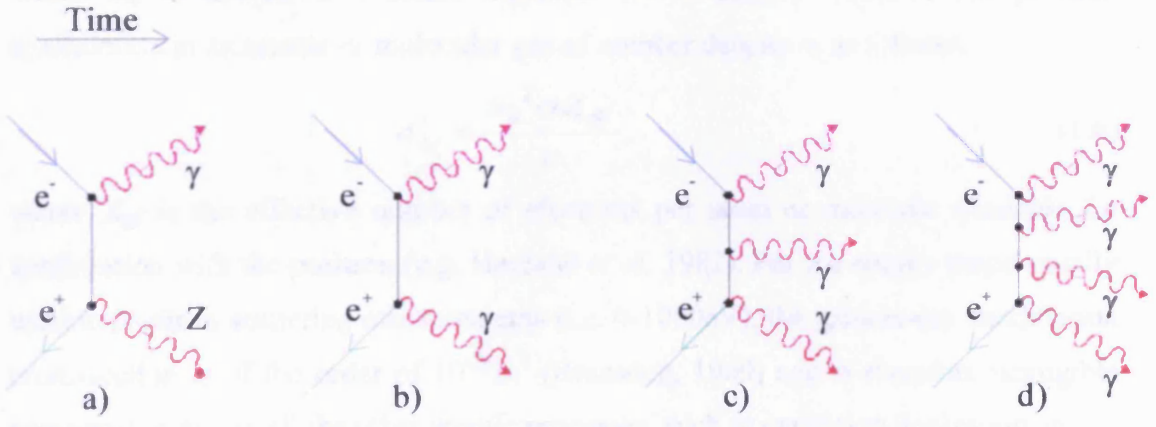

Figure 1.2: Feynmann diagrams of a) one, b) two, c) three and d) four gamma-ray decay modes.

Figure 1.2 shows the lowest order Feynmann diagrams for positron-electron annihilation resulting in one, two, three and four gamma-rays. The cross-section for a given decay mode is directly proportional to α^m, where m is the number of vertices in the corresponding Feynmann diagram and α is the fine structure constant, given by:

$$\alpha = \frac{e^2}{2\varepsilon_0 hc} \approx \frac{1}{137}. \tag{1.3}$$

where e is the electron charge, ε_0 is the permittivity of free space, h is Planck's constant and c is the speed of light. Hence, the most likely mode of annihilation is into

two gamma-rays shown in figure 1.2 b), as a) needs a nearby third body (Z) to conserve momentum and c) and d) have three and four vertices, respectively. The decay modes shown in figure 1.2 have all been observed by: a) Palathingal *et al* (1991), b) Klemperer *et al* (1934), c) Chang *et al* (1982 and 1985), and d) Adachi *et al* (1990).

The non-relativistic limit of the cross-section for positron-electron annihilation resulting in two gamma-rays derived by Dirac (1930b) is given as:

$$\sigma_{2\gamma} = \frac{\pi r_0^2 c}{v}, \tag{1.4}$$

where v is the velocity of the positron with respect to that of the electron and r_0 is the classical electron radius, given by:

$$r_0 = \frac{e^2}{4\pi\varepsilon_0 m_0 c^2}. \tag{1.5}$$

where m_0 is the electron mass. Equation 1.4 is usually modified for positron annihilation in an atomic or molecular gas of number density n, as follows:

$$\sigma_{2\gamma} = \frac{\pi r_0^2 c n Z_{eff}}{v}, \tag{1.6}$$

where Z_{eff} is the effective number of electrons per atom or molecule available for annihilation with the positron (e.g. Heyland *et al*, 1982). For the energy range usually used in positron scattering measurements (i.e. 0-1000eV), the gamma-ray annihilation cross-section is of the order of $10^{-26}m^2$ (Bransden, 1969) and is therefore negligible compared to nearly all the other atomic processes, such as excitation, ionization etc.

1.2.2 Positronium

Positronium is the bound state of a positron and an electron. It can be formed in two states: the singlet-state (para-Ps or p-Ps) and the triplet-state (ortho-Ps or o-Ps). Para-Ps is formed with an electron and a positron of opposite spins and in its ground state has a lifetime in vacuum of 125ps, decaying predominantly into two 511keV gamma-rays emitted back-to-back. Ortho-Ps is formed with an electron and a positron of parallel spins and has a lifetime in vacuum of 142ns in its ground state, decaying predominantly into three coplanar gamma-rays with energies from zero to 511keV.

Positronium annihilates into n gamma-rays according to equations 1.1 and 1.2, which yield:

$$(-1)^n = (-1)^{L+S}, \tag{1.7}$$

where S is the total spin and L is the angular momentum of the positronium. The characteristics for the two spin states are given in table 1.1, where due to spin statistics, positronium is formed in a ratio of ortho- to para-Ps of 3:1. Thereby, upon annihilation of ground-state positronium, three gamma-rays are more likely to occur.

Table 1.1: Ground-state positronium properties: [a]Al-Ramadhan and Gidley, 1994; [b]Khriplovich and Yelkhovsky, 1990 and Adkins *et al*, 2003; [c]Vallery *et al*, 2003; and [d]Adkins *et al*, 1992, Milstein and Khriplovich, 1994 and Adkins, 2005.

Name	State	Substate	Ground state decay rates (μs^{-1})	
			Experiment	Theory
p-Ps	1^1S_0	m=0	7990.9±1.7[a]	7989.5[b]
o-Ps	1^3S_1	m=0, ±1	7.0404(10)(8) (140ppm)[c]	7.0420[d]

Figure 1.3 shows the calculations of Adkins (1983) and the experimental data of Chang *et al* (1985) for the continuous energy distribution of the three coplanar gamma-rays arising from o-Ps. The theoretical and experimental data are found to be in good agreement.

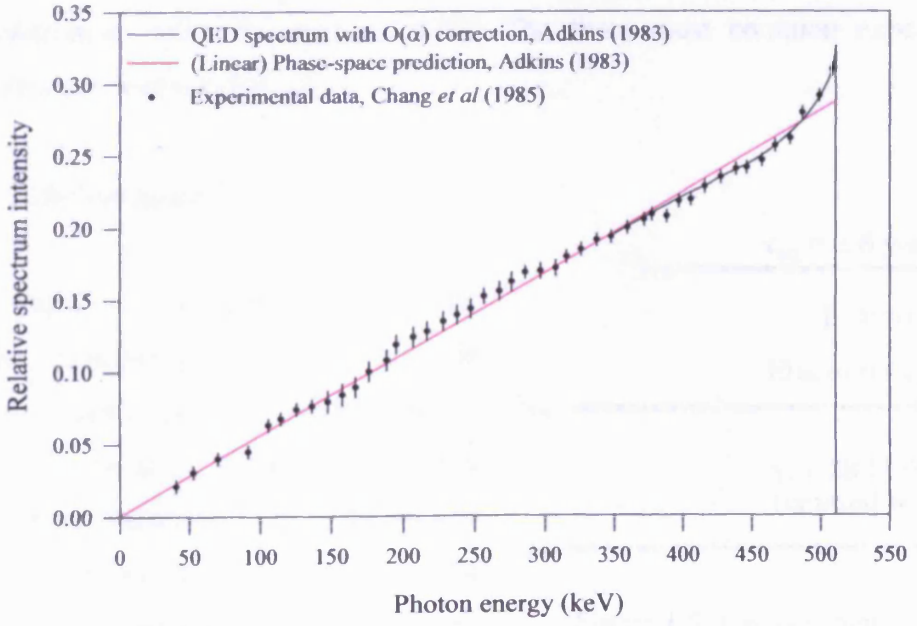

Figure 1.3: Energy distribution of gamma-rays emitted from o-Ps annihilation.

Positronium is structurally similar to hydrogen but, with half the reduced mass, it has half of the binding energy (6.8eV) and double the Bohr radius (1.05Å). The energy levels for both hydrogen and positronium (Fulton and Martin, 1954) are shown in figure 1.4 for comparison.

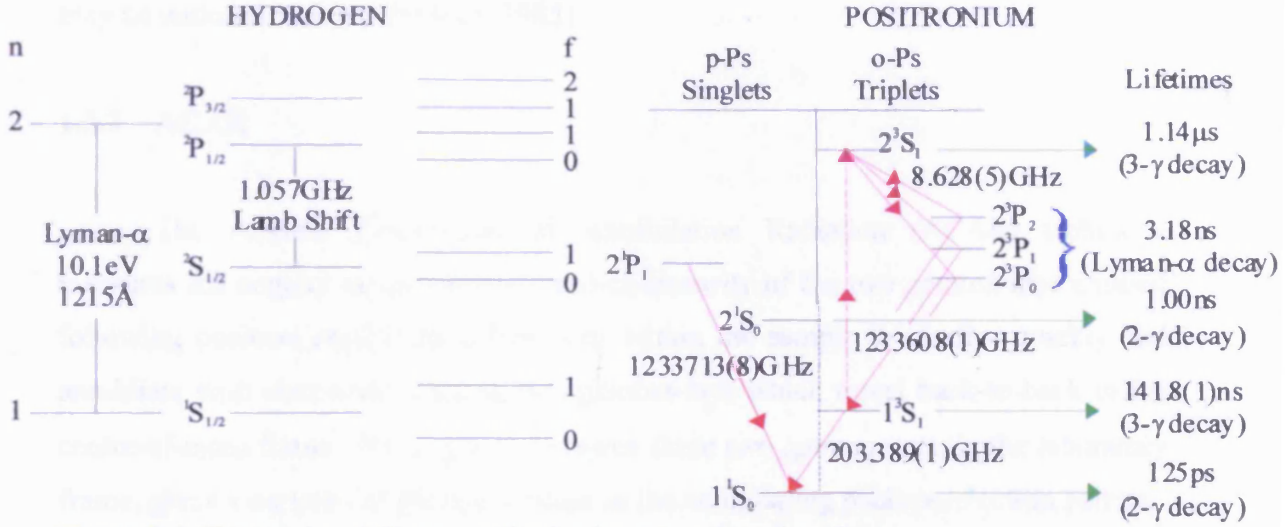

Figure 1.4: Energy level diagrams for hydrogen and positronium.

1.3 Early Techniques

The earliest experiments with positrons comprised a positron-emitting isotope within a solid, liquid or gas and the detection of gamma-rays from positron annihilation. These experiments provided information on the interactions of positrons and positronium with the medium itself. The three most common experimental techniques are discussed below.

1.3.1 Lifetime technique

Figure 1.5 shows the decay scheme for the radioisotope ^{22}Na, which is frequently used in positron lifetime studies as well as in medicine where it is used as a tracer to track natural sodium in the human body. As may be seen in the figure, the emission of a β^+ particle is followed by the

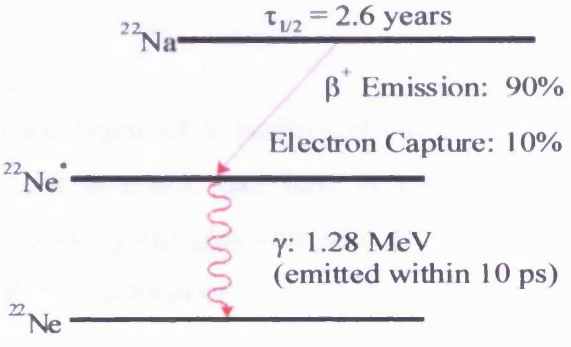

Figure 1.5: Decay scheme for ^{22}Na.

release of a 1.28MeV gamma-ray. Lifetime experiments utilize this gamma-ray in delayed coincidence with the annihilation gamma-ray from the positron in the sample investigated (Shearer and Deutsch, 1949). Through this technique, investigations into positronium formation and quenching, and positron and positronium thermalization may be undertaken (see Charlton, 1985).

1.3.2 ACAR

The Angular Correlation of Annihilation Radiation (ACAR) technique measures the angular deviation from anti-co-linearity of the two gamma-rays emitted following positron annihilation. Positrons within the sample thermalize quickly and annihilate with electrons, emitting two gamma-rays which travel back-to-back in the centre-of-mass frame. The angle, θ, between these two gamma-rays, in the laboratory frame, gives a measure of the momentum of the annihilating positron/electron pair as:

$$\theta \approx \frac{p_{\perp}}{mc}, \tag{1.8}$$

where $p_{\perp}$ is the perpendicular component of the centre-of-mass momentum, m is the positron mass and c is the speed of light. The technique is principally used in condensed matter physics to investigate the topography of Fermi surfaces (Dugdale *et al*, 1994), but it has also been employed in the study of positron and positronium annihilation in the noble gases (Coleman *et al*, 1994). As well as to determine the momentum transfer cross-section of positronium in collision with helium (Nagashima *et al*, 1998), neon and a range of molecular gases (Saito *et al*, 2003) at energies below the positronium fragmentation threshold.

1.3.3 Doppler Broadening

Gamma-rays released through the annihilation of a positron/electron pair, where the centre-of-mass of the annihilating pair is at rest, each have an energy of 511keV. However, a Doppler shift in the gamma-ray energies will arise due to the motion of the centre-of-mass. This energy shift, ΔE, is given by:

$$\Delta E = mc\, v_{cm} \cos\phi, \tag{1.9}$$

where m and c are defined in section 1.3.2, v_{cm} is the speed of the centre-of-mass of the positron/electron pair, and ϕ is the angle between the direction of motion of the centre-of-mass and that of one of the gamma-rays. This technique is often employed in the study of lattice defects, as freely diffusing positrons have a high affinity for trapping in a region of minimum potential, created by a missing ion core (Schultz and Lynn, 1988). It can also be used to give the momentum distribution of the annihilating pair and to measure thermalization rates (Skalsey *et al*, 1998), as well as to determine elastic scattering cross-sections for momentum transfer for positronium collisions with a variety of atomic and molecular gases.

1.4 Slow Positron Beam Development

Controlled experiments using the above techniques are impractical for energy dependent phenomena, due to the large intrinsic energy distribution of the fast positrons (β^+ particles) emitted through the nuclear decay of radioactive isotopes (e.g. ^{58}Co, ^{64}Cu, ^{68}Ge, ^{11}C and ^{22}Na: see Dupasquier and Zecca (1985) for their properties). An example of this is given in figure 1.6, which shows the energy distribution of positrons emitted from ^{22}Na. However, moderation allows a compression of phase space and therefore a greater gain of positrons with energies of a few eV over those

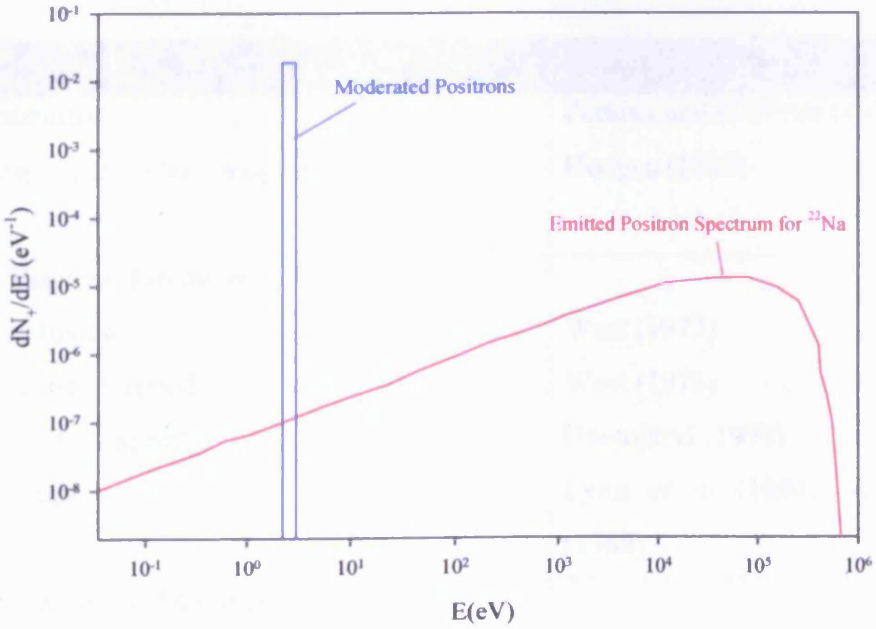

Figure 1.6: Energy distribution of positrons emitted from a ^{22}Na source and a tungsten moderator (centred at 3eV).

velocity-selected from the initial fast positron spectrum (also shown in figure 1.6). The process for obtaining moderated positrons with a few eV is described below.

1.4.1 Positrons in Solids

Fast positrons, implanted within a solid, lose energy mostly through collisions until they reach a state of thermal equilibrium. The typical timescales related to the possible interactions are outlined in table 1.2 and the interactions of positrons at a metal surface are shown in figure 1.7. In a defect free metallic solid, the implantation depth of the fast positrons emitted from a radioisotope is ~0.1-1.0mm, compared to the diffusion length of ~1000Å for a thermalized positron. Hence, the majority of positrons, which diffuse back to the metal surface, will be thermalized. Once thermalized, the de Broglie wavelength of the positron (~60Å at room temperature) is larger than the inter-atomic distance (typically a few Å) and therefore the positron acts like a propagating wave in the solid. Upon reaching the surface, a thermal positron may become localised and annihilate or it may be emitted into the vacuum as a free positron or positronium.

Table 1.2: Time scales for positron and positronium in matter (see Schultz and Lynn, 1988).

Process	Time (s)	References
Thermalization	$\sim 10^{-12}$	Perkins and Carbotte (1970)
Trapping (particular rate per atom)	$\sim 10^{-15}$	Hodges (1970)
Positron Lifetimes		
Freely diffusing	$\sim 1 \times 10^{-10}$	West (1973)
Monovacancy trapped	$\sim 2 \times 10^{-10}$	West (1973)
Multivacancy trapped	$\sim 4 \times 10^{-10}$	Hautojärvi (1979)
Surface State	$\sim 4\text{-}6 \times 10^{-10}$	Lynn *et al* (1984), Kögel *et al* (1988)
Positronium Lifetimes		
Triplet, in solids	$\leq 10^{-9}$	Dupasquier (1981)

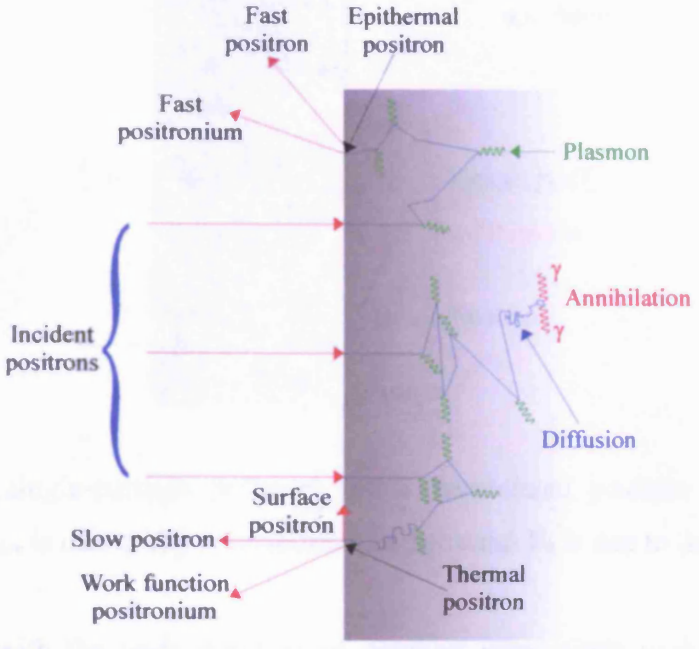

Figure 1.7: Simplified illustration of the interaction of positrons near the surface of a metal.

1.4.2 Positron Moderators

A one-dimensional illustration of the potential energy for a thermalized positron near a metal surface is shown in figure 1.8, for the case of a negative work function, ϕ_+.

The work function of a surface is the minimum potential energy needed to remove a positron from a point inside, to outside the metal. The work function for positrons can therefore be written as:

$$\phi_+ = -\Delta\varphi - \mu_+, \tag{1.10}$$

where $\Delta\varphi$ is the surface dipole and μ_+ is the bulk chemical potential of the positrons with respect to the mean electrostatic potential in the metal (Tong, 1972). The bulk chemical potential includes repulsion from the ion cores and attraction to the electrons.

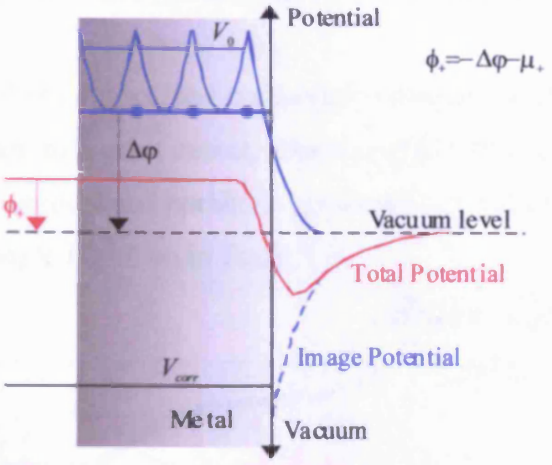

Figure 1.8: The single-particle potential for a thermalized positron near a metal surface, where V_{corr} is due to the conduction electrons and V_0 is due to the ion cores.

Progress with the understanding of positron interactions with solids comes from work performed on high purity, single crystal samples by Mills *et al* (1978). They found that a change in the temperature of the sample led to a change in the slow positron yield. Murray and Mills (1980) measured the moderation efficiency of aluminium and copper by controlling the temperature, surface coverage of S atoms, and orientation of the crystal lattice. Their results show that as the magnitude of the negative work function increases, so does the slow positron yield.

Dale *et al* (1980) annealed tungsten and molybdenum moderators and found that the moderation efficiency increased. This increase was firstly attributed to the reduction of the number of defects in the crystal lattice through heat treatment, as more trapped positrons were able to diffuse back to the surface. Also, for tungsten moderators, annealing allows for the extraction of the majority of adsorbed oxygen from the surface.

In 1986, Gullikson and Mills found that wide band gap insulators, such as rare gas solids (RGS), produce very effective positron moderators. This is due to phonon excitation being the only mechanism for positron energy loss once below the energy needed to make an electron-hole pair, an exciton or positronium atom. Phonon excitation removes only a few meV per collision and therefore the positrons have a long diffusion length (e.g. 5000Å for argon). This allows a considerable number of positrons emitted from the radioactive source to reach the surface of the moderator as

epithermal positrons with energies greater than the positron work function (i.e. ~1.7eV for argon).

The geometry of the source and moderator arrangement affects the efficiency of the slow positron beam to a great extent. Khatri *et al* (1990) and Greaves and Surko (1996) have shown that conical and parabolic geometries give the best RGS moderator efficiencies and an example is shown in figure 1.9.

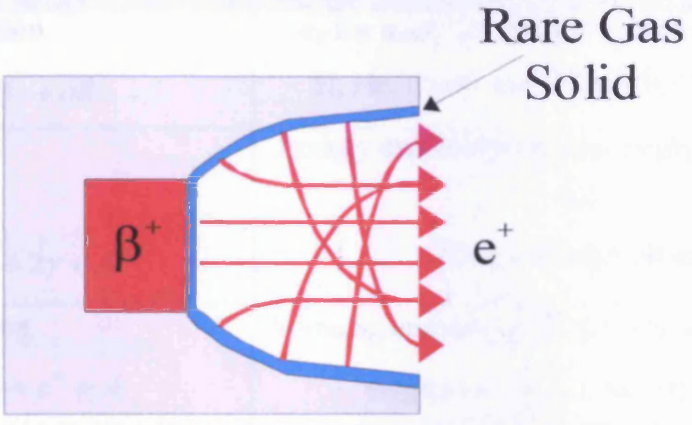

Figure 1.9: Conical geometry for a source and moderator arrangement.

RGS moderators are made by freezing the gas straight on to the surface of the radioactive source. The slow positron yield can also be increased by using sources of high specific activity, so that the number of fast positrons incident upon the moderator is increased.

1.5 Positron Interactions with Atoms and Molecules

Table 1.3 gives a summary of the current status of experimental studies of positron interactions with atoms and molecules. The most relevant topics for the present study are discussed in more detail below.

The total cross-section for positron scattering from atoms and molecules has been studied extensively (e.g. Kauppila and Stein, 1990). The first gases to be studied were noble gases (Kauppila *et al*, 1976, 1981; Stein *et al*, 1978; Dababneh *et al*, 1980; and Karwasz *et al*, 2002), as they exist in atomic form at room temperature. This work was then expanded to include simple and complex molecules (e.g. Hoffman *et al*, 1982; Sueoka and Mori, 1986; Kimura *et al*, 2000, 2001; and Sullivan *et al*, 2001,

2002), alkali metals (Kwan *et al*, 1989, 1991; and Stein *et al*, 1996) and atomic hydrogen (Stein *et al*, 1996; and Zhou *et al*, 1997).

Table 1.3: Status of experimental interactions with positrons (Surko *et al*, 2005; Laricchia *et al*, 2003; and Charlton and Humberston, 2001).

Interaction	Experimental Status
Total cross-section $e^+ + A \rightarrow all$	σ_T for many atomic and molecular targets i.e. H, He, alkali, Mg, O_2 and H_2O. This work.
Annihilation $e^+ + A \rightarrow 2\gamma + A^+$	Energy dependent measurements for Ar, Kr, Xe, N_2, CH_4, and other alkanes.
Elastic Scattering $e^+ + A \rightarrow e^+ + A$	Some σ_{el} and $d\sigma_{el}/d\Omega$ for atomic and molecular targets i.e. Ar, Kr, Xe, H_2 and CO.
Target Excitation $e^+ + A \rightarrow e^+ + A^*$	State resolved σ_{ex} for electronic and vibrational excitations. Including for Ar, CO, H_2, N_2, CO_2 and CF_4.
Positronium Formation $e^+ + A \rightarrow Ps + (m-1)e^- + A^{m+}$	σ_{Ps} for 1<E<100eV i.e. inert and molecular targets, also H, alkali and Mg; some $d\sigma_{Ps}/d\Omega$.
Direct Ionization $e^+ + A \rightarrow e^+ + me^- + A^{m+}$	σ_i^{z+} for 1<E<1000eV i.e. H, some $d\sigma_i^+/d\Omega$, $d^2\sigma_i^+/d\Omega_1\, dE_i$ and $d^3\sigma_i^+/d\Omega_1\, d\Omega_2 dE_i$. This work: $d^2\sigma_i^+/d\Omega_1\, dE_i$.
Formation of compounds $e^+ + A \rightarrow (PsC) + D^+$	Only PsH observed – failed search for PsCl and PsF.

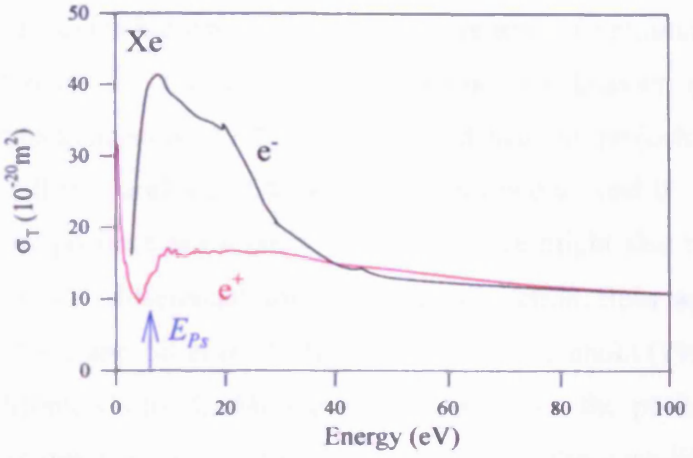

Figure 1.10: Schematic illustration of the behaviour of total scattering cross-sections for positron and electron impact with xenon.

The total cross-sections, σ_T, from positron and electron impact usually have noticeable differences, such as in the case of xenon (Xe) (see figure 1.10) where the electron total cross-section is a factor of 3.2 to 2.0 higher than that for the positron between 6 and 20eV, respectively. This is due to partial cancellation of the polarization and the static Coulomb interaction, and a smaller impact parameter for the positron. Whilst not shown on the figure, at the lowest energies (<1eV), there is a narrow minimum in the electron total cross-section, which arises from the quantum-mechanical nature of the elastic scattering of electrons by the target atom: this is referred to as a Ramsauer-Townsend minimum (Ramsauer, 1921, 1923; Townsend and Bailey, 1922; Ramsauer and Kollath, 1929). A similar feature is also seen in the electron scattering total cross-sections for argon and krypton and in those for positron scattering from helium, neon and possibly argon at energies between 1-3eV.

The total cross-section for positron scattering normally shows a distinct increase at the positronium formation threshold, E_{Ps}, (indicated by a blue arrow in figure 1.10), which reflects the considerable role this process plays in the scattering of positrons by inert atoms. As the impact energy increases, the static interaction process becomes more dominant, which should lead to the merging of the total cross-sections for the electron and positron: this happens at approximately 40eV for xenon.

The direct ionization process is also relevant for this work, as measurements of the doubly differential cross-section for positron-water impact have been performed to complete the work of Arcidiacono (PhD thesis, 2006), who monitored coincidences between the parent or fragment ions (i.e. H^+, OH^+ and H_2O^+) and the scattered positron. It had been predicted that the final state interaction between a scattered positron and an electron from target ionization may cause a cusp shaped peak in the

electron spectrum at a velocity which is equal to the final velocity of the positron. This process is known as Electron Capture to the Continuum (ECC) and has been studied at length for the impact of protons and heavier positive ions (e.g. Lucas and Steckelmacher, 1988). It was found that the projectile was scarcely deflected in the collision and the ECC peak was confined around 0°. It was therefore thought that, as the positron has a positive charge, there might also result a distinct ECC cusp in the doubly differential ionization cross-section from atomic hydrogen (Mandal *et al*, 1986; and Sil *et al*, 1991). Schultz and Reinhold (1990), using a Classical Trajectory Monte-Carlo (CTMC) method, found that the positron is deflected to much wider angles than the proton thus suppressing the cusp-like structure at any given angle. Using the Born approximation, Brauner and Briggs (1986, 1991), found that a cusp should be observed in the triply differential electron (or positron) spectrum. In this case, the ECC peak would be located at $(E_{\mp} - E_i)/2$ where $E_{\mp}$ is the kinetic energy of the incident electron (or positron) and E_i is the ionization energy of the target.

Kövér *et al* (1993) measured doubly differential ionization cross-sections for argon (Ar) at zero degrees using an electrostatic system to look for an ECC cusp. The energy distributions of the inelastically scattered positrons and electrons were measured in coincidence with the remnant argon ions for impact energies of 100eV, 150eV and 250eV. The doubly differential ionization cross-section for 100 and 150eV, which are relevant for this study, are shown in figure 1.11. The shapes of the energy spectra at the two impact energies are similar, but no significant structure is observed which can be ascribed to ECC in either case. The ECC peak would have been expected in figure 1.11a) at 42eV and in figure 1.11b) at 67eV. The only ECC calculations are for atomic hydrogen as a target and for Sil *et al* (1991), the ratio between the argon and atomic hydrogen cross-sections would have to be >10 to see any peak in the spectrum.

The measurements of Kövér and Laricchia (1998) however did indicate an ECC cusp, but only in the triply differential ionization cross-section (TDCS). These measurements were made for ejected electrons from 100eV positron impact on molecular hydrogen (H_2) and their results are shown in figure 1.12 along with the theory of Berakdar (1998). This theory assumed that molecular hydrogen consists of two non-interacting hydrogen atoms and that the relaxation time of the final H_2^+ ion is

a lot greater than the interaction time. Therefore, his results are twice those for atomic hydrogen but with the correct molecular hydrogen ionization energy.

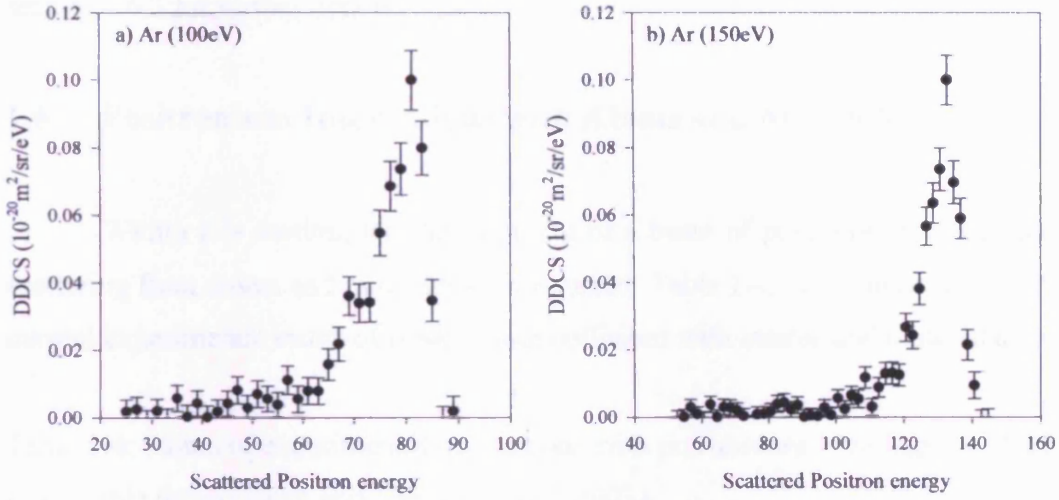

Figure 1.11: Doubly differential ionization cross-sections for positrons scattered at ~0° after collision between a) 100eV positrons and argon and b) 150eV positrons and argon.

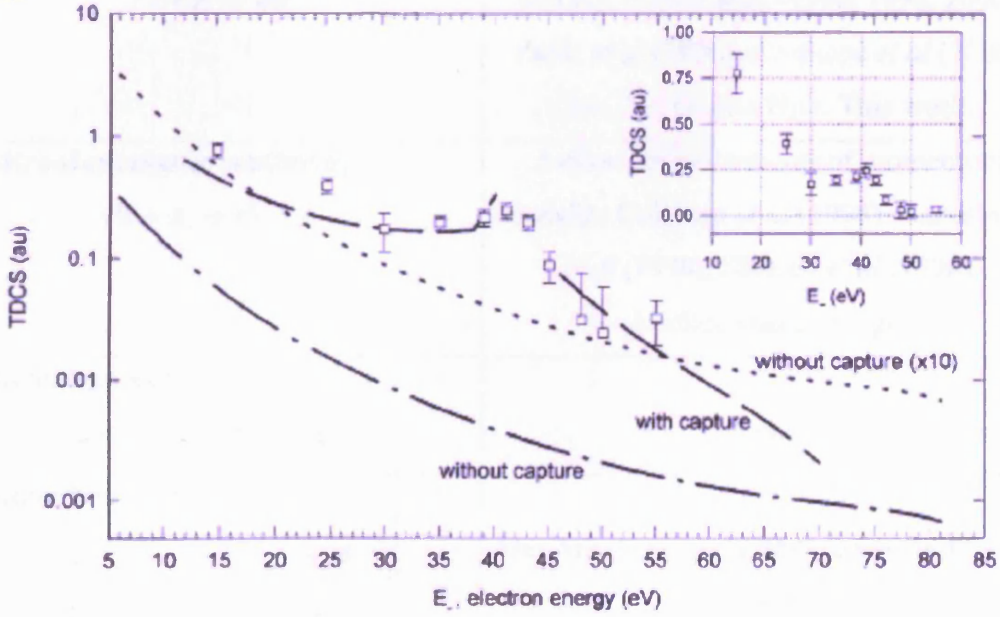

Figure 1.12: TDCS for electrons scattered at ~0° after collision between 100eV positrons and molecular hydrogen: hollow squares – Kövér *et al* (1998); curves – Berakdar (1998) folded with the experimental resolutions. The curve labeled "without capture" is also shown. The inset shows the experimental results in a linear plot.

As well as electron capture to the continuum, another process can occur in atom-atom collisions: electron loss to the continuum (ELC). Here, the residual

electron has a low relative velocity with respect to the scattered projectile and therefore can also give rise to a cusp-like shape in the differential cross-section (see section 1.6.3 for further details).

1.6 Positronium Interactions with Atoms and Molecules

Within this section, the development of a beam of positronium atoms and its scattering from atoms and molecules is discussed. Table 1.4, gives an overview of the current experimental status of positronium collisions with atomic and molecular gases.

Table 1.4: Status of experimental interactions with positronium (Armitage *et al*, 2006; Leslie PhD thesis, 2005; and Laricchia *et al*, 2003).

Interaction	Experimental Status
Total cross-section $Ps + A \rightarrow all$	Direct measurements for He, Ar, H_2, O_2 and N_2: Garner *et al* (1996, 1998, 2000), Zafar *et al* (1996), Armitage *et al* (2006). Ne, Xe, O_2 and H_2O: This work.
Positronium elastic scattering $Ps + A \rightarrow Ps + A$	Indirect measurements of momentum transfer: Coleman *et al* (1994), Nagashima *et al* (1998), Skalsey *et al* (1998). Limited energy range.
Positronium excitation $Ps + A \rightarrow Ps^* + A$	None.
Positronium ionization $Ps + A \rightarrow e^+ + e^- + A$ $Ps + A \rightarrow Ps + A^+ + e^-$ $Ps + A \rightarrow e^+ + e^- + A^+ + e^-$	He: Armitage *et al* (2002, 2006) and Leslie (2005). Xe: This work.

1.6.1 Development of Positronium Beams

Positronium is created by neutralizing a positron beam in a gaseous target, A, through the charge exchange reaction:

$$e^+ + A \rightarrow Ps + A^+. \qquad (1.11)$$

The kinetic energy for positronium, E_{Ps}, is given to a first approximation by:

$$E_{Ps} = E_{+} - I + B, \tag{1.12}$$

where E_{+} is the incident positron energy, I is the ionization potential of the gaseous target and B = 6.8eV is the binding energy of a positronium atom in the ground state.

The positronium beam production efficiency, ε_{Ps}, is the number of positronium atoms produced per incident positron per steradian and is given by:

$$\varepsilon_{Ps} = \frac{N_{Ps}}{\Omega N_{+}} D, \tag{1.13}$$

where N_{Ps} and N_{+} are the number of positronium atoms and incident positrons, respectively. D corrects for the in-flight decay of positronium atoms and Ω takes into account the detection solid angle.

The production efficiency of a positronium beam from argon, helium, molecular hydrogen, molecular nitrogen (N_2) and xenon for different gas pressures and positronium energies have been investigated by Garner *et al* (1996), Leslie *et al* (2002) and Laricchia *et al* (2004). Through these studies, it was shown that molecular hydrogen is the most efficient positron to positronium converter gas for positronium energies from 10 to 90eV and molecular nitrogen is the best for energies from 90eV to 250eV. Figure 1.13 shows the positronium production efficiency for molecular hydrogen and molecular nitrogen plotted against target gas pressure and positronium energy as a 3D plot.

As can be seen in figure 1.13, the production efficiency tends to saturate as the pressure of the target gas increases (Zafar *et al*, 1991; Laricchia and Zafar, 1992). This is due to competition between the formation of positronium and its subsequent scattering from the neutralizing gas, as described by the following expression:

$$\varepsilon_{Ps} \propto \{1 - \exp(-\rho l_{+} \sigma_{T+})\} \left\{ \frac{1}{\sigma_{T+}} \int_{0}^{\theta'} \frac{d\sigma_{Ps}}{d\Omega} \sin\theta d\theta \right\} \exp(-\rho l_{Ps} \sigma_{TPs}), \tag{1.14}$$

where $d\sigma_{Ps}/d\Omega$ is the differential positronium formation cross-section, and σ_{T+} and σ_{TPs} are the total cross-sections for positron and positronium scattering, respectively. The three terms correspond to the fraction of scattered positrons through a scattering cell of length l_{+}, the probability of making positronium within an angular range of 0 to θ', and the probability of positronium transmitted through a gas of density ρ and length l_{Ps}.

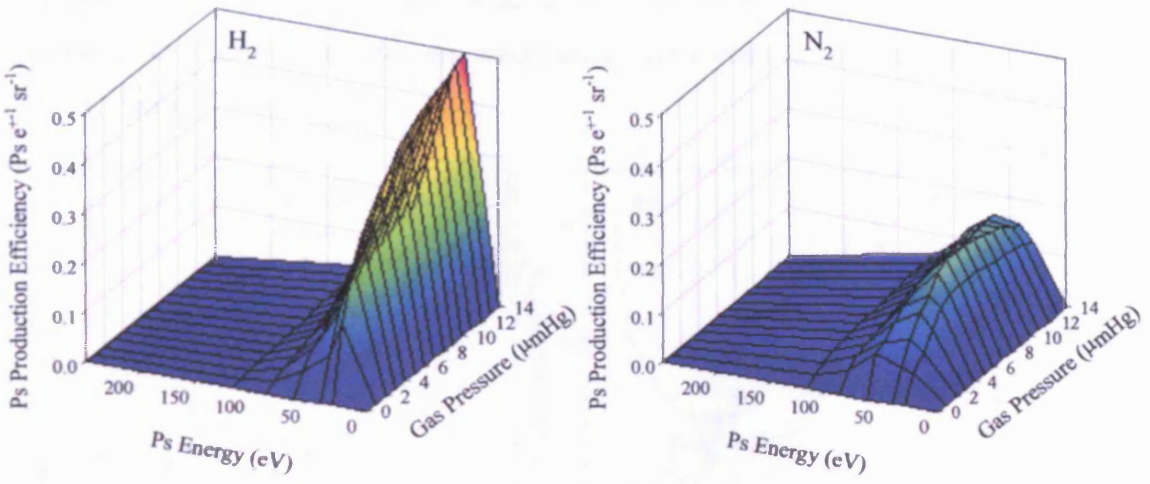

Figure 1.13: Positronium beam production efficiency measurements for H_2 – Garner *et al* (1996) and N_2 – Leslie *et al* (2002).

1.6.2 Positronium Scattering from Atoms and Molecules

Zafar *et al* (1996), Garner *et al* (1996, 1998, 2000) and Leslie (2005) determined the total cross-sections, σ_T^{Ps}, for positronium in collision with argon (Ar), helium (He), molecular hydrogen (H_2) and molecular nitrogen (N_2) by measuring the intensity of the positronium beam through the scattering cell (with and without gas) and using the Beer Lambert law:

$$\sigma_T^{Ps} = \frac{kT}{Pl} \ln\left(\frac{I_0}{I}\right), \tag{1.15}$$

where k is the Boltzmann constant, T is the ambient temperature, P is the pressure of the target gas, l is the effective length of the scattering cell, I is the transmitted beam intensity and I_0 is the incident beam intensity.

Figure 1.14 shows the results of the total cross-section for molecular nitrogen, argon, molecular hydrogen and helium (Leslie, 2005; and Garner *et al*, 1996, 2000) compared with available theories (McAlinden *et al*, 1996; Biswas and Adhikari, 1999, 2000; Blackwood *et al*, 1999, 2002; and Basu *et al*, 2001) and momentum transfer cross-sections (Coleman *et al*, 1994; Nagashima *et al*, 1998; Mitroy and Ivanov, 2002; Saito *et al*, 2003; and Skalsey *et al*, 2003). From this figure, it can be seen that all four targets show a similar trend, whereby there is a rapid increase in the total cross-section to a broad maximum, followed by a slow decrease at higher energies. An

extrapolation of the cross-section values to zero detection angle are also included in all cases except molecular nitrogen, where data were taken at a small acceptance angle of Ω~1.15msr.

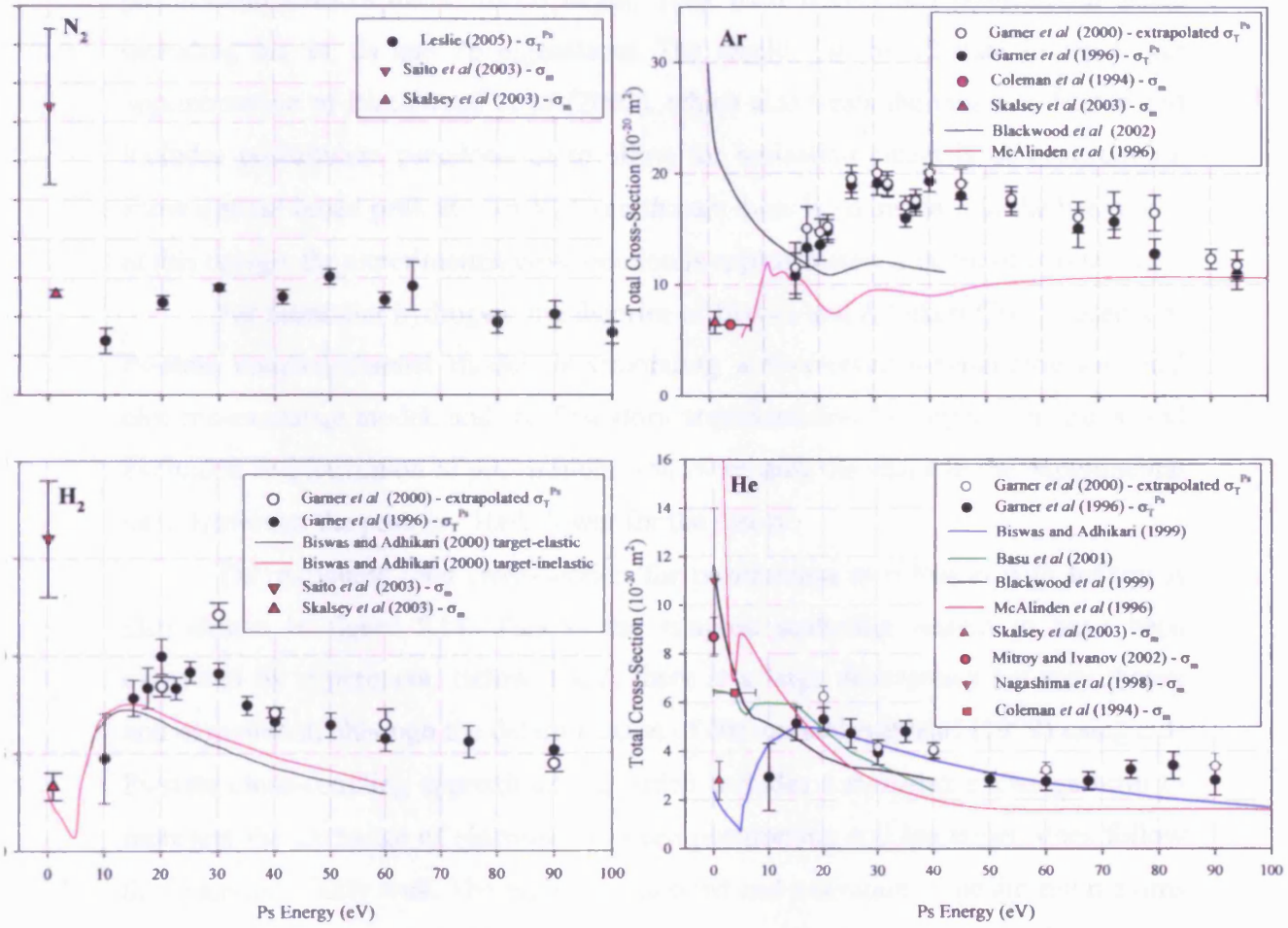

Figure 1.14: Available experimental and theoretical data for the total and momentum transfer cross-section of positronium in collision with N_2, Ar, H_2 and He.

Relevant theoretical and experimental data for the momentum transfer cross-section (σ_m) are also shown, although Blackwood *et al* (2002) noted that comparison between the total cross-section and the momentum transfer cross-section should be used with care due to the differential cross-section being anisotropic even at very low energies.

For argon, the theoretical data of McAlinden *et al* (1996) does not agree in shape or magnitude with the experimental data. At the lowest energies, this may be because it does not take into account the exchange interaction. At the highest energies however, the experimental and theoretical data converge. McAlinden *et al* (1996) determined the total cross-section by using the First Born approximation (which treats

the interactions as perturbations of free-particle systems) including the Hartley-Walters approximation for the target, for the inelastic processes. For the elastic processes, a coupled pseudostate calculation was used, which assumed that the positronium scatters off a frozen target. They used twenty-two positronium states including the 1s, 2s and 2p eigenstates. The results for the 22-state frozen target approximation of Blackwood *et al* (2002), which also treats the target as frozen and includes positronium pseudostates to allow for ionization channels of positronium, show a small broad peak at ~32eV. Even though there is an increase in the beam data at this energy, the experimental cross-section is approximately a factor of two higher.

For molecular hydrogen, the theories of Biswas and Adhikari (2000), used a 3-Ps-state coupled-channel model, incorporating a time-reversal-symmetric nonlocal electron-exchange model, and the first Born approximation for target excitations, and excitation and ionization of positronium, follow broadly the shape of the experimental data. However, the peak is ~10eV lower for the theory.

The measured total cross-section for positronium in collision with helium is also shown in figure 1.14. This is the simplest scattering system to have been examined by experiment. Below 10eV, there is a large discrepancy between theory and experiment, although the determination of Biswas and Adhikari (1999) using a 3-Ps-state close-coupling approximation, which includes a modified exchange term to represent the exchange of electrons between positronium and the target, does follow the beam data fairly well. The higher excitations and ionization of positronium atoms were treated by the Born approximation. The theoretical work of McAlinden *et al* (1996), and the close-coupling calculation of Basu *et al* (2001) using two basis sets (1s and 2p Ps-states) and Blackwood *et al* (2002) show a decrease from a maximum at low energies, whilst the theory of Biswas and Adhikari (1999) shows an increase to a broad maximum at ~15eV. The results of Blackwood *et al* (2002) lie up to 30% below the experimental data at energies between 20-40eV, indicating a possible underestimate of the elastic cross-section and/or target inelastic effects.

Finally, for molecular nitrogen, the experimental data are plotted along with the momentum transfer cross-section data of Saito *et al* (2003) and Skalsey *et al* (2003) measured using the ACAR technique and through time-resolved Doppler-broadening measurements of the annihilation photons, respectively. They are found to be a factor of five and two, respectively higher than the total cross-section at 10eV. There are currently no theoretical data available for comparison.

1.6.3 Fragmentation of Positronium in Collision with Helium Atoms

The main fragmentation/ionization channels for positronium colliding with a target at low energies are:

Channel I $$Ps + A \rightarrow e^- + e^+ + A, \quad (1.16)$$

Channel II $$Ps + A \rightarrow e^- + e^+ + A^*, \quad (1.17)$$

Channel III $$Ps + A \rightarrow Ps + A^+ + e^-, \quad (1.18)$$

Channel IV $$Ps + A \rightarrow Ps^* + A^+ + e^-, \quad (1.19)$$

Channel V $$Ps + A \rightarrow e^- + e^+ + A^+ + e^-, \quad (1.20)$$

where channel I corresponds to a target elastic collision (i.e. the target is left in its initial state); whilst in channel II the target is excited. Channel III corresponds to target ionization with the projectile remaining in its ground state; whilst in channel IV the positronium atom is excited and the target is ionized. Finally, channel V is a doubly inelastic channel which includes both projectile and target ionization.

The first measurement of projectile fragmentation was conducted by Armitage *et al* (2002) for positronium in collision with helium atoms at impact energies (E_{Ps}) of 13, 18, 25, 33 and 60eV. Both the integrated fragmentation cross-section and the longitudinal energy distributions of the residual positrons were determined. The residual positron energy distributions are shown in figure 1.17, where peaks are seen to develop just below half the residual energy, $\frac{E_r}{2} = \frac{(E_{Ps} - 6.8eV)}{2}$, becoming more prominent with increasing impact energy. The peaks indicate that the residual positron and electron stay strongly correlated in the final state, in a similar manner to the ELC in atom-atom collisions (discussed in section 1.5, and Ludlow and Walters (2001)). Armitage *et al* (2002) explained the shift in the peak from $E_r/2$ as arising from residual positrons being released within an angle of less than 20° with respect to the beam axis across the energy range.

Following the work of Armitage *et al* (2002), Sarkadi (2003) calculated the integrated fragmentation cross-section and the longitudinal energy distributions of both the residual positrons and electrons using a three-dimensional three-body version of the CTMC method, where the helium atom was considered as a structureless particle. His results were a factor of ~1.6 higher than the experimental integrated cross-section, but the shape of the longitudinal energy distributions of the residual

positrons was very close to those measured as shown in figures 1.16 and 1.17, respectively.

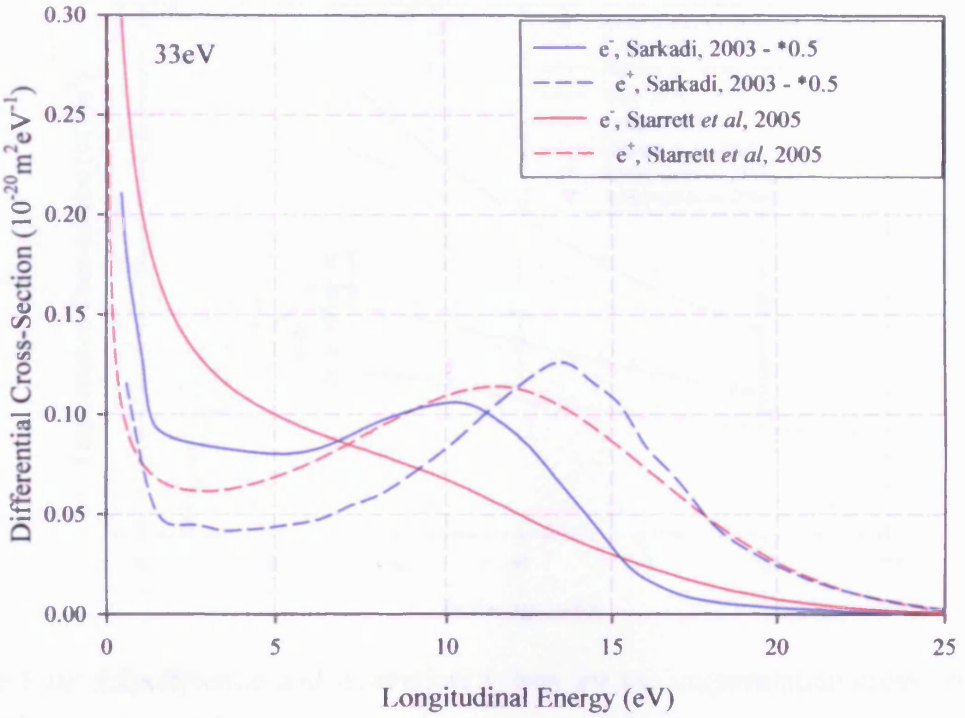

Figure 1.15: Theoretical data for the absolute differential cross-section for the residual positrons and electrons from positronium in collision with helium atoms at 33eV.

An asymmetry was also predicted by Sarkadi (2003), shown in figure 1.15, arising from the polarization of the positronium atom by the screened Coulomb potential of the target. This asymmetry was later confirmed by the Impulse Approximation of Starrett *et al* (2005), also shown in figure 1.15, which treats the scattering of positronium as a coherent sum of the individual scatterings of its constituents.

For the experiment of Armitage *et al* (2002), a time-of-flight (T-o-F) method was used, which allowed a stringent confirmation of the origin of the signal. To detect electrons at high and low energies, a different method of measurement was applied. This was done because low energy electrons are predicted to dominate the target ionization spectrum (channels III to V) but these, in a T-o-F spectrum, would be lost in the background. For higher energies, the energy resolution of the T-o-F gets gradually worse and hampers extraction of the electron energy spectra. A retarding field analyzer (RFA) was thus employed together with a biased scattering cell, in

order to accelerate the residual electrons away from the background of low energy secondary electrons.

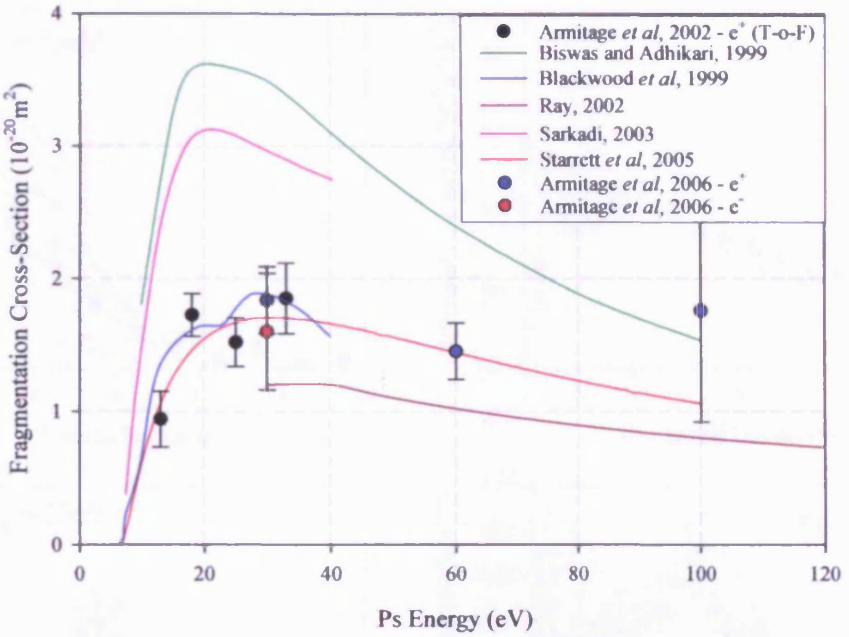

Figure 1.16: Experimental and theoretical values for the fragmentation cross-section of positronium in collision with helium atoms.

In order to check for the predicted asymmetry and probe for evidence of target ionization, the integrated fragmentation cross-section of positronium in collision with helium atoms and the longitudinal energy distributions of both the residual positrons and electrons were determined at 30eV (Armitage *et al*, 2006, 2007). The results indeed confirmed the predicted asymmetry (Armitage *et al*, 2007) and furthermore, target ionization was found to be insignificant, as the integrated fragmentation cross-section for the residual positrons and electrons were measured to be the same within errors (see figure 1.16).

As well as the theories of Sarkadi (2003) and Starrett *et al* (2005), which are shown in figure 1.16, there are various other theoretical determinations including Blackwood *et al* (1999), Biswas and Adhikari (1999) and Ray (2002). The theoretical calculation of Biswas and Adhikari (1999) using the Born approximation lies a factor of two above the experimental data. On the other hand, the Coulomb-Born approximation determination of Ray (2002), which used continuum Coulomb wavefunctions for the ionized electrons, produces results that lie below the experimental data. The theoretical data of Blackwood *et al* (1999) using a close-

coupled calculation and the results of Starrett *et al* (2005), broadly agree with the experimental data.

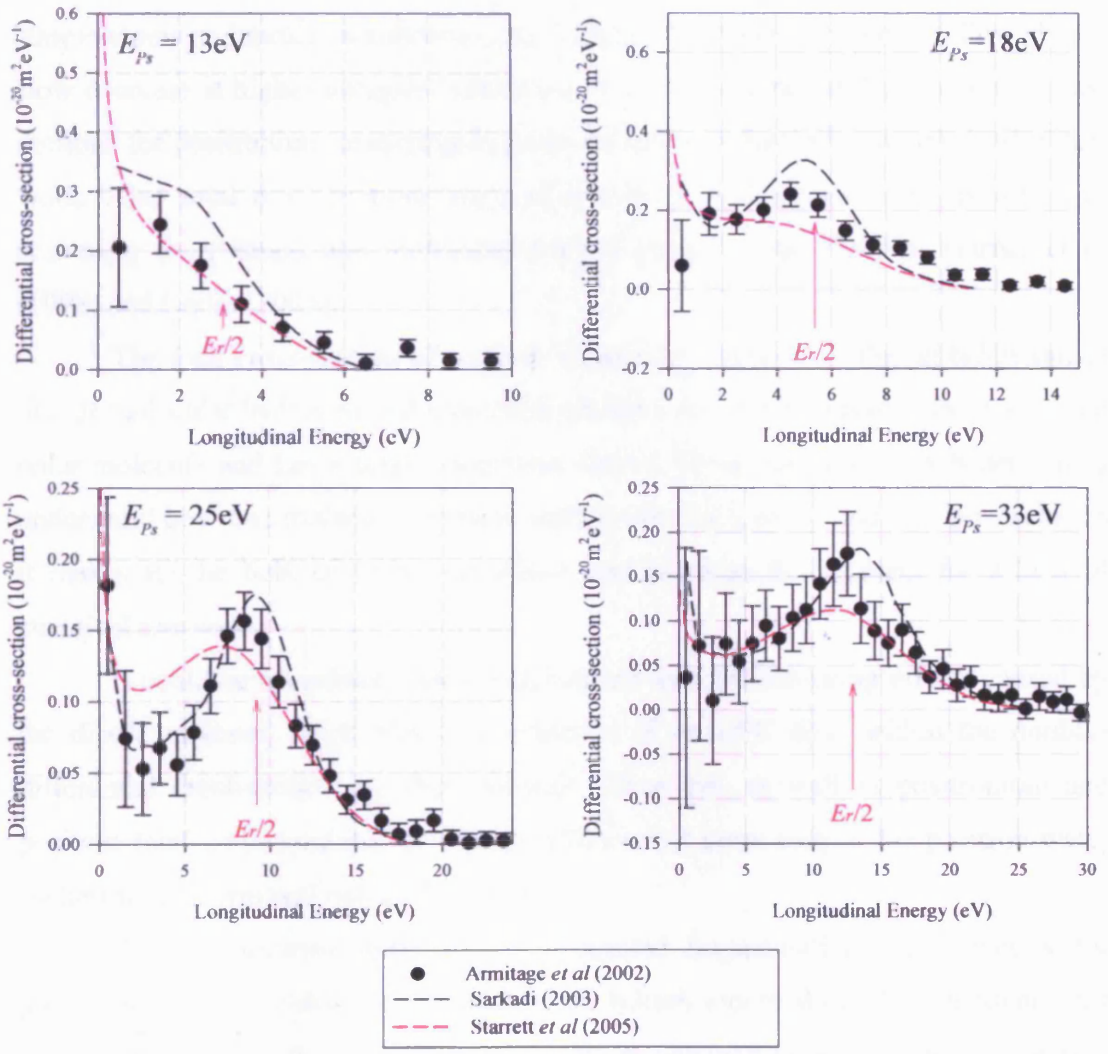

Figure 1.17: Experimental and theoretical data for the absolute differential cross-section for the residual positrons from positronium in collision with helium atoms.

Within figure 1.17, the Impulse Approximation of Starrett *et al* (2005) is ~50% lower than that of Sarkadi (2003) around the peak position for 13, 18, 25 and 33eV. An additional uncertainty of +8% to –(20-30)% was ascribed due to the systematic errors involved in the determination of the detection efficiencies using two different techniques (Armitage PhD thesis, 2002).

1.7 Motivation for Present Work

As discussed in section 1.6, the positronium total cross-sections for both simple atoms and molecules show a rapid increase to a broad maximum followed by a slow decrease at higher energies. Therefore, to help probe this further, the total cross-sections for positronium scattering from neon and water have been determined in this work. Also total cross-sections were measured to further investigate positronium scattering from xenon and molecular oxygen following the work of Garner *et al* (1998) and Leslie (2005).

The total cross-section of water is expected to display a different behaviour to that of molecular hydrogen and molecular nitrogen due to long range effects, as it is a polar molecule and has a large permanent electric dipole moment. It is beneficial to understand how this molecule interacts with positronium atoms and also positrons, as it makes up the bulk of living organisms and provides the medium for a host of chemical reactions.

It could be speculated that the significant forward-scattering effects caused by the dipole moment, might result in evidence of an ECC cusp within the doubly-differential cross-section for this molecule. Therefore, as well as positronium and positron total cross-sections, the doubly-differential cross-section for positron-water scattering is determined within this study.

Previous measurements of the integrated fragmentation cross-sections for positronium fragmentation in collision with helium atoms showed no evidence for target ionization, as the integrated cross-section obtained through electron detection was approximately equal to that deduced by positron detection. Therefore, measurements have been carried out with a xenon target at a higher excess energy above ionization with the expectation that target ionization might be observed.

Chapter 2: Positronium Beam Techniques

2.1 Introduction

Within this chapter the experimental apparatus for the production and detection of a slow beam of positrons (e^+) and its conversion to a positronium (Ps) beam are described. Figure 2.1 shows a schematic diagram of the experimental arrangement. The equipment was originally designed by Zafar *et al* (1991) and developed by Garner *et al* (1996), Özen *et al* (2000), Armitage *et al* (2002) and Leslie (PhD thesis, 2005), prior to the work shown in this thesis.

The apparatus can be divided into two separate parts: the source side and the experimental side. A monoenergetic beam of e^+ is obtained from a radioisotope of sodium (^{22}Na). The decay of the ^{22}Na results in the emission of β^+ particles, which are moderated by a solid argon (Ar) film deposited on a conical cup (Özen *et al*, 2000) and are accelerated to the required beam energy by applying a positive bias to the source with respect to the chamber ground. The slow e^+ beam is guided by an axial magnetic field produced by eleven Helmholtz coils and is separated from fast e^+ and gamma-rays emanating from the source region by a Wien filter. The two regions are separated by a pneumatic valve, which can be used to isolate the two sides when needed.

The experimental side is where the Ps beam is produced and scattered. Ps is generated in the 'production cell' and then enters the 'scattering cell', which contains the gas under investigation for scattering studies. For Ps studies, a set of grids in front of the scattering cell are used to reflect transmitted e^+ from the production cell away from the scattering cell. Another set of retarding grids, this time in front of the detectors, are used to prevent any e^+/e^- (electrons) from Ps fragmentation within the scattering cell from reaching the detector (Armitage *et al*, 2002).

The detection method utilized in this work incorporated a NaI gamma-ray detector in coincidence with a channel-electron-multiplier-array (CEMA).

The following sections give a detailed description of the experimental apparatus and detection methods.

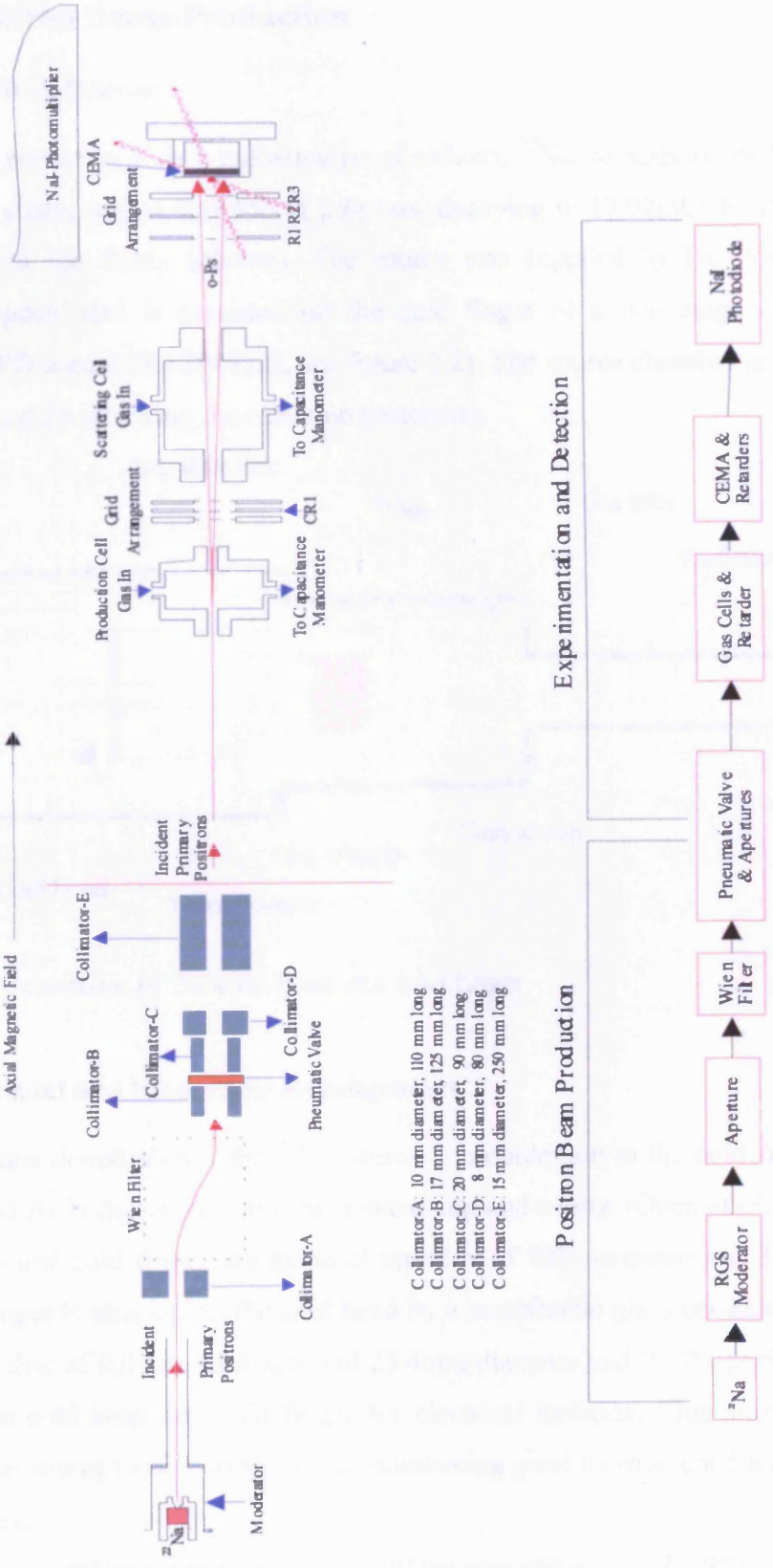

Figure 2.1: Schematic of the positronium beamline.

2.2 Positron Beam Production

2.2.1 Positron Source

The source of e^+ is a radioisotope of sodium, ^{22}Na, of activity 39.9mCi at the start of the study, with a half life of 2.6years, decaying to 17.92mCi by the end (see figure 1.5 for the decay scheme). The source was supplied by Du Pont plc in a titanium capsule and is mounted on the cold finger of a two stage closed-cycle cryostat (APD model DE-204SLB, see figure 2.2). The source chamber is surrounded by interlocked Pb shielding for radiation protection.

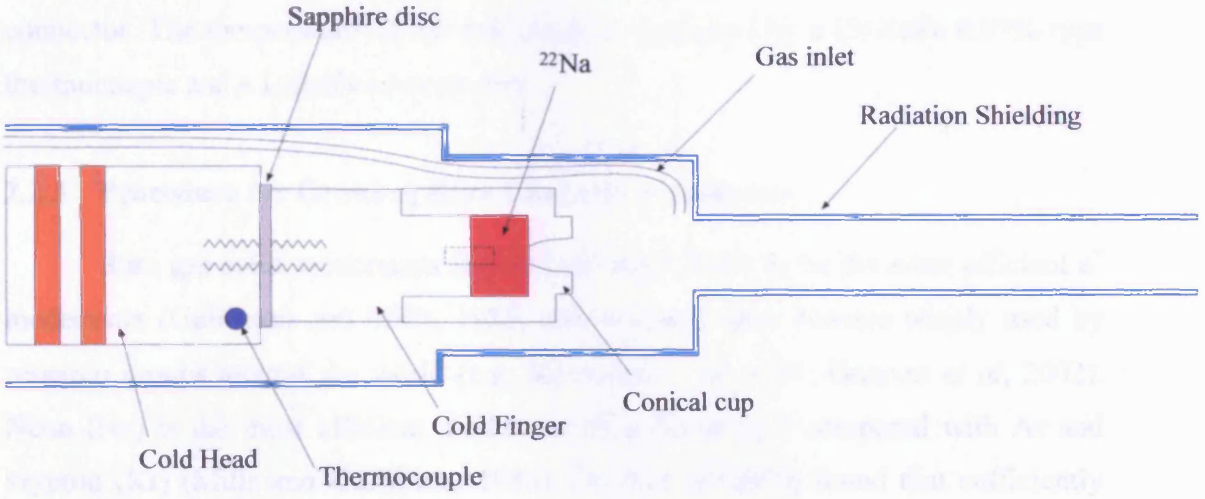

Figure 2.2: Schematic of the cold head and cold finger.

2.2.2 Cryostat and Moderator Arrangement

As mentioned above, the ^{22}Na source is mounted on to the cold finger, and a film of solid Ar is deposited onto the conical cup and source (Özen *et al*, 2000). The conical cup and cold finger are made of an alloy of 70% tungsten and 30% copper. The cold finger is attached to the cold head by a machinable glass-ceramic M6 screw. A sapphire disc of 0.5mm thickness and 25.4mm diameter and 99.9% purity is placed between the cold head and cold finger for electrical isolation. This allows the cold head and the source to be biased, whilst maintaining good thermal conductivity at low temperatures.

The conical cup provides a large surface area (Khatri *et al*, 1990; Greaves and Surko, 1996) and allows penetration of the electric field for slow positron extraction. Electrical contact with the cup is maintained through a tungsten wire of 0.075mm

diameter and 99.9% purity, which is connected to the cold finger by an Oxygen Free High Conductivity (OFHC) copper screw and to the cryostat by a feedthrough on the flange.

A radiation shield made of 1mm thick OFHC copper surrounds the cold head and the cold finger, extending by 90mm beyond the source. The shield is grounded via the cryostat, such that positrons can be extracted from the positively charged moderator.

Ar gas is admitted into the shield through a stainless steel pipe of 1.75mm diameter and an OFHC copper pipe of 1.3mm diameter, separated by a PTFE connector. The temperature of the cold head is monitored by a Cr-AuFe 0.07% type thermocouple and a Lakeshore controller.

2.2.3 Procedure for Growing Rare Gas Solid Moderators

Rare gas solid moderators (RGS) have been found to be the most efficient e^+ moderators (Gullikson and Mills, 1986) and therefore have become widely used by research groups around the world (e.g. Massoumi *et al*, 1991; Greaves *et al*, 2002). Neon (Ne) is the most efficient moderator by a factor of 5 compared with Ar and krypton (Kr) (Mills and Gullikson, 1986). Özen *et al* (2000) found that sufficiently low temperatures of the cold head (<6K), required to produce Ne moderators with reliably stable high efficiencies, could not be achieved with the present cryostat (with which a temperature of ~7K is attainable).

Ultra-high-vacuum conditions are required for optimum moderator efficiency and stability (Petkov *et al*, 1997). In order to achieve this, the system (i.e. the source and Wien filter chambers, gas line and source) is baked to an average temperature of 350K. The system is baked for five days (on average) until a base pressure of the order of $1x10^{-9}$Torr (0.1μPa) is achieved in the source chamber. Before the cryostat is turned on, the gas line is flushed to reduce impurities within the system further. Once the temperature of the cold head is ~7K, Ar is slowly admitted into the source chamber to a pressure of $2x10^{-6}$Torr (0.3mPa) where it freezes on to the cup and source. The source chamber pressure corresponds to a pressure of ~$2x10^{-8}$Torr (2.7μPa) in the ExB chamber (Wien filter region). The pressures are measured with ion gauges in the ExB and source chambers.

Figure 2.3 shows an example of a typical moderator growth plot for the system. The number of slow positrons is monitored with a CEMA, whose pulses are processed by a multi-channel-scalar, and the pressure in the source chamber is controlled by a bakeable leak valve.

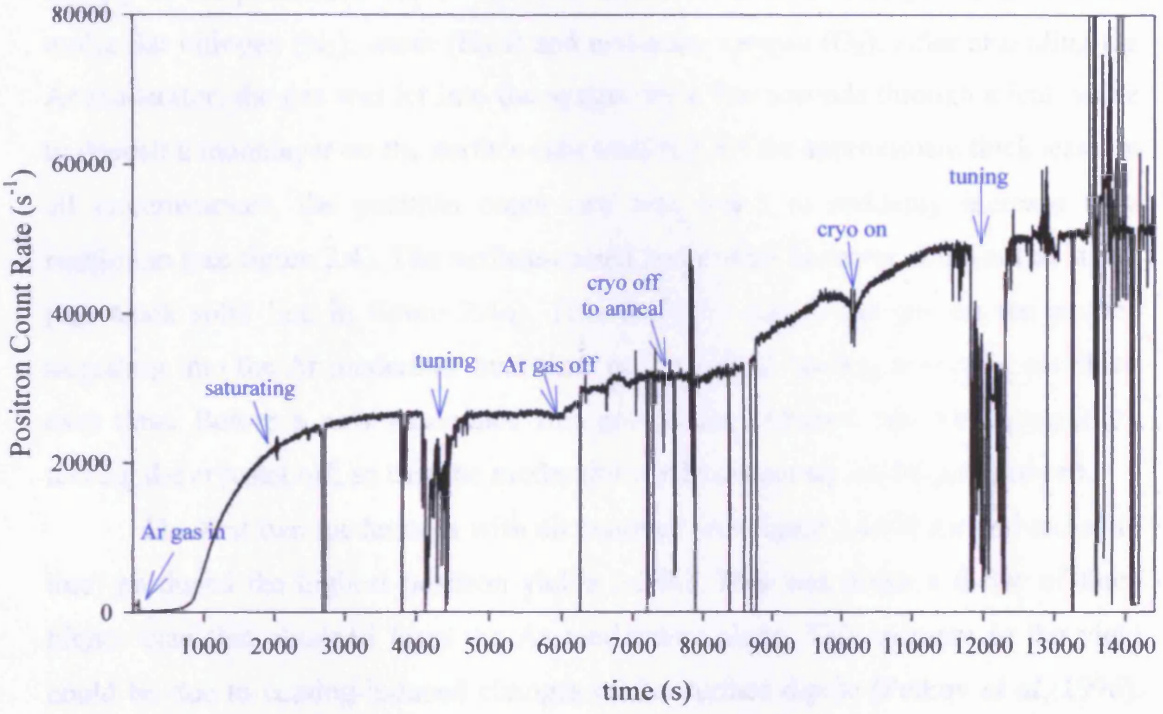

Figure 2.3: Example of an Ar solid moderator.

The number of slow e^+ increases with increasing moderator thickness, as seen in figure 2.3, until saturation, after which time the flow of gas into the chamber is stopped by closing the leak valve. During growing, the beam may be tuned by changing the currents and potentials of the magnetic field and Wien filter (see section 2.3), respectively, to achieve the maximum slow e^+ count rate. Once the leak valve is closed, a further increase is seen in the e^+ beam intensity, which is due to fewer e^+ being attenuated by residual gas in the chamber. When the slow e^+ count rate has saturated, the moderator is annealed by turning off the cryostat until the temperature of the cold head is 35K, after which time the cryostat is turned back on. This serves to decrease crystal defects by realigning the lattice (Klein and Venables, 1977), resulting in fewer e^+ being trapped and thus higher reemission, as can be seen in figure 2.3. During annealing, residual Ar frozen on the cold head is also removed to give a lower base pressure.

An investigation into growing a RGS moderator with a surface monolayer of another gas was carried out to see if a greater positron count rate could be achieved. This investigation was prompted by the observation that the slow positron count rate increases following a brief increase in pressure associated with the opening and closing of the pneumatic valve. This was tested for a number of gases, namely air, molecular nitrogen (N_2), water (H_2O) and molecular oxygen (O_2). After annealing the Ar moderator, the gas was let into the system for a few seconds through a leak valve to deposit a monolayer on the surface (see section 2.2.4 for approximate thickness). In all circumstances, the positron count rate was found to suddenly increase to a maximum (see figure 2.4). The surface-coated moderators however, were not as stable (see black solid line in figure 2.4a). This could be due to the gas on the surface migrating into the Ar moderator over time or the surface coating becoming too thick over time. Before a new moderator was grown, the previous one was dumped by turning the cryostat off, so that the moderator would evaporate and be pumped out.

The first two moderators with air coatings (see figure 2.4a black and red solid line) produced the highest positron yields (~34k). This was about a factor of three higher than that obtained from the Ar moderators alone. This increase in the yield could be due to coating-induced changes of the surface dipole (Petkov *et al*, 1996). For the N_2, O_2 and H_2O coatings the increases in positron yield were a factor of 1.5, 1.7 and 1.6, respectively. After the first two Ar moderators with a surface coating of air, the e^+ count rates for the other air coatings were found to be comparable to the Ar moderators with N_2, O_2 and H_2O. This suggests that after dumping previous moderators some of the impurities stayed in the source chamber, which could have frozen onto the new moderator making it less efficient. It would therefore be beneficial to repeat this study, but instead of dumping and then growing a new moderator straight away, the source chamber should be baked or flushed with Ar to dilute the impurity concentration.

The e^+ beam energy profiles shown in figure 2.5 for the surface coated moderators can be seen to have similar shapes and energy spread widths (~2eV) and are similar to the energy profile of a solid Ar moderator (see section 2.2.4).

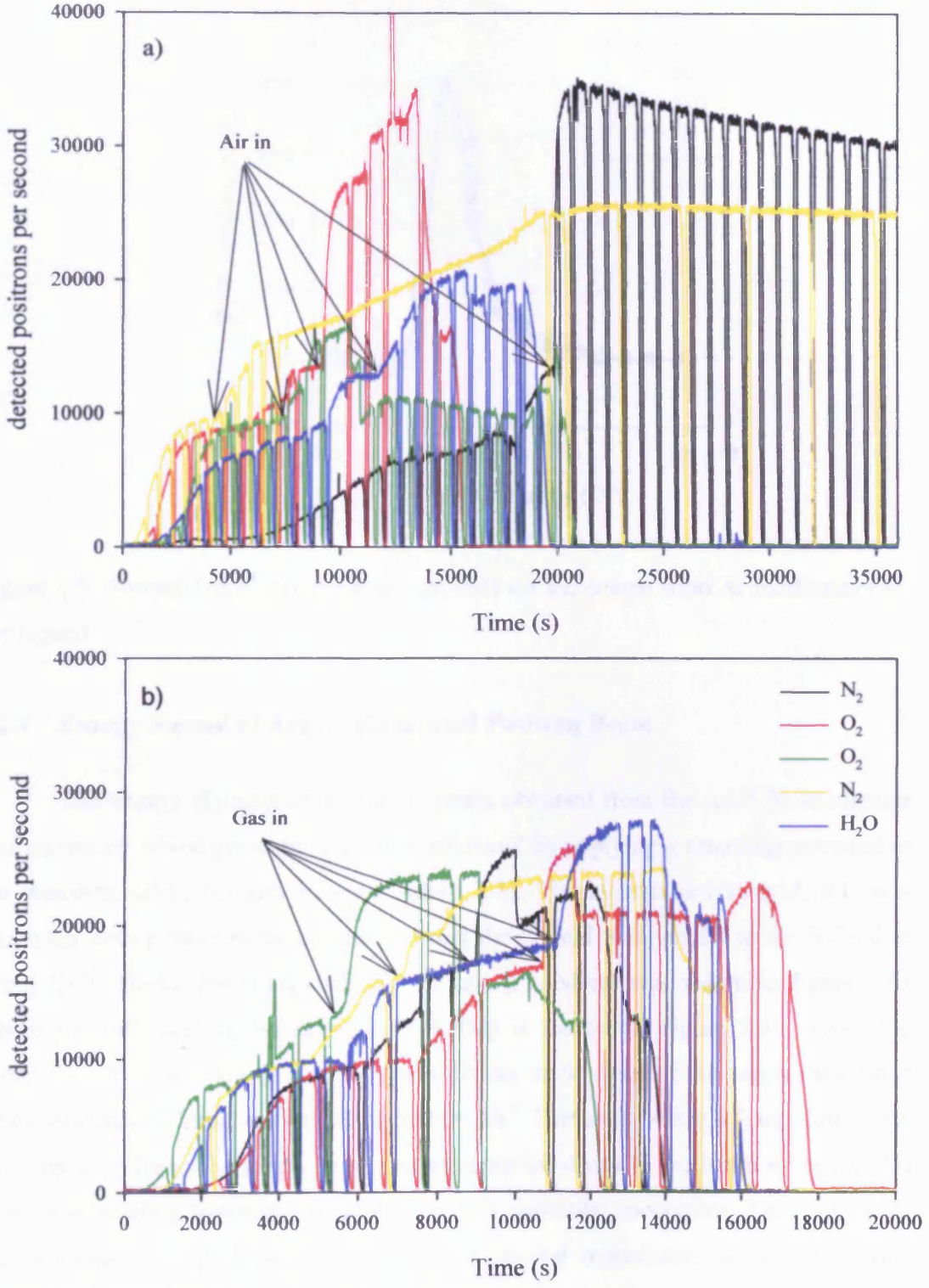

Figure 2.4: Examples of solid Ar moderators with a surface coating of: a) air and b) see legend for coatings.

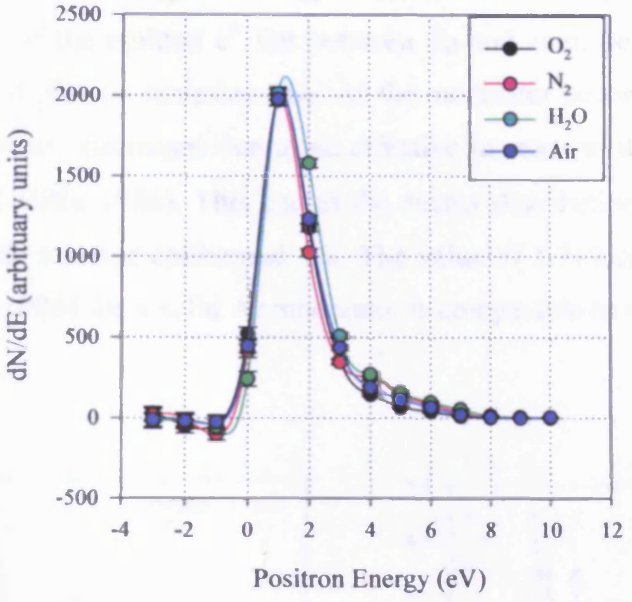

Figure 2.5: Normalized e^+-beam energy-profiles for the coated solid Ar moderators as per legend.

2.2.4 Energy Spread of Argon Moderated Positron Beam

The energy distribution of the e^+ beam obtained from the solid Ar moderator was measured whilst growing. This was achieved by applying a retarding potential to the retarding grids, R2 and R3 (see figure 2.1). The other retarding grid, R1, was grounded during these measurements so that the E-field was parallel to the B-field to avoid ExB effects. An energy profile for an Ar moderator is shown in figure 2.6a where the full-width-half-maximum (FWHM) is indicated. Figure 2.6b shows the energy widths (FWHM) obtained from differing thicknesses of the argon moderator given in terms of Langmuirs (1 Langmuir = 10^{-6} Torr sec), where a Langmuir is the gas exposure dose. The graph shows an exponential decay in the beam energy width over time, tending towards 1.8±0.2eV for this particular moderator. This highlights the importance of growing a moderator of several monolayers thick, where one monolayer is approximately one Langmuir if all the gas molecules stick to the surface, in order to have a slow positron beam with a narrow energy distribution.

Gullikson and Mills (1986) explained why the e^+ energy spreads from RGS moderators are ~2eV wide, in terms of the epithermal positron emission i.e. when the e^+ kinetic energy falls below the Ps formation threshold (E_{th} = 9.95±0.05eV for solid

argon (Gullikson and Mills, 1986)), the energy loss is dominated by phonon emission; therefore, the energy of the emitted e^+ lies between E_{th} and zero, depending on the implantation depth and phonon emission rate. As the moderator becomes thicker, the epithermal e^+ contribution decreases due to an effective increase in the implantation depth (Gullikson and Mills, 1986). This causes the energy distribution of the emitted e^+ to be narrower with a lower epithermal tail. The value of 1.7±0.2eV obtained by Gullikson and Mills (1986) for a solid Ar moderator is comparable to that observed in this work.

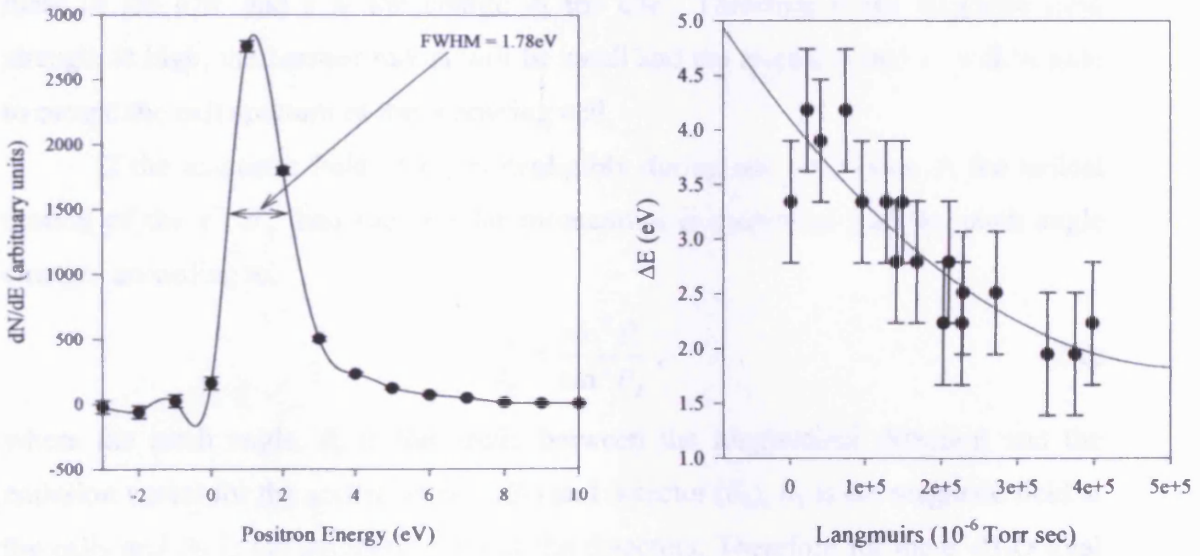

Figure 2.6: a) An example of a slow e^+ beam energy profile and b) an Ar moderator energy profile distribution.

2.3 Transporting the Positron Beam

2.3.1 Magnetic Field

The e^+ beam is guided by an axial magnetic field produced by eleven Helmholtz coils. Each coil has an outer diameter of 700mm and is water cooled. The coils can be moved along the beam line (the x-axis) and rotated about the y- and z-axes, in order to maximize the transport efficiency of the e^+ beam. The magnetic field strength is varied along the beam axis (4-22mT) in order to optimize the beam transport through the apertures, and to reduce spiralling of the e^+ in the scattering region.

For Ps fragmentation studies, a magnetic field strength of 22mT was applied to the scattering and detection regions to confine the ejected e^- and e^+ and to allow them to exit the scattering cell and be detected at CEMA (see section 4.3). This is because charged particles (e^-/e^+) which are emitted at an angle will follow a helical path along the axis of the magnetic field. The Larmor radius, r, of this helical path is inversely proportional to the magnetic field strength, B, applied, through:

$$r = v_{\perp} \frac{m}{eB}, \tag{2.1}$$

where $v_{\perp}$ is the perpendicular velocity with respect to the magnetic field, m is the mass of the e^-/e^+ and e is the charge of the e^-/e^+. Therefore if the magnetic field strength is high, the Larmor radius will be small and the ejected e^- and e^+ will be able to escape the exit aperture of the scattering cell.

If the magnetic field changes negligibly during one revolution of the helical motion of the e^+/ e^-, then the angular momentum is conserved and the pitch angle changes according to,

$$\frac{B_1}{B_2} = \frac{\sin^2 \theta_1}{\sin^2 \theta_2}, \tag{2.2}$$

where the pitch angle, θ, is the angle between the longitudinal direction and the emission vector for the scattering cell (θ_1) and detector (θ_2), B_1 is the magnetic field at the cells and B_2 is the magnetic field at the detectors. Therefore for the e^+-H_2O total cross-section study, a magnetic field gradient was applied between the scattering (B_1=4mT) and detection (B_2=22mT) regions to partially discriminate against forward-scattering (see section 3.4.4).

2.3.2 Wien Filter

The slow e^+ beam is separated from the stream of fast particles and gamma-rays emanating from the source by deflection through a Wien filter (see figure 2.7).

The Wien filter, which acts as a velocity selector, consists of a pair of curved plates to which approximately equal and opposite voltages are applied. Following the work of Hutchins *et al* (1986), the curved plates are flared at the ends to minimize fringing effects and preserve the beam shape after deflection. The electrostatic field, $\underline{E}$, is applied perpendicular to the axial magnetic field, $\underline{B}$, produced by the Helmholtz

coils. This causes charged particles with a velocity, v_x, to drift by a distance, y, given by:

$$y = \frac{\underline{E} \times \underline{B}}{\underline{B}^2}\left(\frac{L}{v_x}\right), \tag{2.3}$$

where L is the length of the plates and v_x is the particle velocity parallel to $\underline{B}$. In this way, the slow positron beam is lowered by 3cm, and the fast particles and gamma-rays are blocked by a Pb plug.

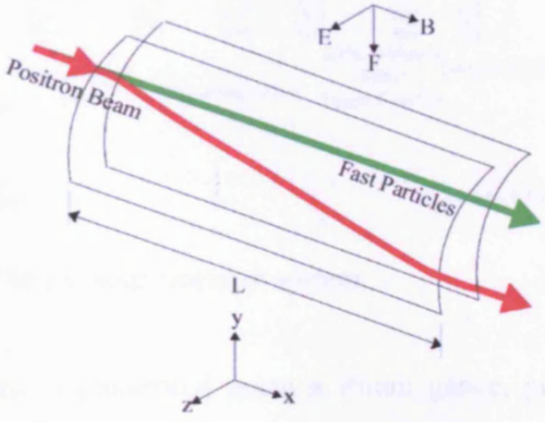

Figure 2.7: Schematic of the Wien Filter.

2.4 Vacuum System

Figure 2.8 shows a schematic diagram of the vacuum system. The two sections of the apparatus are pumped by different methods and are described separately.

2.4.1 Source Region

In the source and ExB chambers, an ultra-high-vacuum ($\leq 10^{-9}$Torr (0.1μPa)) is needed to grow an efficient, stable RGS moderator. This ultra-high-vacuum is achieved through two turbo pumps: an Edwards turbo molecular pump (EXT 70H) connected to the source chamber and a Varian turbo pump (V550) connected to the ExB chamber. The pumps are H_2O cooled and both are backed by a Varian dry scroll pump (TriScroll™ 300). The dry scroll pump is used instead of a standard rotary pump to keep the source side oil free and hence limit contaminants which adversely affect the moderator efficiency.

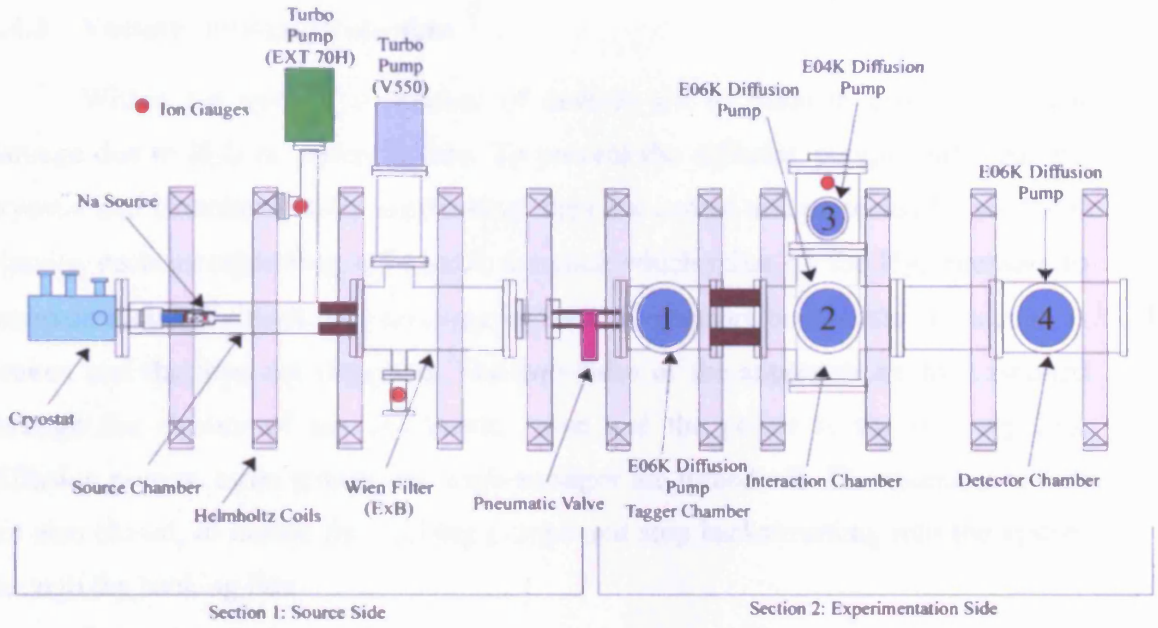

Figure 2.8: Schematic of the Ps beam vacuum system.

The backing line pressure is monitored using a Pirani gauge, placed between the backing and turbo pumps. In the case of vacuum or power failure, the backing pump may be isolated using either a magnetic or manual valve. Two ion gauges, one situated in each chamber on the source side, are used to monitor the system pressure. A pneumatic valve is situated between the source and experimental regions in order to isolate the two sides of the system in case of a power or H_2O cooling failure, or pressure increase in one of the regions.

2.4.2 Experimental Region

In the experimental region, a high-vacuum ($\leq 10^{-6}$Torr (0.1mPa)) is used. This is achieved through four H_2O cooled oil-based diffusion pumps (one Edwards E04K and three E06K), which contain Santovac-5 oil. Two of the pumps (pumps 2 and 3, see figure 2.8) are backed by an Edwards rotary pump (E2M40), and the others (pumps 1 and 4, see figure 2.8) are backed by Varian rotary pumps (SD300 and DS202, respectively). A Pirani gauge between each diffusion pump and its corresponding backing pump is used to monitor the backing line pressure, and magnetic and manual isolation taps are placed between the pumps, such that the backing pumps maybe isolated if required. To monitor the system pressure, an ion gauge is situated above diffusion pump 3.

2.4.3 Vacuum System Protection

Within the system, a number of devices are in place in order to prevent damage due to H_2O or power failure. To prevent the diffusion pumps, turbo pumps, cryostat and Helmholtz coils overheating, they are cooled and protected by six H_2O-circuits, each incorporating a flowtrol: a switch which relies on the H_2O pressure to maintain a closed circuit. If a decrease in the H_2O pressure occurs, the connection is broken and the trips are triggered. The two sides of the apparatus are then isolated through the closure of the pneumatic valve and the power to the coil supplies, diffusion pumps, turbo pumps and high-voltages are turned off. The magnetic valves are also closed, to isolate the backing pumps and stop backstreaming into the system through the backing line.

Protection devices, which rely on the pressure readings in the backing lines, are present in the case of a pump failure, a leak in the vacuum chamber or an uncontrolled inflow of gas. The backing pressure trip level for these circuits is set to $7x10^{-2}$Torr (9.3Pa) at which point the protection devices are triggered, shutting the system down as described above. The cryostat has additional devices, which prevents it from being powered if the H_2O pressure for the cryostat or the vacuum in the system is insufficient.

2.5 Positronium Beam Production

2.5.1 Introduction

Ps is created within the production cell via the charge-exchange reaction,

$$e^+ + A \rightarrow Ps + A^+, \tag{2.4}$$

whereby the incident e^+ captures an e^- from the production gas (A) (Charlton and Laricchia, 1990). For the range of energies used in this work, molecular hydrogen (H_2) was used as the Ps formation gas within the production cell for energies less than 100eV (Garner *et al*, 1996; 1998), and N_2 was used for energies greater than 100eV (Leslie *et al*, 2002). These gases were chosen for their efficient Ps production at these energies (see figure 1.13).

Providing there are no inelastic effects simultaneous to Ps formation, the kinetic energy of the Ps beam, E_{Ps}, is given to a first approximation by (Laricchia *et al*, 1992):

$$E_{Ps} = E_{+} - I + B, \tag{2.5}$$

where E_{+} is the e^{+} beam kinetic energy, I is the ionization energy of the production gas and B is the binding energy of Ps (6.8eV for the ground state).

The efficiency of producing the Ps beam is dependent on the differential Ps formation cross-section of the gas used to neutralise the e^{+} and the total cross-sections for both e^{+} and Ps scattering (Garner *et al*, 1996).

2.6 Experimental Region

2.6.1 Gas Cells

As shown in figures 2.1 and 2.9, two gas cells are used in this study. Ps is produced via charge-exchange with the gas in the first cell (the production cell) (see Section 2.5.1) i.e. H_2 (for incident positron energies <100eV) or N_2 (for incident positron energies >100eV). The pressure within the production cell is typically 1.33Pa throughout the Ps measurements, so that the Ps production efficiency does not vary with pressure fluctuations (see figure 1.13 and Garner *et al*, 1996). The scattering of Ps with a target gas occurs within the second gas cell (the scattering cell). The scattering cell for this study had brass or aluminium (Al) apertures depending on what was being measured, whereas the production cell had lead apertures throughout the work to reduce the background of gamma-rays and fast particles emanating from the source.

The gas cell pressures are measured with external capacitance manometers (Chell MK7893) with a range of up to 1Torr (133Pa). Gas inlets on the gas cells are attached to external gas cylinders via computer controlled valves to accurately control the gas flow into the cells.

Three different scattering cells have been used for this study: a simple cylinder for the total-cross section measurements; a narrow long cylinder for H_2O scattering measurements; and a specially designed cell for Ps fragmentation measurements (see sections 2.6.1, 3.3.2 and 4.2, respectively).

A retarding grid arrangement is placed between the two cells in order to prevent e^+ transmitted through the production cell from entering the scattering cell and forming Ps. This arrangement consists of three copper grids (90% transmission), the outer two grids are earthed to shield the interaction regions from stray electric fields, and the middle grid is positively biased.

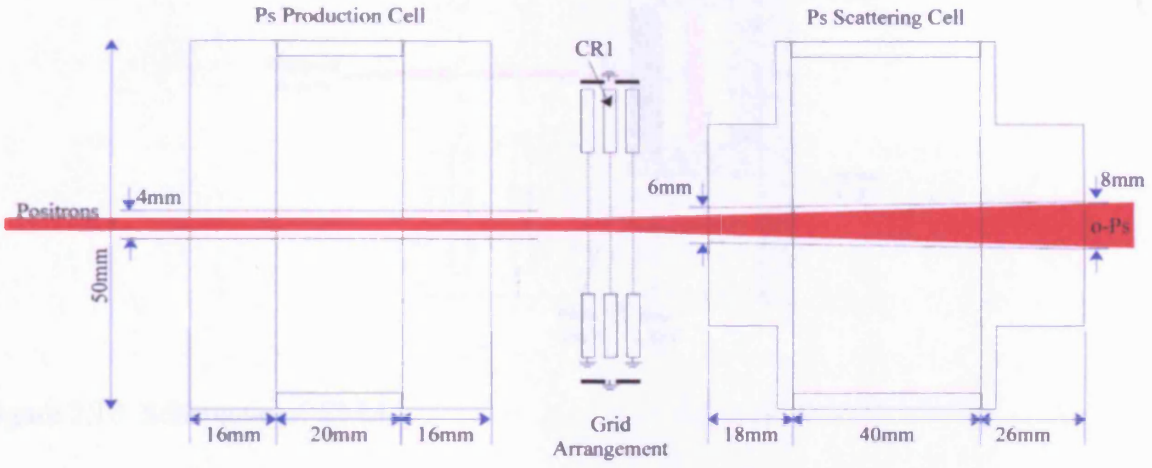

Figure 2.9: Schematic of the gas cells: scattering cell shown is for total cross-section measurements.

2.6.2 CEMA (end-of-flight detector)

A channel-electron-multiplier-array (CEMA), shown schematically in figure 2.10, is placed at the end of the flight path, after the gas cells, to detect either e^+ or Ps atoms, as discussed below. The signal from CEMA can be used in coincidence with a gamma-ray detector (described in section 2.6.3). A further grid arrangement, again comprising three copper grids (90% transmission), is positioned in front of CEMA. The first grid, R1, is earthed when detecting the incident e^+ beam and e^+/e^- from Ps fragmentation, and is positively biased when detecting Ps, to repel any e^+ emitted from the scattering cell. The grids R2 and R3 are used to increase the detection efficiency of CEMA (Armitage PhD thesis, 2002) by returning secondary e^- liberated from the surface of the channel plates. During Ps fragmentation measurements R2 and R3 are used to energy analyze the ejected e^+ and e^-. The grid potentials are shown in figure 2.10 for the incident e^+ beam. The assembly is enclosed in an earthed wire cage in order to minimize stray electric fields, and it is mounted on a linear manipulator so

that the Ps flight-length may be varied to obtain the maximum count rate. Pulses from CEMA are sent to external electronics, as discussed in section 2.7.

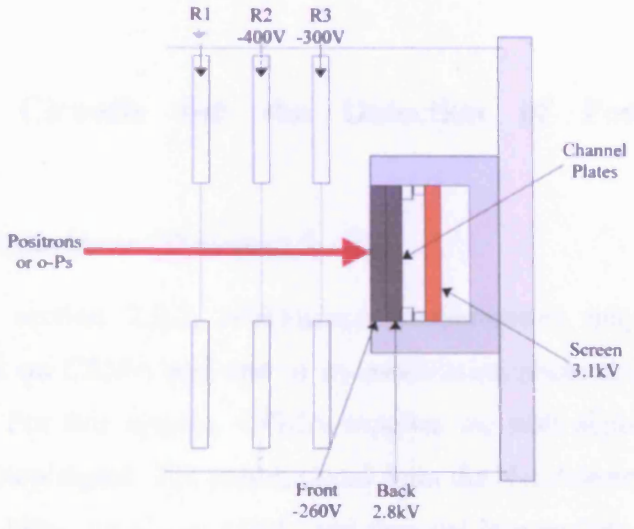

Figure 2.10: Schematic of CEMA.

2.6.3 Gamma-Ray Detectors

Coincidence measurements may be acquired between a e^+ incident on CEMA and one of its annihilation photons. A NaI detector (see figure 2.11) is used to detect these annihilation photons. The detector consists of a scintillator crystal (150mm diameter and 80mm width) attached to a photomultiplier tube via a 1m long light pipe, which allows the detector to be located in a region of lower magnetic field.

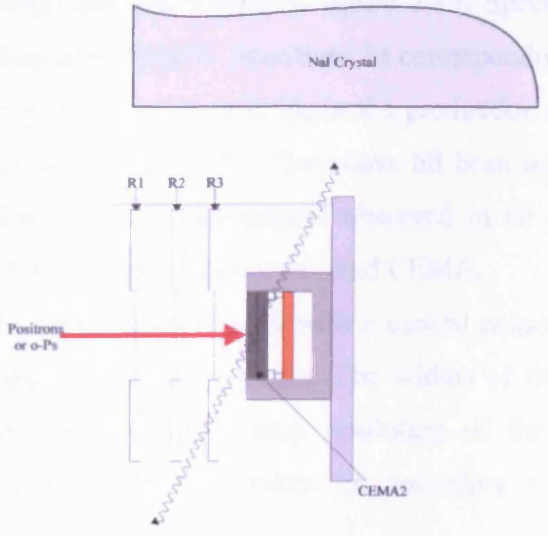

Figure 2.11: Schematic diagram of the position of the NaI detector with respect to CEMA.

The gamma-ray detector is placed perpendicularly to the detector chamber and as close to CEMA as possible (as shown in figure 2.11), in order to maximize the detection solid angle.

2.7 Electronic Circuits for the Detection of Positrons and Positronium

2.7.1 CEMA/NaI Coincidence Detection System

As stated in section 2.6.3, coincidence measurements may be achieved between a e^+ incident on CEMA and one of its annihilation photons incident on the gamma-ray detector. For this system, CEMA supplies the start signal and the NaI detector supplies the stop signal. The output signal from the NaI detector is inverted in an Ortec 474 Timing Filter Amplifier (TFA) and then fed into an Ortec 463 Constant Fraction Discriminator (CFD). The output signal from the CFD is delayed by 500ns before being used as the stop pulse for an Ortec 437A Time to Amplitude Converter (TAC). The pulses from CEMA are acquired from the screen (figure 2.10) via a capacitor, which is terminated by a 3.5kΩ resistor. The pulses are then sent to a fast (x10) pre-amplifier, after which they are fed through an Ortec 584 CFD to the start input of the TAC. The output from the TAC is then fed into a PC-based multichannel analyzer (Ortec MCA). A block diagram of the electronics is shown in figure 2.12, and examples of the CEMA/NaI coincidence spectra for the incident e^+ beam, incident Ps beam and the background are shown in figure 2.13. Spectrum a) was acquired using an incident e^+ beam of 38.6eV. Spectrum b) corresponding to Ps of 30eV was attained by neutralizing the e^+ beam with H_2 in the production cell. Spectrum c) was obtained with vacuum in both gas cells. They have all been normalized to the same run time of 1000s. The uniform background observed in all the spectra is due to random coincidences between the NaI detector and CEMA.

The spectra all have similar shapes with a central coincidence peak; the only difference is in the magnitude of the peaks. The widths of the peaks arise from a significant contribution due to the timing resolution of the NaI detector and a negligible contribution from the time taken for secondary e^- to pass through the channel plates.

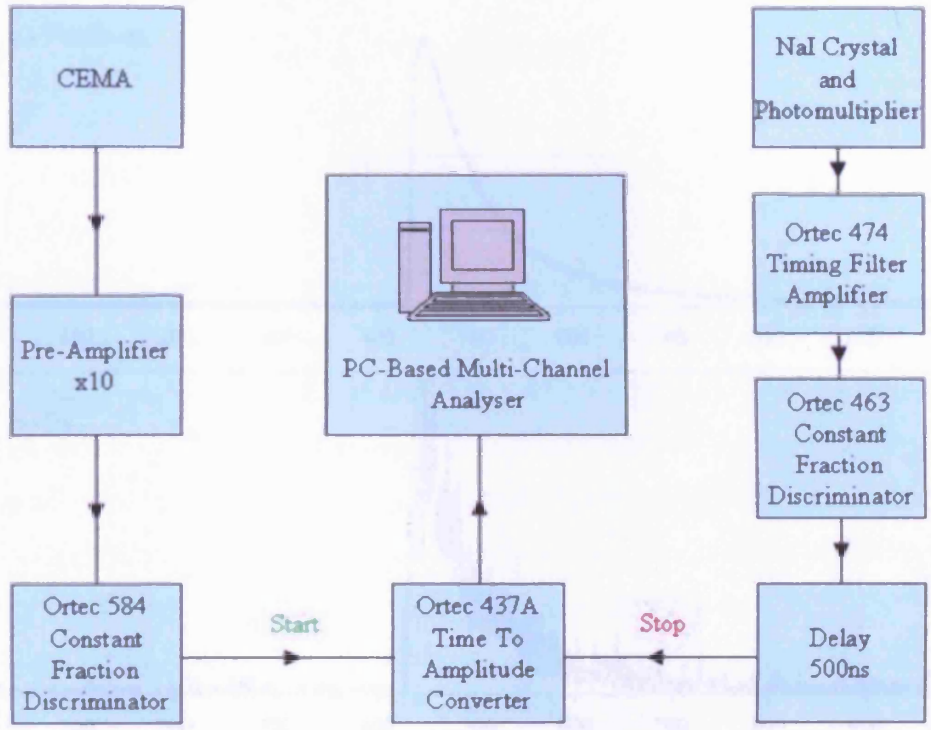

Figure 2.12: Block diagram of the electronics for the CEMA/NaI coincidence detection system.

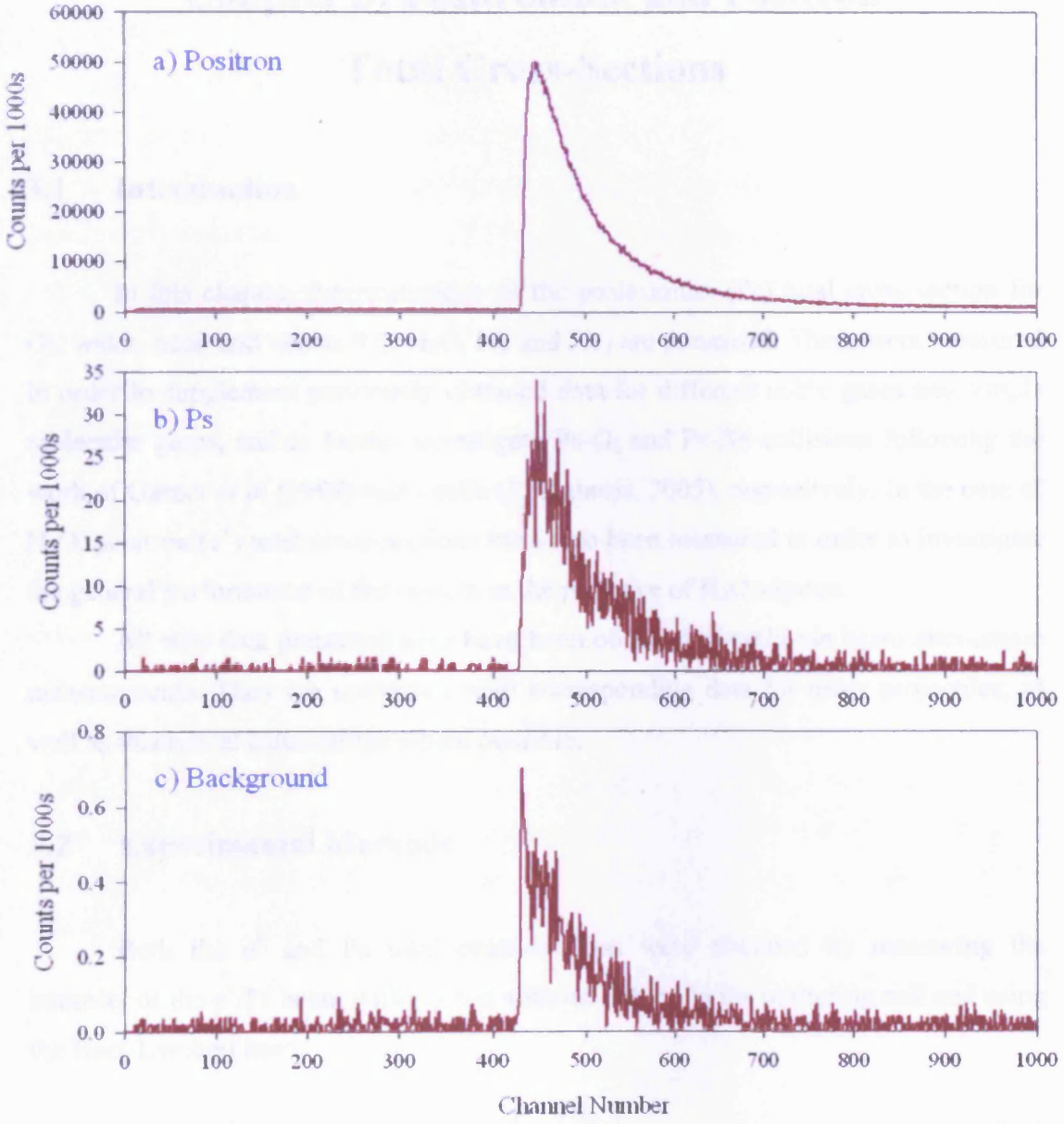

Figure 2.13: Typical CEMA/NaI coincidence spectra for a) incident e^+ beam, b) incident Ps beam and c) background.

Chapter 3: Positronium and Positron Total Cross-Sections

3.1 Introduction

In this chapter, determinations of the positronium (Ps) total cross-section for O_2, water, neon and xenon (O_2, H_2O, Ne and Xe) are presented. These were measured in order to supplement previously obtained data for different noble gases and simple molecular gases, and to further investigate Ps-O_2 and Ps-Xe collisions following the work of Garner *et al* (1998) and Leslie (PhD thesis, 2005), respectively. In the case of H_2O, positron (e^+) total cross-sections have also been measured in order to investigate the general performance of the system in the presence of H_2O vapour.

All new data presented here have been obtained directly via beam attenuation measurements. They are compared with corresponding data for other projectiles, as well as theoretical calculations where possible.

3.2 Experimental Methods

Both the e^+ and Ps total cross-sections were obtained by measuring the intensity of the e^+/Ps beam with (I) and without (I_0) gas in the scattering cell and using the Beer-Lambert law:

$$\sigma_T = \frac{kT}{Pl} \ln\left(\frac{I_0}{I}\right), \tag{3.1}$$

where k is the Boltzmann constant, T is the ambient temperature and P is the pressure of the target gas in a scattering cell of effective length l (determined as discussed in section 3.3.1).

The measurements were made using the coincidence detection system consisting of a NaI gamma-ray detector and a CEMA, as described in section 2.7.1. During the investigation, the ambient temperature of the laboratory was kept stable to within ±1K by an air conditioning unit in the laboratory and the gas pressures were monitored continuously by a computer via a capacitance manometer.

3.2.1 Method for Ps-O_2, Ne and Xe

For each energy investigated, several measurements were conducted at different gas pressures, ranging from 0-6μmHg (0-0.8Pa), and the weighted mean of the data used to calculate the total cross-section. Before and after each Ps run, the incident e^+ beam flux was monitored for 10s, so that any variation in the intensity could be taken into account during the analysis. The incident Ps was produced by introducing gas in the production cell: molecular hydrogen (H_2) or molecular nitrogen (N_2) (depending on energy under investigation, as discussed in section 2.5.1), both at pressures of ~10μmHg (1.3Pa). Measurements of the incident Ps beam were alternated to those of the Ps beam transmitted through the scattering cell containing the gas under investigation. Due to the variation of the Ps beam intensity with kinetic energy, the total run time varied between 1-8 days at each incident energy (time needed to obtain acceptable statistical errors). Measurements in vacuum (i.e. with no gas in either the production or the scattering cells) have been performed to account for random coincidences between detectors (see section 2.7) and for those due to fast particles emanating from the source. This background was subtracted from the recorded incident and transmitted beam intensity.

With reference to figure 2.1, during the Ps measurements, a potential of 200V was applied to CR1, so that any residual slow e^+ exiting the production cell would be reflected and prevented from entering the scattering cell and forming Ps. The potential on R1, in front of CEMA, was set so that any e^+ resulting from Ps fragmentation upon the gas in the scattering cell or upon surfaces before the detector would be repelled. It is crucial that the potential on R1 should be greater than the potential on CR1 (e.g $V_{R1} \geq V_{CR1} + E_R$, where $E_R = E_{Ps} - 6.8eV$) to prevent events which arise from Ps fragmenting in the region between CR1 and the earth grid being recorded.

3.2.2 Method for e^+-H_2O and Ps-H_2O

The Ps and e^+ total cross-sections for H_2O were measured over the energy ranges (7–417)eV and (10–100)eV, respectively. During all measurements, the gas pressure within the scattering cell was maintained at 0.38±0.04μmHg (0.05±0.01Pa). A new aluminium (Al) cell, as discussed in detail in section 3.3.2, was constructed

with which incident Ps beam attenuations of (86 to 90)% were achieved. The evacuation time for H_2O vapour was measured by monitoring the time taken for the incident positron beam count rate to return to its normal level after stopping the inflow of H_2O in the scattering cell. The average time taken was found to be ~10min and therefore an equivalent time delay was introduced between the measurements of the incident and transmitted beams. This delay was controlled by a program designed, using LabVIEW, to conduct all measurements.

For the range of energies in this study, H_2 was used within the production cell at a pressure of (9–11)μmHg (1.2–1.5Pa) to generate the incident Ps beam. The incident Ps flux was recorded between measurements of the transmitted Ps beam with H_2O in the scattering cell. As discussed in section 3.2.1, before and after each incident and transmitted Ps measurement, the incident e^+ beam intensity was monitored for 10s. For the Ps total cross-sections, background measurements were also made i.e. with vacuum in both cells such that this contribution could be subtracted from the incident and transmitted measurements to account for random coincidences between detectors and those due to fast e^+ emanating from the source. For determination of the e^+ total cross-section, the incident beam was measured with vacuum in both cells and the transmitted beam was measured with vacuum in the production cell and H_2O in the scattering cell. Due to the variation in the Ps/e^+ count rate with kinetic energy, the total data-acquisition time was between 1–8 days and 0.6–1.5 hr, respectively, at each energy investigated (time needed to obtain acceptable statistical errors).

The grid, CR1, in front of the scattering cell (see figure 2.9) was used to define the lower limit of the energy distribution of the incident e^+ chosen to be ~3eV below the maximum energy of the beam (see appendix A for details). This limitation on the energy distribution was imposed before the scattering cell, so that residual e^+, from the lower portion of the energy distribution of the beam exiting the production cell, would be reflected and prevented from entering the scattering cell and forming Ps. The grids in front of CEMA were used to discriminate against forward scattered e^+ in the total cross-section measurements (details given in section 3.4.4). These grids were also used to stop any e^+/e^- (electrons) from Ps fragmentation within the scattering cell from reaching the CEMA (Armitage *et al*, 2002, 2006).

As used in other H_2O scattering experiments, a freeze-pump-thaw method (Rudd *et al*, 1985; Sağlam and Aktekin, 1990) was employed to remove residual gases (e.g. N_2) from the distilled H_2O prior to its introduction into the Al scattering cell (see

figure 3.1 for a schematic diagram). The method involved placing the distilled H_2O into an Al reservoir and using liquid nitrogen (LN_2) to freeze the H_2O and a roughing pump to remove any other gases. The gas line to the system was kept closed by a computer controlled valve throughout this procedure. Firstly, the gas line was pumped with tap 2 closed and tap 3 open. The H_2O was then put into the reservoir through tap 1 with tap 2 closed. Tap 1 was then closed and the reservoir was immersed in LN_2.

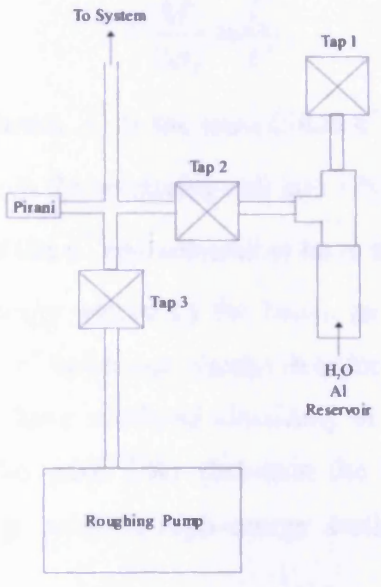

Figure 3.1: A schematic diagram of the setup used to purify the distilled H_2O.

Once the H_2O was frozen, tap 2 was opened and the other gases (e.g. N_2 and O_2) were pumped away for ~20mins. Afterwards, tap 2 was closed and the reservoir was brought back up to room temperature. This process was then repeated several times. The effectiveness of this procedure was verified by mass spectrometry on the electrostatic system, which also indicated the absence of H_2O clusters (see figure 5.11).

3.3 Length of the Effective Scattering Cell

3.3.1 Cell Length for O_2, Ne and Xe

As shown in figure 2.9 and described in section 2.6.1, for total cross-section measurements, a simple Al cylinder with brass apertures coated in graphite, to reduce

the emission of secondary electrons and to provide equipotential surfaces, was used for the scattering cell. The angular acceptance for the Ps beam detected at CEMA for this cell was 1.23°. The effective length for this scattering cell was determined by performing e^+ beam attenuation measurements and using known e^+ total cross-section, σ_T^+, values (Dababneh *et al*, 1980; Kauppila *et al*, 1981; Dababneh *et al*, 1988) according to:

$$l = \frac{kT}{P\sigma_T^+} \ln \frac{I_0^+}{I^+}, \tag{3.2}$$

where I_0^+ is the incident e^+ beam, I^+ is the transmitted e^+ beam, k is the Boltzmann constant, P is the gas pressure in the scattering cell and T is the ambient temperature.

The incident energy of the e^+ was selected to be in a region where σ_T^+ does not vary too much within the energy spread of the beam, as indicated in figure 3.2. A narrower energy spread of the e^+ beam was chosen in order to decrease the uncertainty introduced by e^+ which may have scattered elastically at small forward angles (see section 3.4.4 for details). The grids CR1 (between the cells) and R2 (before the CEMA detector) were used to select a high-energy section of the e^+ beam energy distribution.

For the example shown in figure 3.2, CR1 and R2 were set to Vs+7V i.e. 64V, which is indicated by the dashed line in figure 3.2a). This resulted in a count rate of ~$30e^+s^{-1}$. Figure 3.3 shows the results attained from e^+-gas attenuation measurements for a range of pressures, P=(0-9)μmHg (0-1.2Pa) for Ne. The effective cell length for this example is shown in table 3.1, along with measurements made for the other gases investigated in the scattering cell. As the results did not show any significant mass dependence, an average of the values was computed, yielding an effective cell length value of (6.64±0.08)cm. This value was then used for the determination of the Ne, Xe and O_2 total cross-sections.

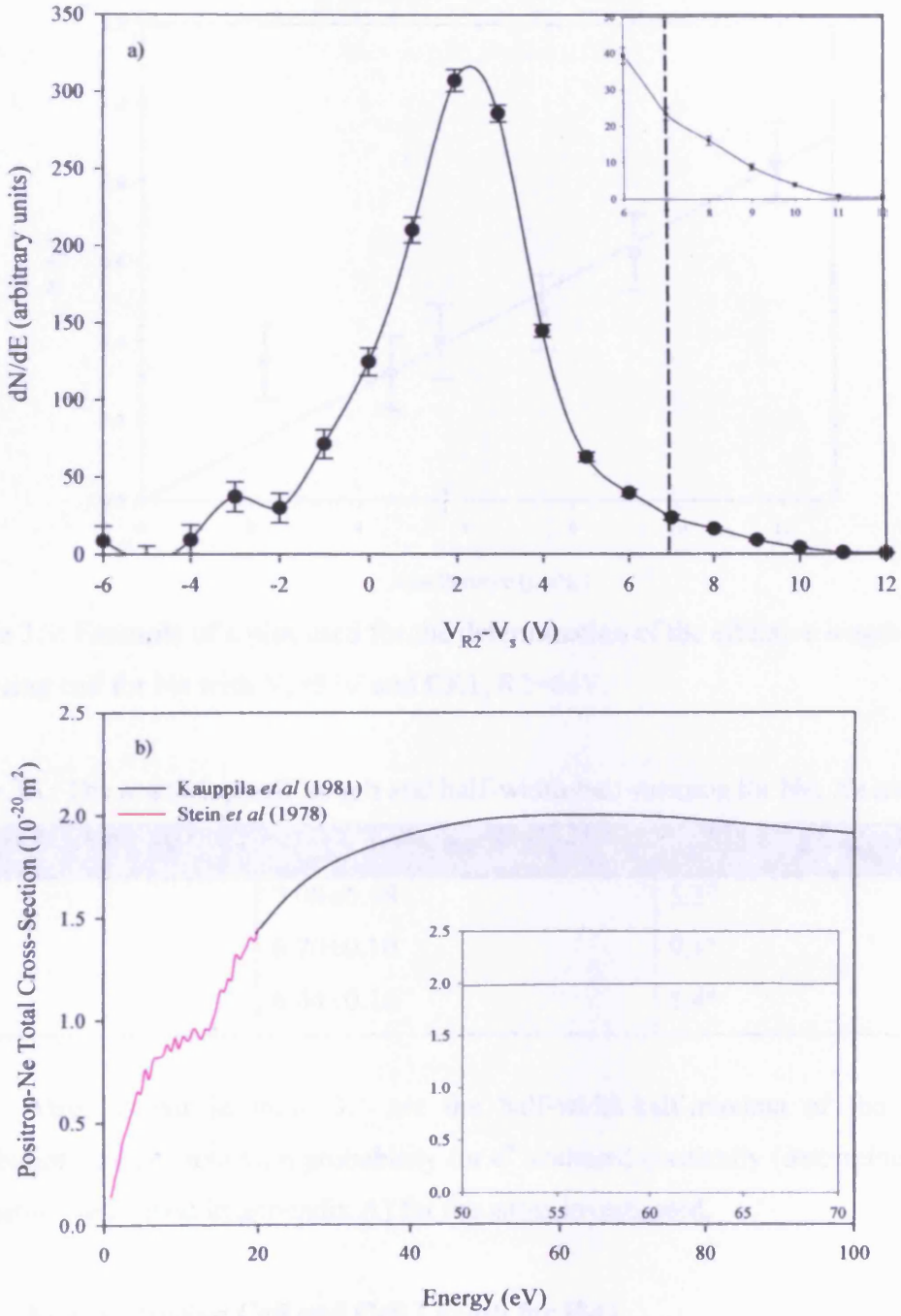

Figure 3.2: a) An example of a e^+ beam energy profile for V_s=57V and b) corresponding e^+-Ne total cross-section. Insets are expanded regions of interest.

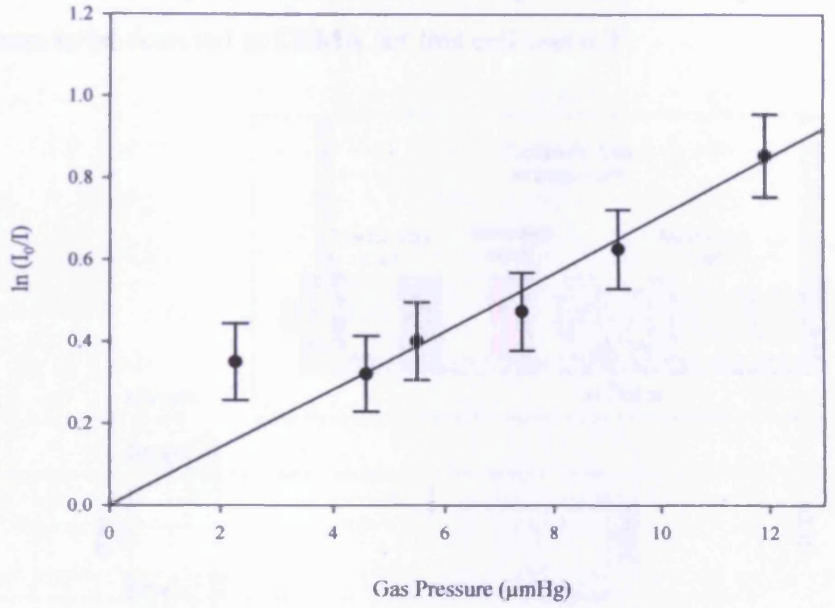

Figure 3.3: Example of a plot used for the determination of the effective length for the scattering cell for Ne with V_s=57V and CR1, R2=64V.

Table 3.1: The scattering cell length and half-width-half-maxima for Ne, Xe and O_2.

Gas in Scattering Cell	Scattering Cell Length (cm)	Half-Width-Half-Maxima
Ne	7.08±0.48	5.3°
Xe	6.70±0.10	9.1°
O_2	6.44±0.16	8.4°

Also, shown in table 3.1 are the half-width-half-maxima of the angular distributions of the detection probability for e^+ scattered elastically (determined using the method described in appendix A) for the gases investigated.

3.3.2 New Scattering Cell and Cell Length for H_2O

As mentioned in section 3.2.2, a new Al scattering cell was used in the case of H_2O. This scattering cell is shown schematically in figure 3.4, along with the cradle supporting the cells and the collars used to place the scattering cell on the cradle. The length of the cell body was 144mm, with the entrance and exit apertures each measuring 20mm. The diameters of the entrance and exit apertures were 6mm and

8mm, respectively, so designed to allow the full Ps beam to exit the cell and be detected without hitting the exit aperture and fragmenting. The angular acceptance for the Ps beam to be detected at CEMA for this cell was 0.9°.

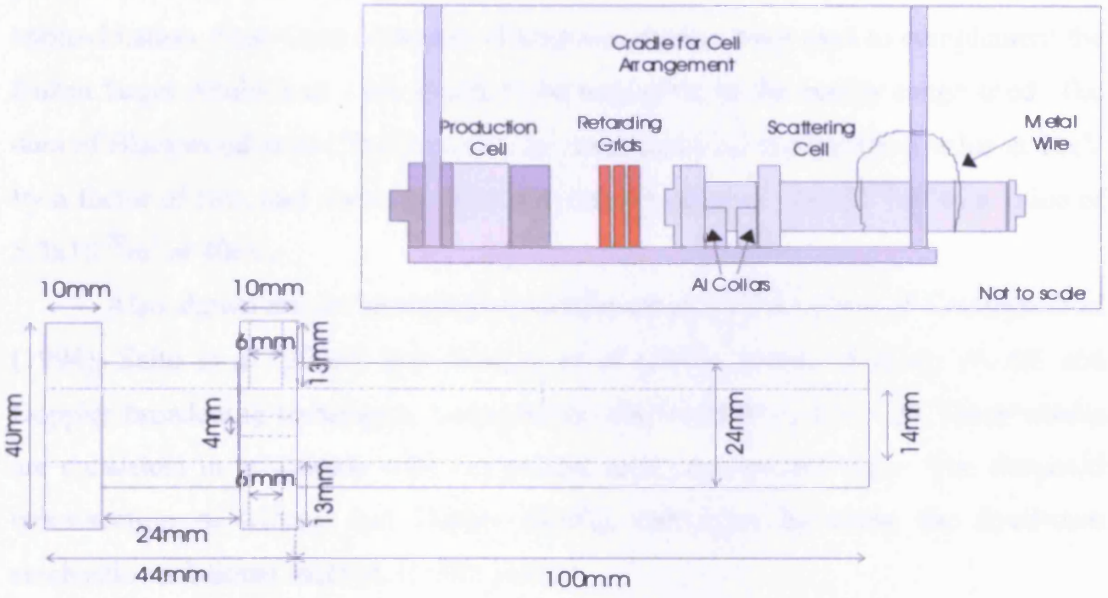

Figure 3.4: A schematic diagram of the scattering cell used for Ps-H_2O and e^+-H_2O total cross-sections without the apertures. The dotted lines represent the internal diameters. Inset shows the arrangement for the cells.

The effective cell length for this cell was 0.128±0.003m, as determined by measuring e^+-gas (Xe, O_2, and Ne) total cross-sections and normalizing these to known values (Dababneh *et al*, 1980; Kauppila *et al*, 1981; and Dababneh *et al*, 1988; respectively), in a similar fashion to the method discussed in section 3.3.1.

3.4 Results, Comparisons and Discussion

3.4.1 Ne

Total cross-section measurements for Ps scattering from Ne were performed in the energy range (10-250)eV. The present results, as in figure 3.5, show the cross-section to be roughly constant with energy in the range (10 to 100)eV with an average value of ~$4.3\times10^{-20}m^2$, decreasing above 100eV to an average value of ~$3.6\times10^{-20}m^2$.

The present results are compared with the theoretical target-elastic total cross-section results of Blackwood *et al* (2002), where it is assumed that the target atom remains unchanged in the collision. The calculation of Blackwood *et al* (2002) was performed using a full-electron coupled-state treatment of Ps within the frozen-target approximation. First Born estimates of target-excitation were used to complement the frozen target results and were found to be negligible in the energy range used. The data of Blackwood *et al* (2002) exceed the measured total cross-section value at 10eV by a factor of two, and decrease from a threshold value of ~$14\times10^{-20}m^2$ to a value of $5.3\times10^{-20}m^2$ at 40eV.

Also shown are the momentum transfer cross-section values of Coleman *et al* (1994), Saito *et al* (2003), and Skalsey *et al* (2003), measured using ACAR and Doppler broadening techniques, respectively (discussed in section 1.3). These results are consistent in magnitude with the present total cross-section data. The threshold cross-section of Mitroy and Ivanov (2002), calculated by using the fixed-core stochastic variational method, is also plotted.

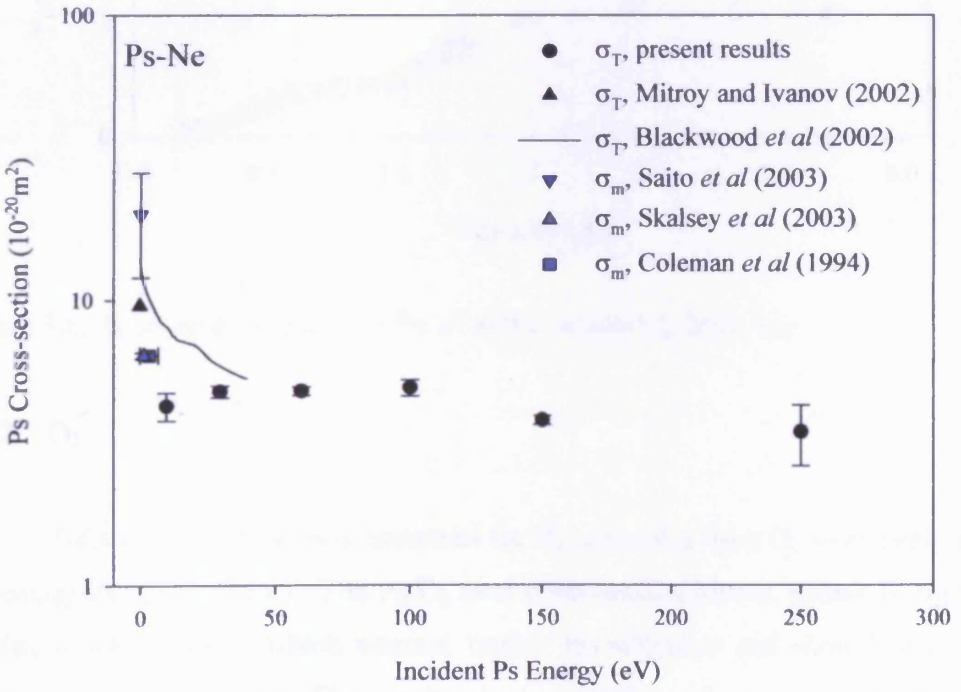

Figure 3.5: Cross-sections for Ps scattering from Ne.

In figure 3.6, the present Ps results are compared with values for equivelocity e^- and e^+ (Stein *et al*, 1978; and Kauppila *et al*, 1981). The e^- and e^+ total cross-sections both rise to a broad peak the former being a factor of two higher between (1.5

and 2.0)au. The e^- total cross-section decreases after ~1.9au, whereas the e^+ total cross-section stays roughly constant. The Ps-Ne total cross-section follows the e^--Ne total cross-section closely above 1.9au, but is slightly higher at and below this velocity. It is a factor of between seven to two higher than the e^+-Ne total cross-section between (0.6 and 3.0)au.

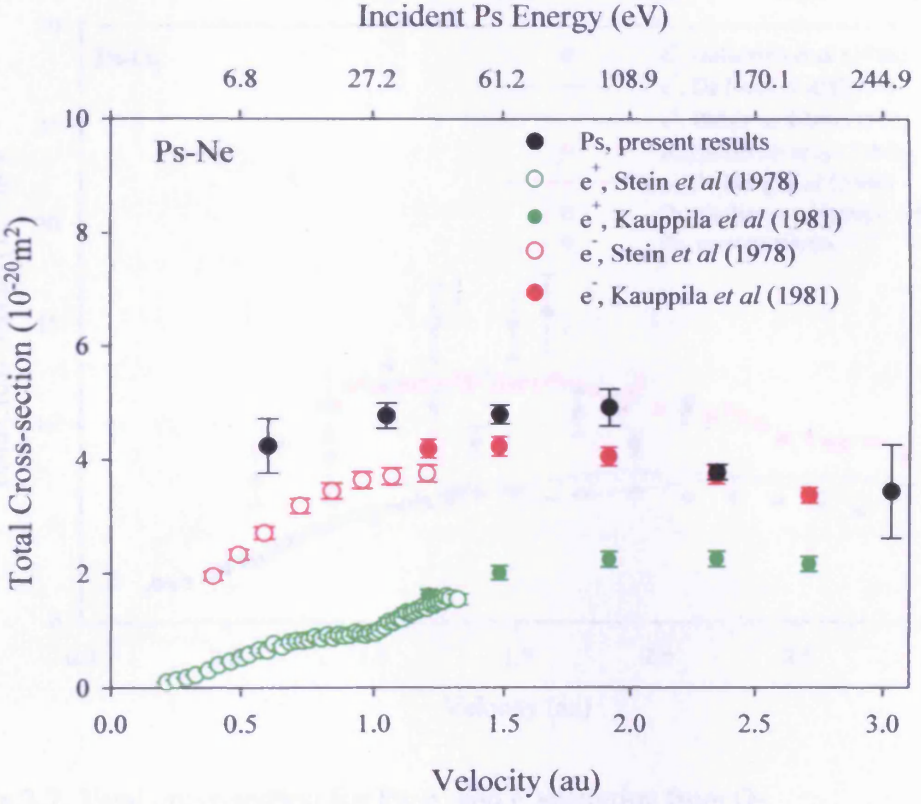

Figure 3.6: Total cross-section for Ps, e^+ and e^- scattering from Ne.

3.4.2 O_2

Total cross-section measurements for Ps scattering from O_2 were performed in the energy range 10-120eV. The Ps-O_2 total cross-section results, shown in figure 3.7, display a large scatter, which warrant further investigation and should therefore be considered as preliminary. The results show an increase from (7.1 to 12.8)x$10^{-20}m^2$ between 10eV and 30eV before decreasing to 9.0x$10^{-20}m^2$ at 50eV and increasing to ~15.3x$10^{-20}m^2$ between 60 and 70eV. The Ps results then decrease again to a constant value of ~10.0x$10^{-20}m^2$. This apparent structure has not been observed from other targets for which Ps scattering data are available where the total cross-sections

generally show an increase to a broad peak before decreasing towards higher energies. One possibility for the apparent structure could be quenching of Ps, as discussed below.

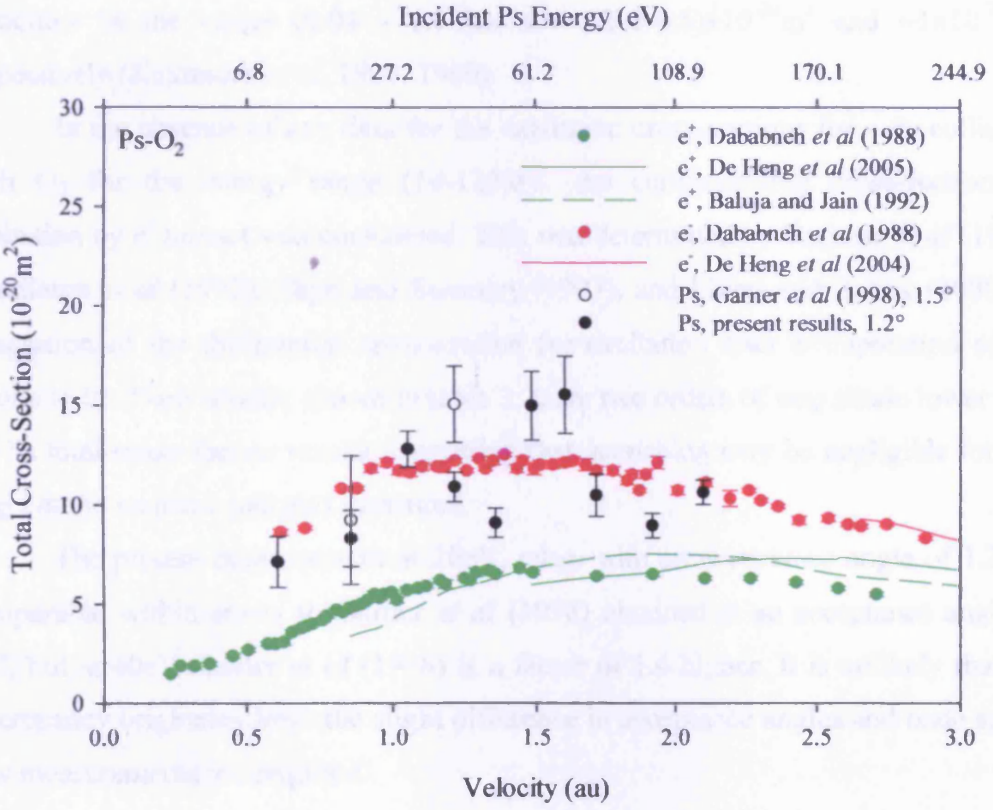

Figure 3.7: Total cross-section for Ps, e^+ and e^- scattering from O_2.

Ferrell (1958), Kakimoto *et al* (1987, 1990) and Shinohara *et al* (2001) discussed quenching by a paramagnetic gas such as O_2 converting o-Ps into p-Ps which then promptly self-annihilates. This can happen through several processes including the following inelastic reactions:

$$Ps(\uparrow\uparrow)+O_2\left(X^3\Sigma_g^-\right)(\downarrow\downarrow)\rightarrow Ps(\downarrow\uparrow)+O_2\left(a^1\Delta_g\right)(\uparrow\downarrow)\quad (E_{th}=0.98eV), \tag{3.3}$$

$$Ps(\uparrow\uparrow)+O_2\left(X^3\Sigma_g^-\right)(\downarrow\downarrow)\rightarrow Ps(\downarrow\uparrow)+O_2\left(b^1\Sigma_g^+\right)(\uparrow\downarrow)\quad (E_{th}=1.62eV), \tag{3.4}$$

where E_{th} represents the threshold energy.

Quenching can happen both inelastically and elastically, where inelastic conversion is due to electronic excitation of O_2 from the ground triplet state ($X^3\Sigma_g^-$) to the metastable excited singlet states ($a^1\Delta_g$ and $b^1\Sigma_g^+$) and elastic quenching occurs

when the O_2 remains in the ground state and the e^-, having parallel spins, are exchanged. Both processes involve the exchange of e^- with and without spin flip between the o-Ps and the O_2 molecule, as long as one or more e^- in the molecule are unpaired. The conversion cross-sections for inelastic and elastic processes for velocities in the range (0.04 - 0.18)au are $\sim(0.2\text{-}0.5)\times10^{-20}m^2$ and $\sim1\times10^{-23}m^2$, respectively (Kakimoto *et al*, 1987, 1990).

In the absence of any data for the excitation cross-sections for o-Ps collisions with O_2 for the energy range (10-120)eV, the corresponding cross-section for excitation by e^- impact was considered. This was determined by Trajmar *et al* (1971), Middleton *et al* (1992), Shyn and Sweeney (1993), and Linert and Zubek (2006) by integration of the differential cross-section for excitation after extrapolation of the results to 0°. Their results, shown in table 3.2, are two orders of magnitude lower than the Ps total cross-section results suggesting that quenching may be negligible for this target at the incident energies measured.

The present measurement at 20eV, taken with an acceptance angle of 1.2°, is comparable within errors to Garner *et al* (1998) obtained at an acceptance angle of 1.5°, but at 40eV Garner *et al* (1998) is a factor of 1.4 higher. It is unlikely that the discrepancy originates from the slight difference in acceptance angles and once again, new measurements are required.

Table 3.2: The integrated cross-section of the metastable excited singlet states for e^- impact on O_2.

Ref	Energy (eV)	$^1\Delta_g$ integrated cross-section ($10^{-22}m^2$)	$^1\Sigma_g^+$ integrated cross-section ($10^{-22}m^2$)
Trajmar *et al* (1971)	7	~9	~2
Middleton *et al* (1992)	10	11.8	3.7
Shyn and Sweeney (1993)	7	10.5	3.2
Linert and Zubek (2006)	10	5.9	

As no theoretical data are currently available for Ps-O_2, the results are compared with the e^- and e^+ total cross-section values of Dababneh *et al* (1988), as well as the theoretical total cross-section predictions for e^+-O_2 (Baluja and Jain, 1992; De-Heng *et al*, 2005) and e^--O_2 (De-Heng *et al*, 2004). The e^- total cross-section rises

smoothly to a broad peak at ~(1-2)au before decreasing slowly. The e^+ total cross-section increases smoothly through the Ps formation threshold (~0.6au), to a broad peak at ~(1.5-2.5)au before slowly decreasing. The Ps-O_2 total cross-section is comparable in magnitude to the e^--O_2 total cross-section across the whole energy range investigated, and is approximately a factor of 1.4 to 2.4 higher than the e^+ total cross-section. Neither the e^- nor the e^+ total cross-sections display the structure suggested by the Ps total cross-section.

Baluja and Jain (1992) used the spherical complex optical potential method to calculate the e^+ total cross-section for collisions with O_2. They are in fairly good agreement with the experimental data for the e^+ at and above 1.2au. De-Heng *et al* (2004, 2005) also used a complex optical potential, but included the concept of a bonded atom and incorporated the additivity rule to simplify it to an atomic scattering problem. Their e^+ data are comparable in magnitude to those of Dababneh *et al* (1988) and Baluja and Jain (1992). Their e^- data at the high energies are in very good agreement to the experimental data of Dababneh *et al* (1988).

3.4.3 Xe

Leslie (2005) performed preliminary measurements of total cross-sections for Ps scattering from Xe in the energy range (10-120)eV. The present measurements, which include Leslie (2005), completed this study in the energy range (10-100)eV. As shown in figure 3.8, the Ps total cross-section values increase from a value of $(16\pm3)\times10^{-20}m^2$ at 10eV to a broad peak from (30 to 50)eV, with an average value of $\sim29\times10^{-20}m^2$. Above 50eV, the data decrease to $\sim16.5\times10^{-20}m^2$. Also shown in the figure is the theoretical determination of the elastic cross-section by Blackwood *et al* (2002) obtained using a static-exchange approximation. The theoretical values decrease with energy, intersecting the experimental results at 20eV.

The zero energy cross-section of Mitroy and Bromley (2003), who used a fixed core stochastic variational method, is consistent in magnitude with the experimental data. An upper limit to the momentum transfer cross-section has also been determined by Nagashima *et al* (1995) from angular correlation measurements to be $120\times10^{-20}m^2$, which, along with the theoretical calculation of Blackwood *et al* (2002), suggests an increase in the cross-section at low energies.

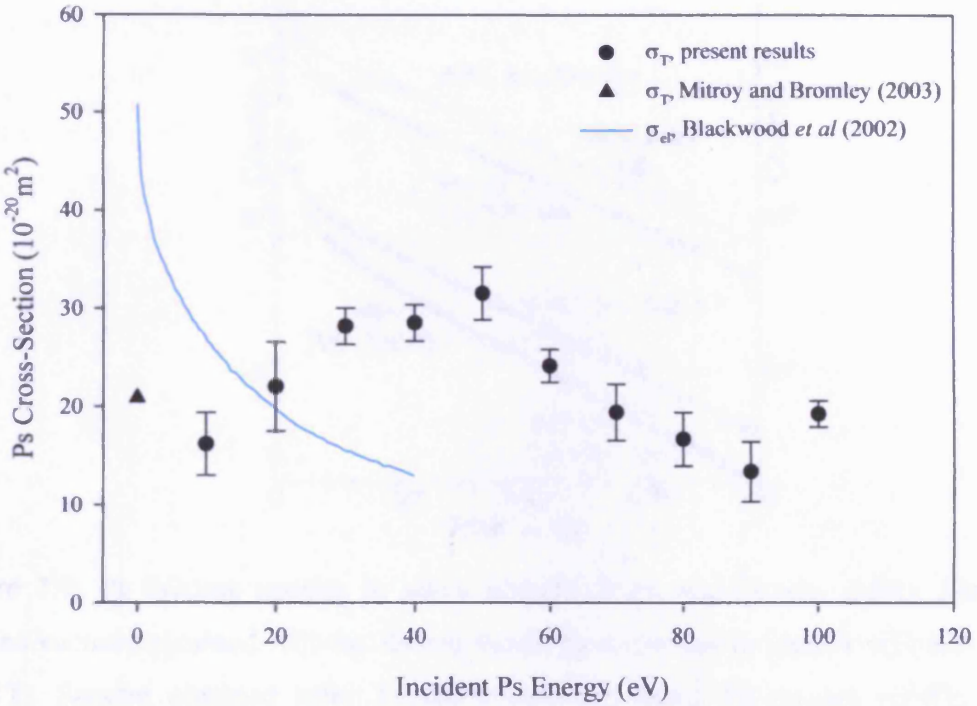

Figure 3.8: Cross-sections for Ps scattering from Xe.

In Xe, the anomalously low Ps fraction extracted from lifetime studies (Coleman *et al*, 1975) was interpreted by Mitroy and Novikov (2003) as arising from the quenching of o-Ps via spin-orbit interactions between the outer electrons of the Xe atom and the electron of the Ps. Spin-orbit interactions in Ps-Xe were detected by Saito and Hyodo (2006) by measuring the change in the lifetime of o-Ps in Xe when a magnetic field of 1T was applied. The principle behind this discussion is that if spin-orbit interactions do not exist then the lifetime of o-Ps would be independent of the magnetic field, whereas if they do exist then there would be a decrease in the lifetime of the o-Ps. Their results are shown in figure 3.9. In the presence of a vacuum, the lifetime was approximately the same with and without a magnetic field, whereas with Xe, the lifetime decreased significantly when the magnetic field was applied, giving evidence for spin-orbit interactions.

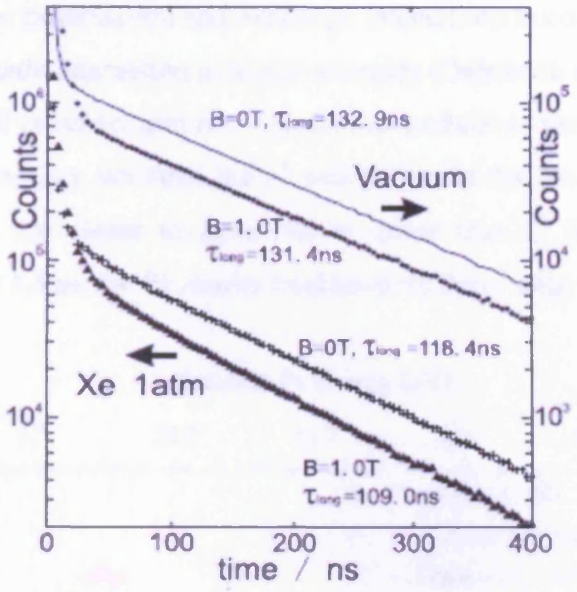

Figure 3.9: Ps lifetime spectra in silica aerogel (Saito and Hyodo, 2006). Spectra labeled vacuum obtained without Xe are shown by a continuous line (B=0T) and dots (B=1T). Spectra obtained after Xe introduced are shown by crosses (B=0T) and triangles (B=1T).

Mitroy and Novikov (2003) parameterized the spin-conversion cross-section for o-Ps quenching to p-Ps as

$$\sigma_{so}(k) = F_{so}\sigma_p(k), \tag{3.5}$$

where F_{so} is the conversion probability per elastic p-wave collision taken to be 0.00053 (Mitroy and Novikov, 2003) and $\sigma_p(k)$ is the functional form for the p-wave elastic cross-section calculated from the effective range expression for the p-wave phase shift, δ_1, for Ps-H scattering in the electron spin triplet state (Adhikari and Mandal, 2000). By calculating the sum of the partial wave elastic cross-sections for $L \geq 1$, for the energy range (10-60)eV (Adhikari and Mandal, 2000), the spin conversion cross-section is estimated to be $\sim(2.34 - 0.05)\times10^{-23}m^2$. Therefore, for Ps-Xe, quenching is unlikely to contribute to the total cross-section.

In figure 3.10, the Ps results are compared with the e^- and e^+ total cross-section values of Dababneh *et al* (1980, 1982). The e^- total cross-section rises rapidly before exhibiting a shoulder between (0.6 and 0.8)au; this is followed by a rapid decrease above ~1.3au. The e^+ total cross-section decreases rapidly from $\sim31\times10^{-20}m^2$ at 0.15au to $\sim10\times10^{-20}m^2$ at 0.55au. After the Ps formation threshold (at ~0.6au), it increases rapidly to a broad peak, merging with the e^- total cross-section at ~1.8au. This is

thought to be due to the polarization and exchange interactions becoming negligible in comparison with the static interaction at higher energies (Dababneh *et al*, 1982).

The Ps-Xe total cross-section has a similar magnitude to the e^--Xe total cross-section above 1.4au and lies between the e^+ and e^- data in the intermediate velocity range. The Ps values are closer to those for e^- rather than e^+ for high velocities (>1.3au), whilst below 1.3au, the Ps results tend towards the e^+ data.

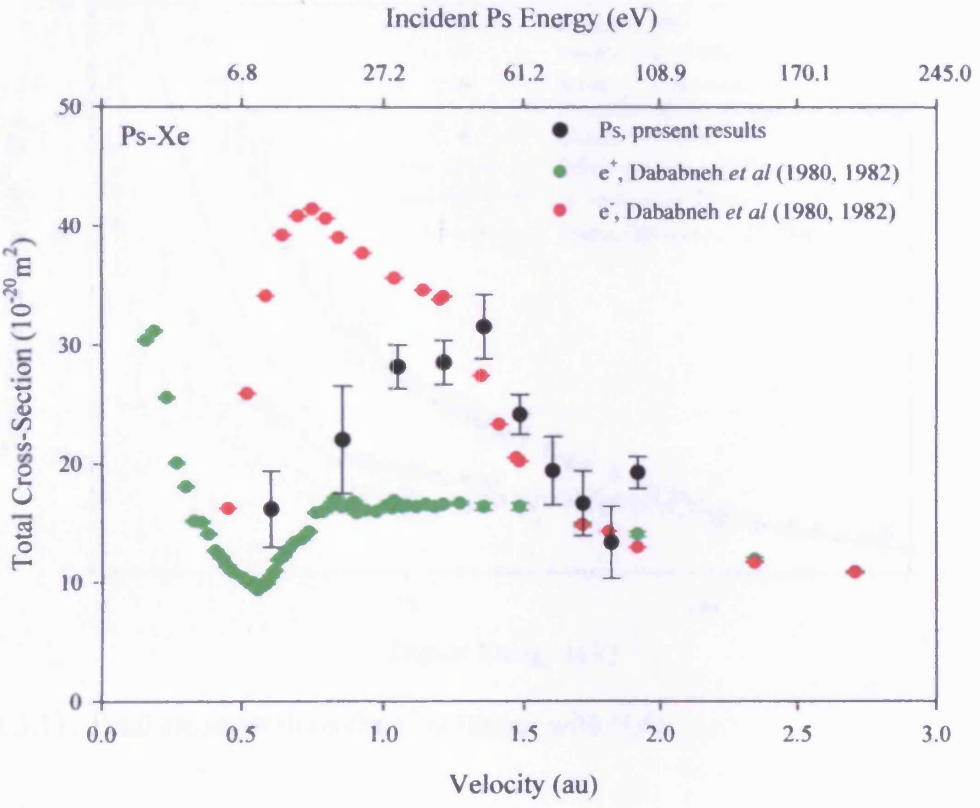

Figure 3.10: Total cross-section for Ps, e^+ and e^- scattering from Xe.

3.4.4 e^+-H_2O

The e^+ total cross-section results are shown in figure 3.11 where they are compared with previous values from experiment (Sueoka *et al*, 1986; Kimura *et al*, 2000; and Zecca *et al*, 2006) and theory (Baluja and Jain, 1992; Gianturco *et al*, 2001; and De Heng *et al*, 2005). For e^- scattering from polar molecules such as H_2O, the contribution of small-angle forward scattering is very large (Okamoto *et al*, 1993; and Yuan and Zhang, 1992) due to the long range of the interaction resulting in strongly forward-peaked differential cross-sections for elastic and inelastic processes (e.g. Jung

et al, 1982; and Itikawa and Mason, 2005). Therefore, forward scattering effects are also expected to be important for e^+ (Kimura *et al*, 2000). Hence, Kimura *et al* (2000) corrected the e^+ data of Sueoka *et al* (1986), which had been determined using a time-of-flight method. They assumed that differential cross-sections for e^+ are the same as for e^-. However, in the absence of explicit differential cross-sections for e^+, the present results have not been corrected for forward scattering and are presented as raw data.

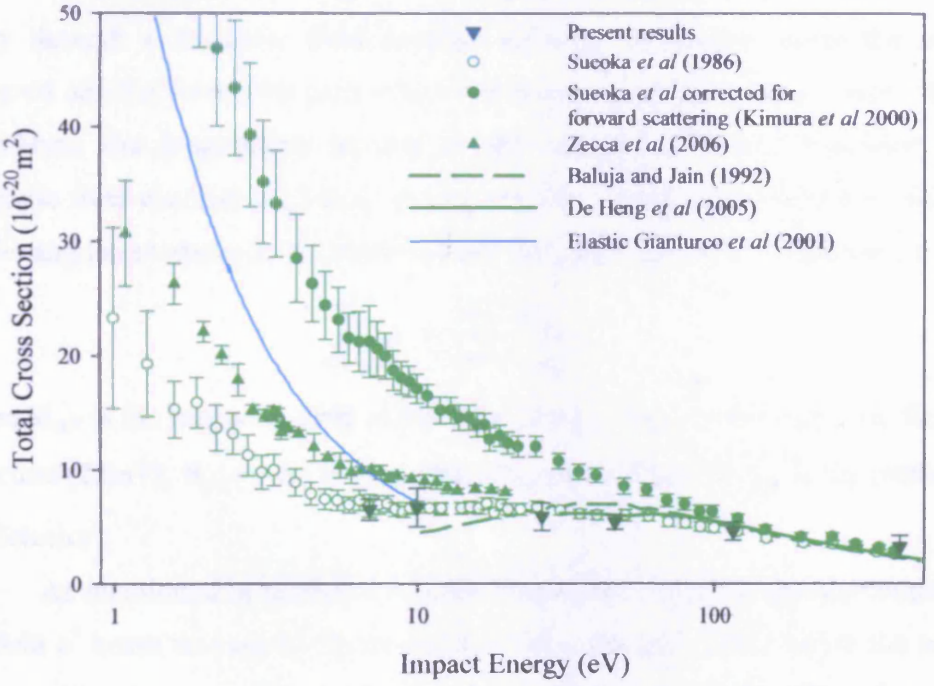

Figure 3.11: Total cross-sections for e^+ colliding with H_2O.

As shown in figure 3.11, the present data show little energy dependence over the range investigated and are in very good agreement with the original results of Sueoka *et al* (1986) i.e. before the correction for forward scattering (Kimura *et al*, 2000). After the correction, their cross-section increases by up to a factor of four. Both the present results and those of Sueoka *et al* (1986) are lower than the close-coupling results for the elastic cross-section calculated by Gianturco *et al* (2001), who used an *ab-initio*, parameter free, model for the quantum treatment of positron annihilation in H_2O at room temperature, where the internal degrees of freedom associated with the nuclei (e.g. rotations and vibrations) and the permanent excitation of electronic states were essentially excluded.

At higher energies, the present results are in fairly good agreement with the calculation of Baluja and Jain (1992) who used a spherical-complex-optical-potential

method along with a molecular wavefunction for a variety of molecules. However, Baluja and Jain (1992) state that their results may not be reliable for polar molecules at energies below 50eV. At intermediate and high energies, the experimental data are also in agreement with the calculation of De-Heng *et al* (2005) who used a complex-optical-potential approach and applied the additivity rule for the cross-sections of the constituent atoms.

Partial discrimination against forward scattering was implemented within this study through a magnetic field gradient between the region where the scattering occurred and the detector region where the retarding grids R2 and R3 were employed to analyze the longitudinal energy of the scattered positron. Provided that the magnetic field changes negligibly during one revolution of the helical motion of the e^+, the angular momentum is conserved and the pitch angle varies according to:

$$\frac{B_{cell}}{B_{CEMA}} \propto \frac{\sin^2 \theta_{cell}}{\sin^2 \theta_{CEMA}}, \tag{3.6}$$

where B_{cell} is the magnetic field at the cells (4mT), B_{CEMA} is the magnetic field at the detectors (22mT), θ_{cell} is the pitch angle within the cell and θ_{CEMA} is the pitch angle at the detector.

As mentioned in section 3.2.2, the lower limit of the energy distribution of the incident e^+ beam was set by the potential (V_r) on the grid, CR1, before the scattering cell, resulting in an energy distribution from eV_r to (eV_r + 3eV). Therefore, forward scattered e^+ with a longitudinal energy below eV_r were repelled by the potential V_r also applied to the grids, R2 and R3, in front of CEMA.

The angular variation of the detection probability of e^+ forward scattered at an angle θ_{cell} was calculated as discussed in detail in appendix A. The results are plotted in figure 3.12 at various e^+ incident energies and their half-width-half-maxima are shown in table 3.3.

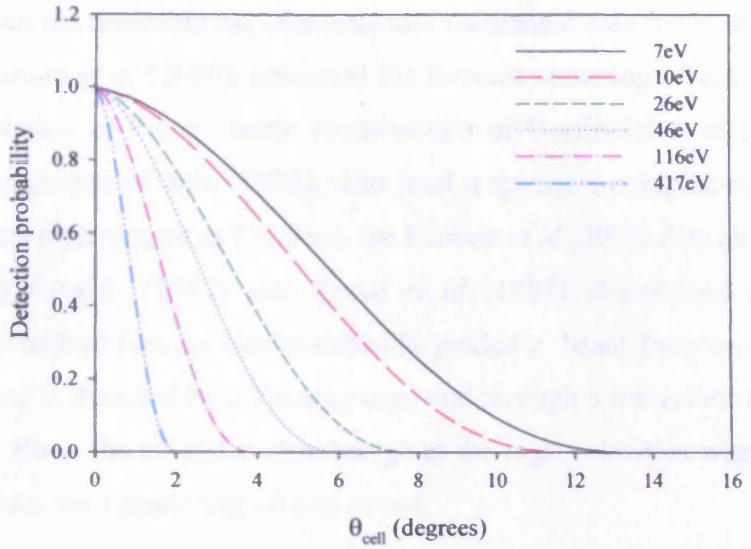

Figure 3.12: Dependence of the detection probability upon scattering angle at each incident e^+ energy investigated.

Table 3.3: The half-width-half-maxima (HWHM) of the angular distributions of the detection probability displayed in figure 3.12.

e^+ incident energy (eV)	HWHM (degrees)
7	5.8
10	5.1
26	3.4
46	2.5
116	1.6
417	0.9

3.4.5 Ps-H_2O

The results for the total cross-section for Ps scattering from H_2O are shown in figure 3.13 along with the results obtained for e^+. As can be seen from the figure, the present Ps data show little energy dependence over the range investigated and are a factor of two higher than those for e^+. This is different from most previously investigated targets, where the total cross-section generally exhibits a broad peak at low energies.

It is unclear what role forward scattering effects play in the case of Ps projectiles, but it would be expected to be minor in comparison with the case for e^- and e^+, since Ps is neutral and its detection upon scattering is limited to angles $\leq 1°$.

The Ps and e^+ total cross-sections are shown in figure 3.14 where they are compared with the available experimental and theoretical data for both e^+ and e^-. The e^- data of Kimura *et al* (2000), corrected for forward scattering effects, follow the *R*-matrix calculation of the e^- elastic cross-section of Gorfinkiel *et al* (2002) and the theoretical prediction of Jain (1988), who used a spherical-complex-optical-potential method. At the high velocities (>1.4au), the Kimura *et al* (2000) data also follow the e^- data of Szmytkowski (1987) and Zecca *et al* (1987), determined using a linear transmission method (i.e. an electrostatically guided e^- beam from an e^- gun scatters off the gas and is detected by a Faraday cup) and through a Ramsauer-type apparatus, respectively. Both, the e^+ and e^- data merge at the high velocities whether they were corrected for forward scattering effects or not.

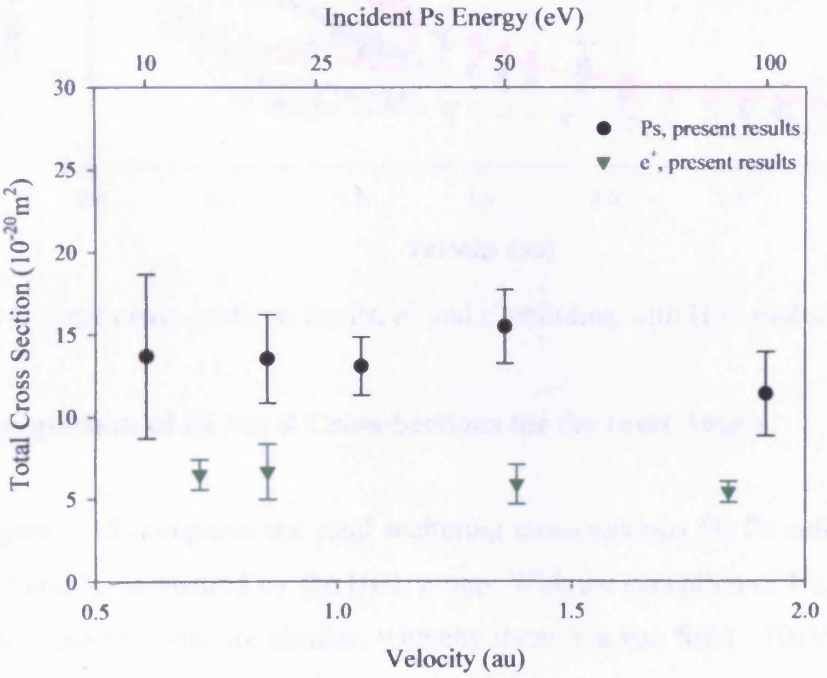

Figure 3.13: Total cross-sections for Ps and e^+ colliding with H_2O molecules.

The data of Zecca *et al* (2006) for e^+, determined using a e^+ spectrometer, are slightly higher than those for Sueoka *et al* (1986) and have a similar shape. For the lowest velocities the e^+ data, whether or not corrected for forward scattering, are similar in shape and magnitude to the close-coupling results for the elastic cross-section calculated by Gianturco *et al* (2001). For higher velocities, the Ps results are comparable with the experimental e^- data of Szmytkowski (1987) and Kimura *et al*

(2000) and the theoretical calculation of Jain (1988). Below ~1.2au, the Ps data fall below the e^- data and the results of Gorfinkiel *et al* (2002).

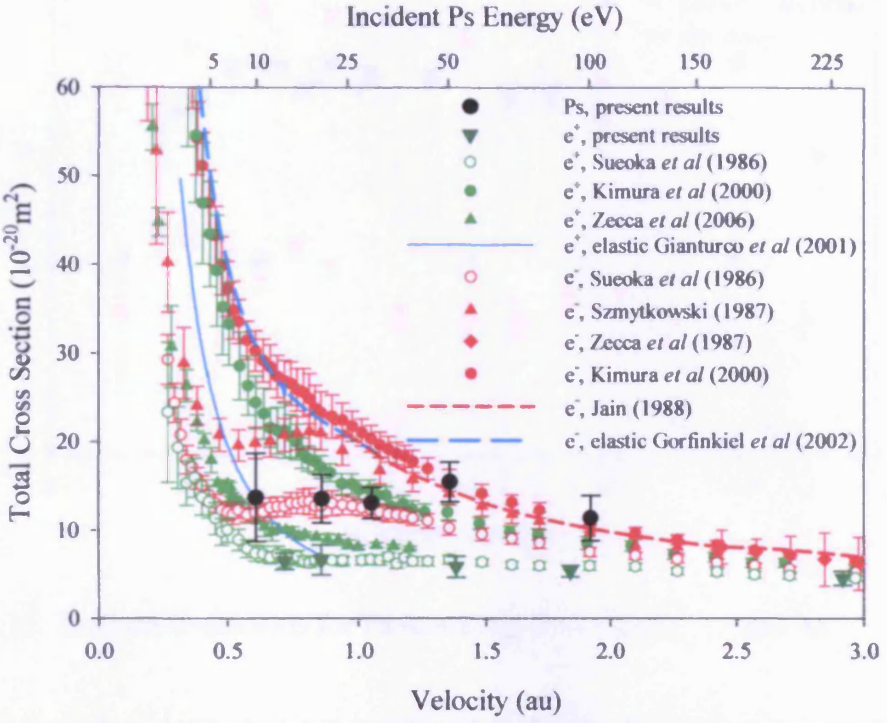

Figure 3.14: Total cross-sections for Ps, e^+ and e^- colliding with H_2O molecules.

3.4.6 Comparison of Ps Total Cross-Sections for the Inert Atoms

Figure 3.15 compares the total scattering cross-sections for Ps collisions with He, Ne, Ar and Xe measured by the UCL group. With the exception of Ne, the shapes of the total cross-sections are similar, whereby there is a rise from ~10eV to a broad peak, with the magnitude and width of the peak growing with increasing complexity of the target gas. For Ne, the data could be said to be roughly constant over the energy range investigated. The Ne and He (helium) total cross-sections have a similar magnitude, whereas Xe has the highest cross-section. Xe and Ar (argon) have a broad peak between 30 and 50eV, whereas He has a peak at approximately 20eV. For He the total cross-section decreases to an approximately constant value at higher energies.

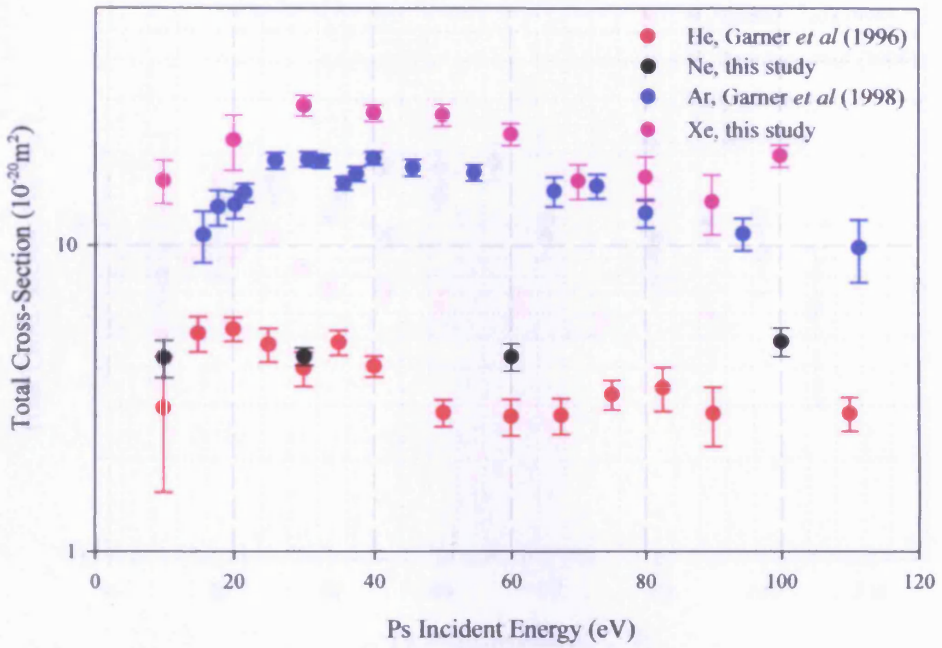

Figure 3.15: Total cross-sections for Ps scattering from He, Ne, Ar and Xe.

3.4.7 Comparison of Ps Total Cross-Sections for the Molecular Gases

In figure 3.16, the Ps total scattering cross-sections for collisions with H_2, N_2, O_2 and H_2O measured by the UCL group are plotted on the same axes for comparison. The total cross-section for H_2O is constant within errors over the energy range investigated, with a magnitude similar to the cross-section for N_2 and O_2. For N_2 and H_2, the total cross-section shows a rapid rise from 10eV to a broad peak, where the magnitude and width is greater for N_2 than for H_2. The magnitude of the total cross-section for O_2 is comparable to that for N_2 at all energies, except at 50eV where N_2 is higher by a factor of ~1.7.

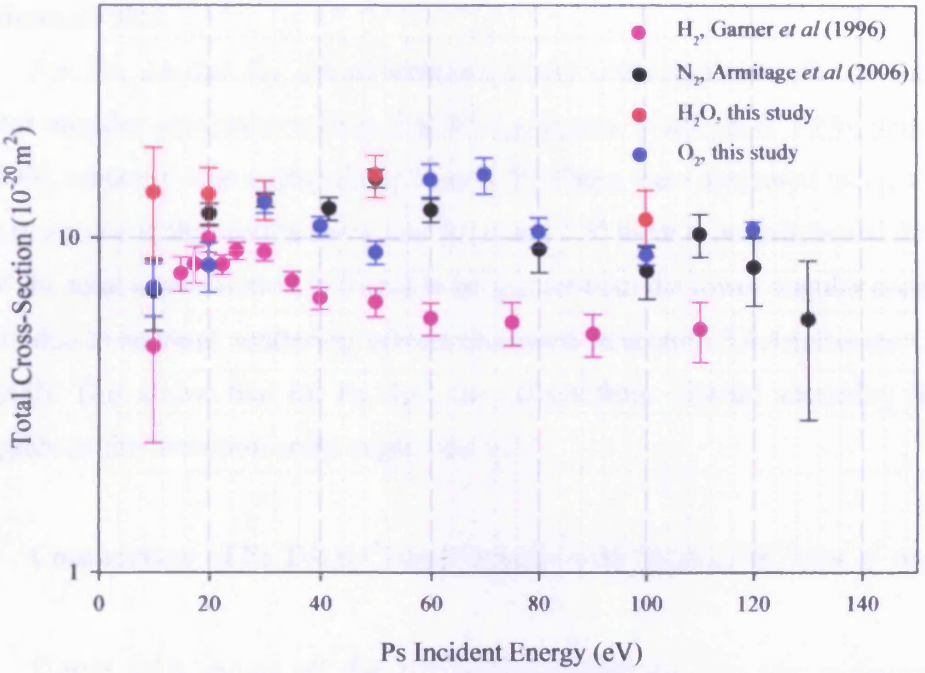

Figure 3.16: Total cross-sections for Ps scattering from H_2, N_2, O_2 and H_2O.

3.4.8 Comparison of Ps Total Cross-Sections with Available Theories and Momentum Transfer Cross-Sections

In figure 3.17, the Ps total scattering cross-sections are shown along with available theories and momentum transfer cross-sections. Apart from the data for He, the theories have a different shape to the experimental results, where generally the experimental data increase at low energies and the theories decrease. For He, the theory of Biswas and Adhikari (1999), determined using a 3-Ps-state close-coupling calculation and the first Born approximation, follows the experimental data below ~80eV. The results of Blackwood *et al* (2002) for the target elastic cross-section, calculated using a full-electron coupled-state treatment of Ps, are higher than the experimental results for Ne for all energies. For Xe and Ar, the theory intersects the experimental data at 20eV. The target inelastic cross-sections of McAlinden *et al* (1996), determined using the first Born approximation, are lower than the experimental results for He and Ar for energies greater than 20eV. This is also true for the theoretical determination of Biswas and Adhikari (2000) for H_2, whilst the

momentum transfer cross-section results are consistent with the magnitude of the experimental data.

For He, Ar and H_2, the experimental total cross-section is shown for various detector angular acceptances from 0 to 6° (i.e Garner *et al*, 2000, 1996; and Zafar *et al*, 1996), where 0° was extrapolated from 1.5°. These were measured using a time-of-flight method and the results show that for 0 and 1.5° there is no substantial difference. For 6° the total cross-section is found to be greater than the lower angular acceptances. This is due to forward scattering effects discussed in section 3.4.4 (also see Garner *et al*, 2000). This shows that for Ps-H_2O, the effects from forward scattering should be negligible as the detection solid angle was ≤1°.

3.4.9 Comparison of Ps Total Cross-Sections with those of H atom, e^+ and e^-

Figure 3.18 shows all the available experimental Ps total scattering cross-sections for collisions with atomic and molecular gases plotted along with those for other projectiles, namely H atom, e^+ and e^-. It can be seen that for He, Ar, Xe and H_2, at high velocities, the Ps total cross-section approximately follows that of the e^- total cross-section. At the lower velocities (<1.2au), the Ps data are found to lie between the e^+ and e^- results for these noble and molecular gases. At intermediate energies the Ps total cross-section for all targets is found to be greater than the e^+ data and for most atomic and molecular targets Ps scattering is similar to e^- scattering for high velocities and for some targets across the whole range of velocities investigated (e.g. O_2 and Ne).

The H atom data of Newman *et al* (1986), Johnson *et al* (1988) and Gao *et al* (1989), determined by integrating differential cross-sections over all angles (0-180°), have similar magnitudes to the Ps data for all targets and follow a similar trend to the Ps theories in figure 3.17 at the low energies.

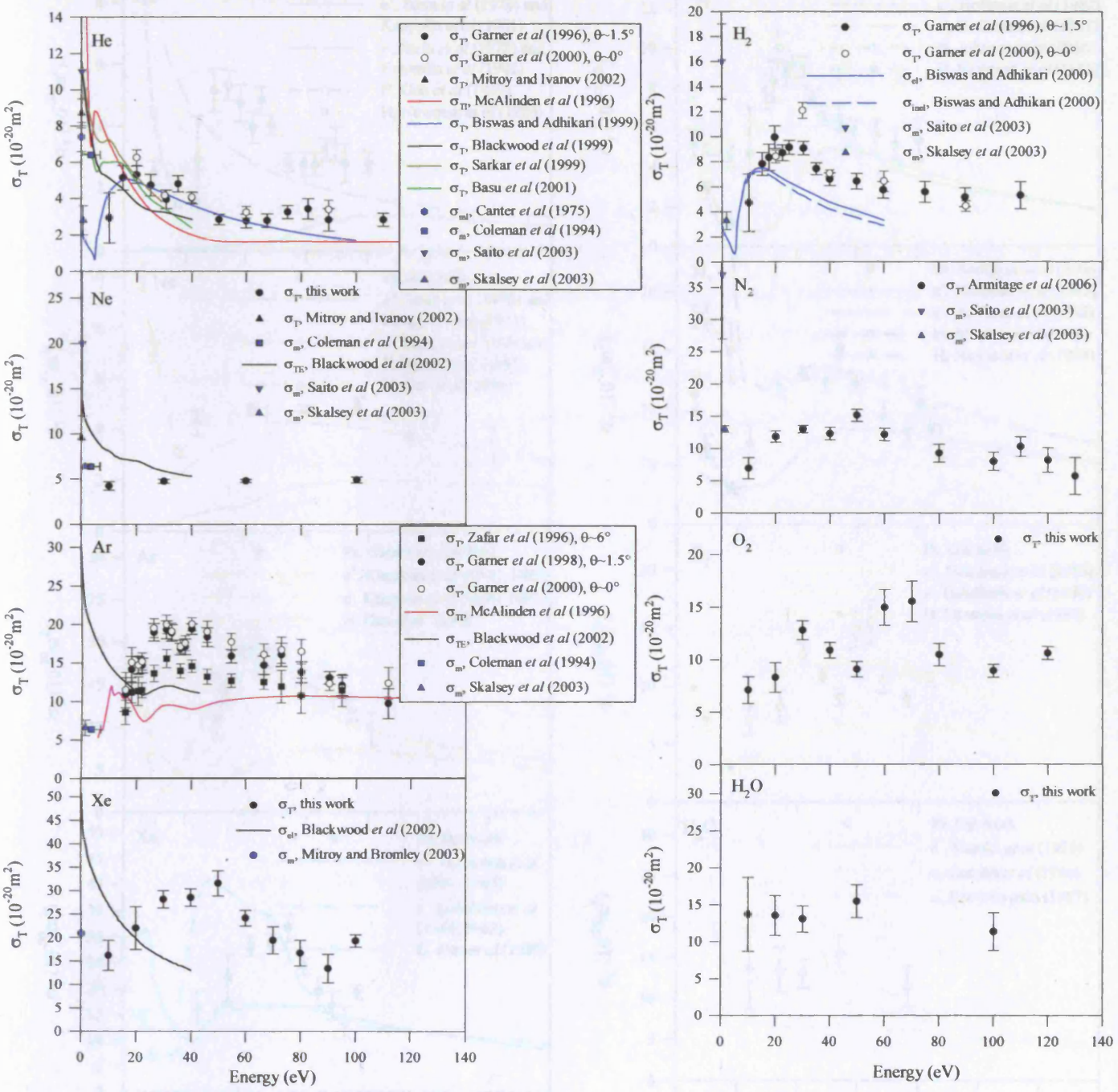

Figure 3.17: Summary of total cross-sections for Ps scattering from He, Ne, Ar, Xe, H_2, N_2, O_2 and H_2O compared with available theories and momentum transfer cross-sections.

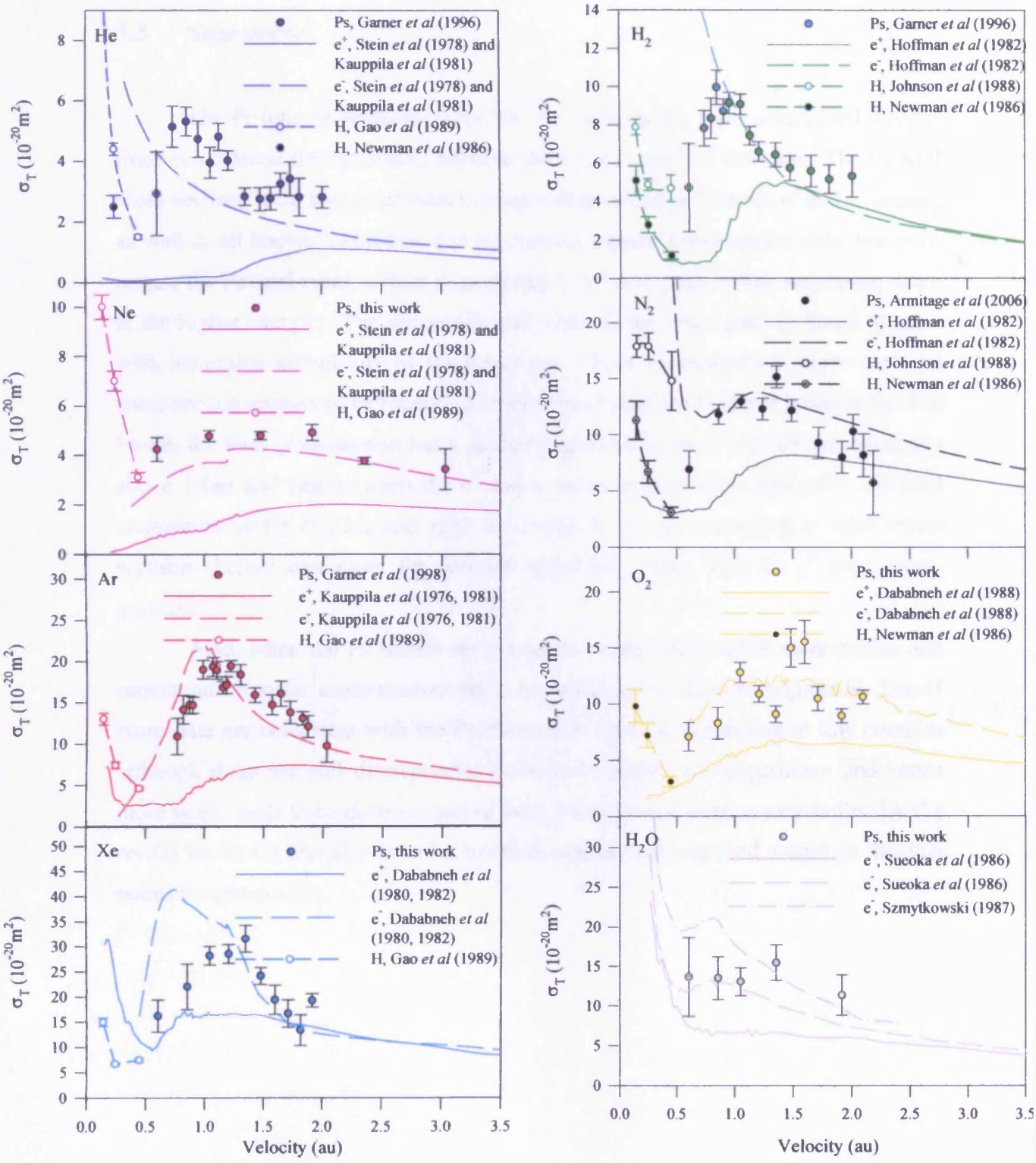

Figure 3.18: Total cross-sections for Ps scattering from He, Ne, Ar, Xe, H_2, N_2, O_2 and H_2O compared with those of other projectiles: H atom, e^+ and e^-.

3.5 Summary

The Ps total cross-sections for Ne, Xe, H_2O and O_2 were determined directly from coincidence measurements between the CEMA and NaI detectors. The Ps total cross-sections were compared with corresponding values by H atom, e^+ and e^- impact, as well as all known theoretical and momentum transfer cross-section data. For most targets the Ps total cross-section rises rapidly to a broad peak before decreasing again at the higher energies. The magnitude and width of the broad peak is found to grow with increasing complexity of the target gas. There are exceptions where the total cross-section appears to be roughly constant; this is seen for H_2O and possibly Ne. For Ps-Xe, the total cross-section has a similar magnitude to the e^--Xe total cross-section above 1.4au and lies between the e^+ and e^- cross-section below this value. Ps total cross-sections for O_2, Ne and H_2O are closer to the corresponding e^- total cross-sections (before correcting for forward scattering) rather than for e^+ total cross-sections.

Also, when the Ps results are compared to the integrated H atom results and momentum transfer cross-sections they are found to be alike in magnitude. The H atom data are consistent with the Ps theories in terms of decreasing at low energies although there are still discrepancies between Ps theory and experiment and hence more work needs to be done to resolve them. Further work is necessary to finalise the results for Ps-O_2 and also in order to check whether the observed scatter in the data points is reproducible.

Chapter 4: Projectile Fragmentation and Target Ionization Cross-Sections by Positronium Impact

4.1 Introduction

In section 1.6.3, ionization channels which can occur in positronium (Ps)-atom collisions were introduced. These include a target elastic process where the Ps atom is ionized (channel I), a singly inelastic process where the target atom is ionized (channel III), and a doubly inelastic process where both previous processes occur (channel V). The other two channels (II and IV) include the excitation of the target and Ps atom, respectively. It was predicted that target-elastic Ps ionization (channel I) would dominate scattering at intermediate energies (Biswas and Adhikari, 1999; and Blackwood *et al*, 1999).

This process was first observed in Ps-helium (He) collisions by Armitage *et al* (2002), using a time-of-flight technique, where the integrated cross-section and the longitudinal energy distributions of the residual positrons were measured for impact energies of 13, 18, 25, 33 and 60eV (see section 1.6.3).

A peak just below half the residual energy was observed in the differential cross-sections suggesting the occurrence of Electron Loss to the Continuum (ELC), whereby the residual positron (e^+) and electron (e^-) lie in a low relative-velocity Coulomb continuum state. A small shift from half of the residual energy was ascribed to the residual e^+ from Ps fragmentation being emitted within an angle of ~20° with respect to the beam axis.

As discussed in section 1.6.3, following the work of Armitage *et al* (2002), Sarkadi (2003) calculated the integrated cross-section and the longitudinal energy distributions of both the residual e^+ and e^-. He only took into account Ps elastic processes. Within his theory, an asymmetry was predicted between the energy distributions of the residual e^+ and e^- for 33eV impact energy, which has been investigated by Armitage *et al* (2007).

Using a retarding-field-analyser (RFA) method (Armitage *et al*, 2006), the Ps fragmentation study was extended to look at the residual e^+ and e^- at an impact energy of 30eV. At this energy, when looking at residual e^+ from Ps impact, channels I, II and

V can be detected, whereas when counting e^-, all five channels can be detected. The e^- from target ionization (channels III, IV and V) may be isolated by taking the difference between the integrated cross-sections for the residual particles. These cross-sections were found to agree within experimental uncertainties, implying that target ionization (channel III, IV and V) is negligible in this case (Armitage *et al*, 2006).

Using the same method as Armitage *et al* (2006), the fragmentation study has now been extended with the aim of ascertaining contributions from target ionization (channel II, IV and V) by Ps impact by looking at xenon (Xe). Integrated cross-sections of Ps in collision with Xe atoms at a Ps incident energy of 30eV and longitudinal energy distributions have been measured for both the residual e^+ and e^-. The processes for this target and impact energy are summarized in table 4.1 along with their corresponding residual energies. The NaI-CEMA coincidence detection system was used for the e^+ measurements, whereas for the e^- measurements, single CEMA counts were used, due to the absence of a correlated gamma-ray signal causing these data to be much more sensitive to background levels.

Table 4.1: The residual energies for the three main ionization processes available for Ps-Xe impact at 30eV.

Channel	Process	Residual Energy (eV)
I	$Ps + A \rightarrow e^- + e^+ + A$	23.20
III	$Ps + A \rightarrow Ps + A^+ + e^-$	17.87
V	$Ps + A \rightarrow e^- + e^+ + A^+ + e^-$	11.07

4.2 Scattering Cell for Fragmentation and Target Ionization Studies

A new scattering cell (shown in figure 4.1 as a cross-sectional schematic diagram) has been designed to aid the measurements of residual e^- from Ps fragmentation and target ionization. This new scattering cell was biased in order to accelerate the residual e^- from Ps fragmentation and target ionization out of the cell imparting them a longitudinal energy that separated them from any background e^-. The cell was designed so that the incident Ps beam entered the cell without

intercepting the entrance aperture and e^- released from Ps fragmenting on the exit aperture could not escape out of the cell.

The cylindrical body made of aluminium (Al) was biased at a potential of ±140V. An outer PTFE case provided electrical insulation and another Al cylinder was grounded through the chamber to stop any stray electric fields.

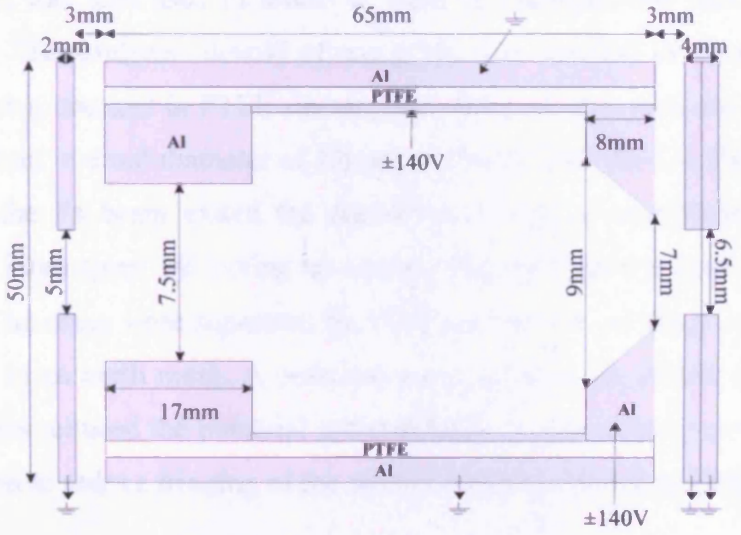

Figure 4.1: Schematic of the scattering cell for Ps fragmentation studies (not to scale).

The entrance aperture consisted of an Al disc also grounded through the chamber with a 5mm diameter hole and an Al cylinder (17mm long) held at ±140V with a 7.5mm diameter hole. The entrance aperture allowed the incident Ps beam to enter the cell without intercepting the aperture and fragmenting, as the exit aperture on the production cell was 1mm smaller in diameter and at a distance of 43.5mm (see figure 4.10). The exit aperture consisted of an Al cylinder (also held at ±140V) with a conical shaped hole and two discs with a mesh in-between, held at ground. This was to allow all the e^+/e^- from Ps fragmentation on the target gas and from target ionization, to get out of the cell, as well as stop any e^- released from Ps fragmenting on the aperture from exiting the cell (see appendix B for details). Both the entrance earth disc and exit earth discs were connected by screws to the Al cylinder held at ground and helped to decrease ExB fringing effects from the applied potential (see figure 4.2). The Ps pencil angle for this new cell was 1.26mSr and the effective length for this scattering cell was (55.2±0.36)mm calculated by measuring e^+ total cross-sections for Xe (see section 3.3.1 for details on measuring the effective length of the scattering cell).

An electrostatic arrangement to repel fast e^- from the source region was placed before the production cell to help minimize the flux of secondary e^- through the cell. The repeller consisted of an earth grid, a negatively biased tube and an earth aperture (see figure 4.3) encased in an earth mesh.

To minimize further the background for the e^- measurements, a retarding field analyzer (RFA) was also used to reflect e^+ from Ps fragmentation which exited the scattering cell. The analyzer, devoid of any grids, was attached to the cell by three pieces of studding encased in PTFE sleeving for electrical insulation and consisted of nine discs with an internal diameter of 22mm, as shown in figure 4.4. Care was taken to make sure the Ps beam exited the scattering cell and passed through the RFA without being intercepted by having an internal diameter greater than the Ps beam pencil angle. The discs were separated by PTFE spacers for electrical insulation and were enclosed in an earth mesh. A potential was applied to the central disc and four resistors in series reduced the potential symmetrically in even steps to ground at either end. This helped to reduce fringing of the electric fields and therefore ExB effects.

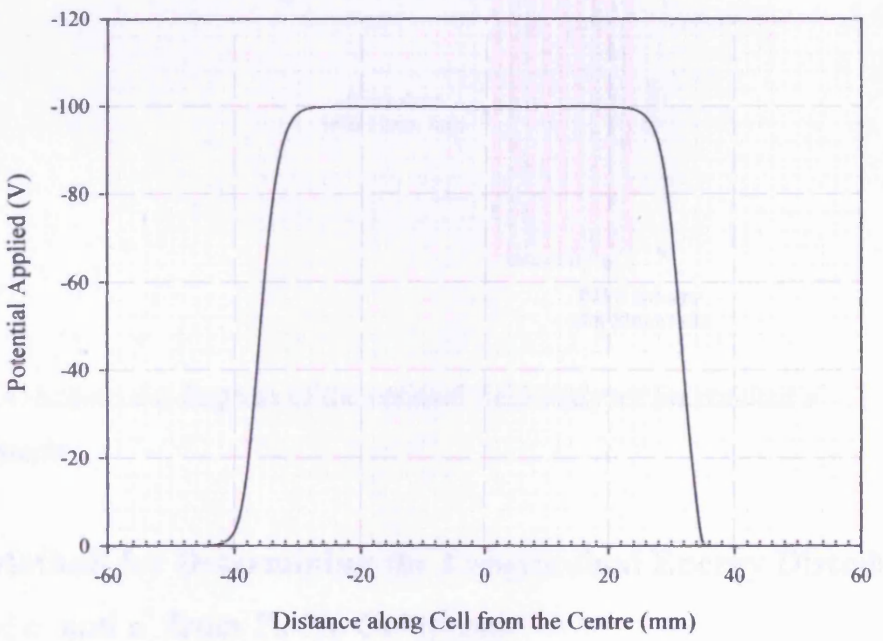

Figure 4.2: Plot of the variation of an applied potential (-100V) with respect to the distance along the cell body.

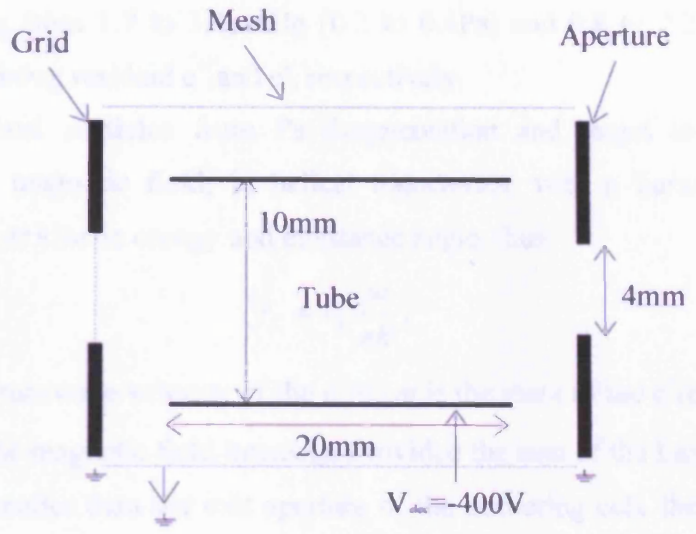

Figure 4.3: Schematic diagram of the e^- repeller.

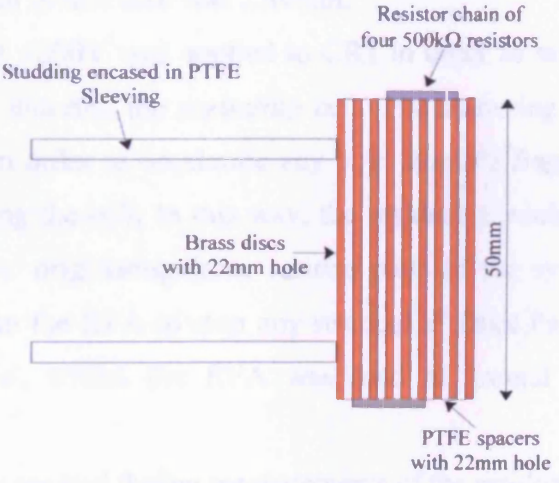

Figure 4.4: Schematic diagram of the residual field analyzer for residual e^- measurements

4.3 Method for Determining the Longitudinal Energy Distributions of e^- and e^+ from Ps-Xe Collisions

Molecular hydrogen (H_2) at a pressure of 10μmHg (1.3Pa) has been used to produce Ps in the production cell. The incident Ps entered the scattering cell where it could fragment on and/or ionize the target gas which, in this work, was Xe at

pressures ranging from 1.7 to 3.4μmHg (0.2 to 0.4Pa) and 0.8 to 2.2μmHg (0.1 to 0.3Pa) when detecting residual e^+ and e^-, respectively.

The residual particles from Ps fragmentation and target ionization were confined by the magnetic field, in helical trajectories, with a Larmor radius, r_L, determined by their kinetic energy and emittance angle, thus:

$$r_L = v_\perp \frac{m}{eB}, \tag{4.1}$$

where $v_\perp$ is the transverse velocity of the e^+/e^-, m is the mass of the e^+/e^-, e is the e^+/e^- charge and B is the magnetic field intensity. Provided the sum of the Larmor and beam (2mm) radii is smaller than the exit aperture of the scattering cell, the e^+/e^- from Ps fragmentation and target ionization can exit the cell (Armitage *et al*, 2002). Therefore a magnetic field of 22mT was used for 30eV impact energy to ensure all e^+/e^- from Ps fragmentation and target ionization were extracted from the cell. The sum of the Larmor and beam radii in this case was 2.84mm.

A potential of +200V was applied to CR1 in order to stop any e^+ exiting the production cell from entering the scattering cell. The scattering cell was biased at a potential of ±140V in order to accelerate any e^+/e^- from Ps fragmentation and target ionization upon exiting the cell. In this way, the residual e^- could be easily separated from the secondary e^- originating from various parts of the system. A potential of +250V was applied to the RFA to stop any residual e^+ from Ps fragmentation when measuring residual e^-, whilst the RFA was held at ground for the residual e^+ measurements.

The potentials applied during measurements of the residual e^+ and e^- are shown in figure 4.5 and 4.6, respectively. The e^+ data were obtained using a PC-based multi-channel analyzer (MCA), which recorded coincidences between the NaI detector and CEMA (see section 2.7.1).

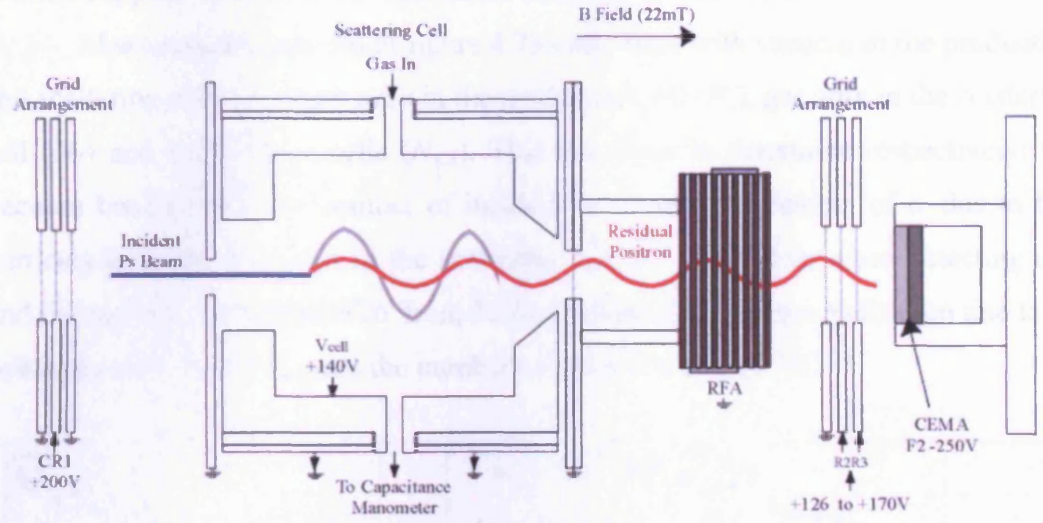

Figure 4.5: Schematic diagram showing the potentials applied during measurements of the residual e^+.

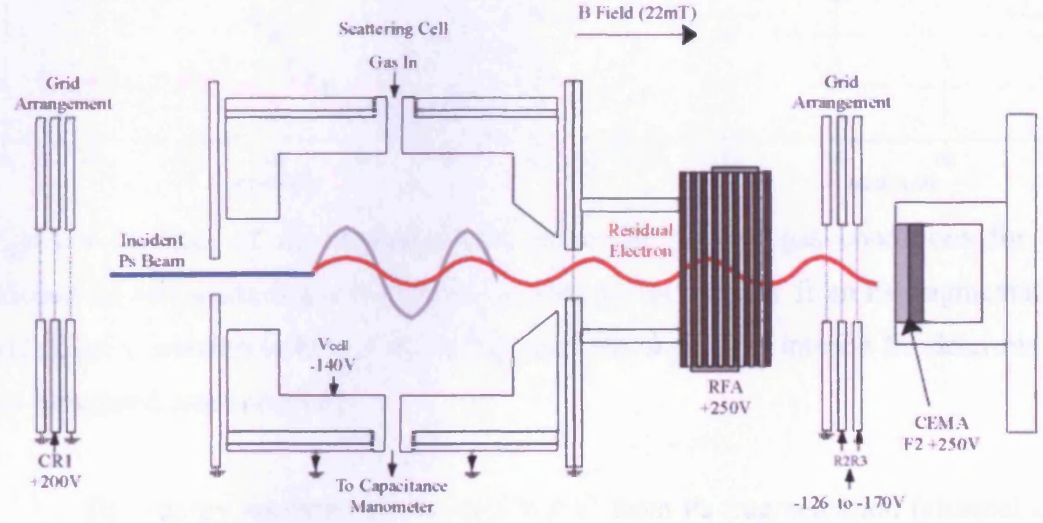

Figure 4.6: Schematic diagram showing the potentials applied during measurements of the residual e^-.

The e^- data were obtained using a PC-based multi-channel scalar (MCS), which recorded only the single counts from CEMA due to the absence of a correlated gamma-ray signal. This resulted in a worse signal-to-background ratio than for the e^+. All measurements were conducted through the use of a program designed using LabVIEW.

In order to measure the number of e^+/e^- from Ps fragmentation and target ionization and to determine their longitudinal energy spread, a positive/negative

potential applied to R2 and R3 was varied in 2V steps from ±(126-170)V.

Measurements (shown in figure 4.7) were made with vacuum in the production and scattering cells (N_V), gas only in the production cell (N_1), gas only in the scattering cell (N_2) and gas in both cells ($N_{1,2}$). This was done to determine respectively: the vacuum background; the number of incident Ps atoms; the number of e^- due to fast particles ionizing the target in the scattering cell (not a problem when detecting e^+); and the number of residual e^+/e^- from Ps fragmentation and target ionization due to Ps collisions with Xe atoms plus the number of transmitted Ps atoms.

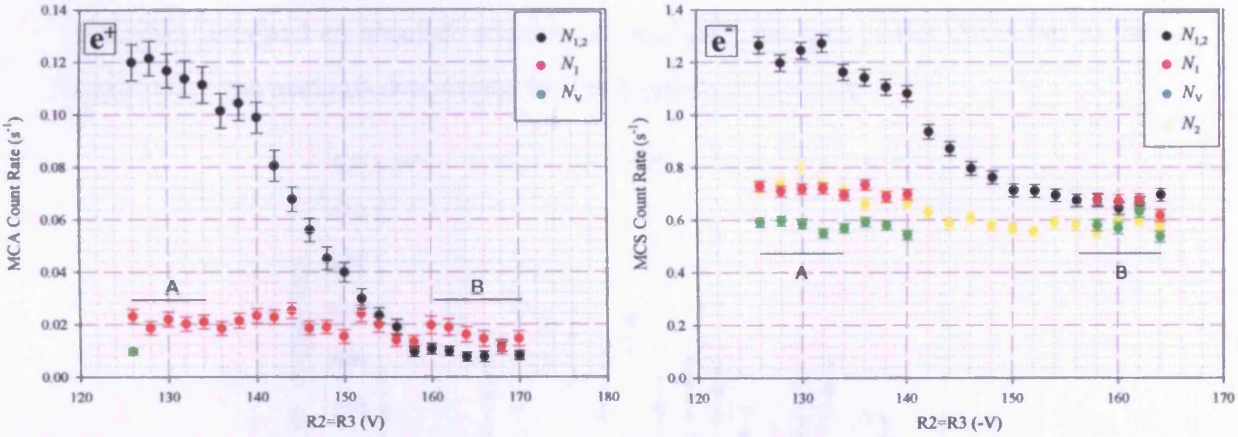

Figure 4.7: Plots of the measurements under the various gas conditions for the production and scattering cells used to find the number of e^+/e^- from Ps fragmentation and target ionization (where A and B represent the regions of interest for determining the integrated cross-section).

The energy spectrum for the residual e^+ from Ps fragmentation (channel I, II and V) could then be found as follows:

$$\left(\frac{dN_+\left(E_{//}^+\right)}{dE_{//}^+}\right)=\left(\frac{dN_{1,2}\left(E_{//}^+\right)}{dE_{//}^+}\right)-\left(\frac{dN_V\left(E_{//}^+\right)}{dE_{//}^+}\right), \tag{4.2}$$

where N_+ is the number of detected residual e^+ from Ps fragmentation due to collisions with Xe atoms, and $E_{//}^+$ is the residual e^+ longitudinal energy (i.e. $E_{//}^+ = eV_{R2/R3} - eV_{cell}$). In the case of the residual e^-, the energy spectrum (channels I – V) was found according to:

$$\left(\frac{dN_-\left(E_{//}^-\right)}{dE_{//}^-}\right)=\left(\frac{dN_{1,2}\left(E_{//}^-\right)}{dE_{//}^-}\right)-\left(\frac{dN_2\left(E_{//}^-\right)}{dE_{//}^-}\right), \tag{4.3}$$

where N_- is the number of detected residual e^- from Ps fragmentation and target ionization due to collisions with Xe atoms and $E_{//}^-$ is the residual e^- longitudinal energy (i.e. $E_{//}^- = eV_{R2/R3} - eV_{cell}$).

As the detection probability of the low energy e^+ and e^- could be hindered by scattering within the scattering cell, the possible attenutation of e^+/e^- with energy $E_{//}^{\pm}$ was computed. This was obtained by first differentiating the measurements made with gas in the scattering cell after subtracting the background according to equations 4.2 and 4.3. The results shown in figure 4.8 and 4.9 for the residual e^+ and e^-, respectively, were then assigned an absolute scale by normalizing the area under the curve to the integrated cross-sections determined as discussed in section 4.4.

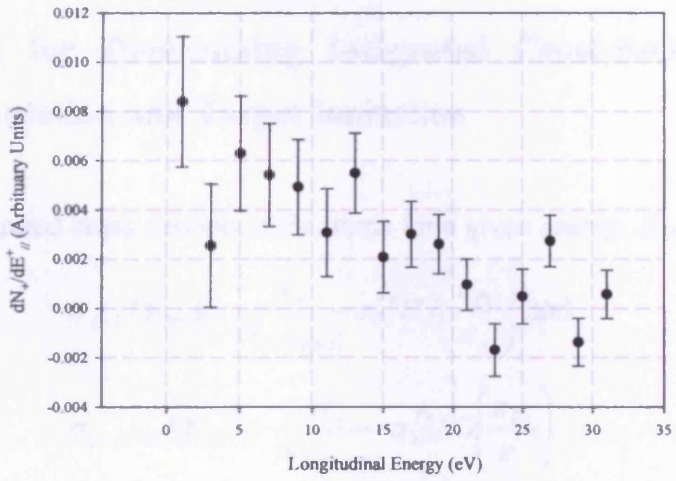

Figure 4.8: Longitudinal energy distribution for the residual e^+ from Ps fragmenting on Xe atoms (arbitrary scale).

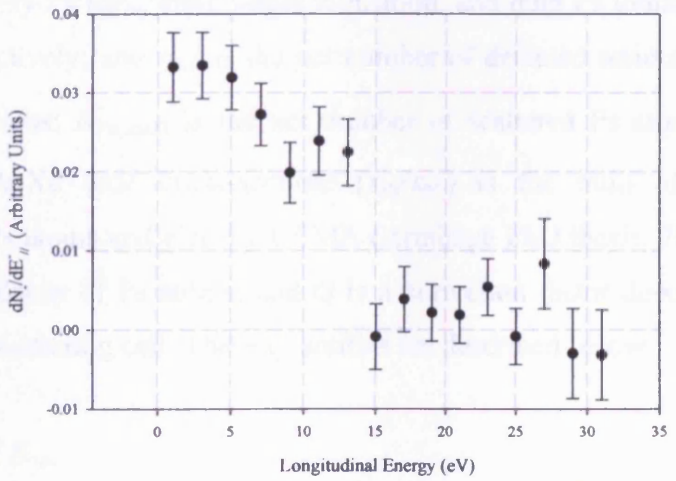

Figure 4.9: Longitudinal energy distribution for the residual e^- from Ps fragmenting on Xe atoms (arbitrary scale).

These distributions were then corrected for the possible attenuation of e^+/e^- of a given total energy E, assuming that $(E^{\pm})_{//} = E$, within the scattering cell according to:

$$\frac{I(E)}{I_0(E)} = \exp\left(-\frac{P}{kT} l_{½} \sigma_T^{+/-}(E)\right), \tag{4.4}$$

where P is the pressure of the target gas, $l_{½}$ is half the effective cell length (taken to approximate the average path length for the residual particles), I is the number of e^+/e^- detected, I_0 is the actual number of e^+/e^- from Ps fragmentation and target ionization, k is the Boltzmann constant, T is the ambient temperature, and $\sigma_T^{+/-}$ is the e^+/e^- total cross-section (Dababneh *et al*, 1980, 1982).

4.4 Method for Determining Integrated Cross-Sections for Ps Fragmentation and Target Ionization

The integrated cross-section of Ps atoms for a given energy, E_{Ps}, is given by:

$$\sigma_{I+V}(E_{Ps}) = \frac{N_+}{N_{Ps(scatt)}} \sigma_T^{Ps} SG\left(\frac{\varepsilon_{Ps}}{\varepsilon_+}\right) \text{ and} \tag{4.5}$$

$$\sigma_{I+III+V}(E_{Ps}) = \frac{N_-}{N_{Ps(scatt)}} \sigma_T^{Ps} SG\left(\frac{\varepsilon_{Ps}}{\varepsilon_-}\right), \tag{4.6}$$

where the subscripts (I, III and V) represent the channels as defined by reactions (1.16-1.20), namely Ps ionization, target ionization, and both Ps ionization and target ionization, respectively; and $N_{+/-}$ is the net number of detected residual e^+/e^- from Ps impact on Xe atoms; $N_{Ps(scatt)}$ is the net number of scattered Ps atoms; σ_T^{Ps} is the corresponding Ps-Xe total cross-section; $(\varepsilon_{Ps}/\varepsilon_{+/-})$ is the ratio of the detection efficiencies for Ps atoms and e^+/e^- by CEMA (Armitage PhD thesis, 2002); S corrects for the in-flight decay of Ps atoms; and G is a correction factor dependent upon the geometry of the scattering cell. These quantities are described below.

Determination of $N_{+/-}$:

The number of e^+/e^- from Ps fragmentation and target ionization were determined in energy steps of 2eV. The net flux of e^+ from Ps fragmentation for a

given voltage, $N^{+}_{net}(V)$, was obtained by subtracting N_V(V) from $N_{1,2}$(V) for the flat region (A in figure 4.7) i.e.:

$$N^{+}_{net}(V) = N_{1,2}(V) - N_V(V), \tag{4.7}$$

The net flux of e^- from Ps fragmentation and target ionization for a given voltage, $N^{-}_{net}(V)$, was obtained by subtracting N_2(V) from $N_{1,2}$(V) for the flat region (shown as A in figure 4.7) i.e.:

$$N^{-}_{net}(V) = N_{1,2}(V) - N_2(V), \tag{4.8}$$

Thus, the number of e^+/e^- from Ps fragmentation and target ionization, $N_{+/-}$, was obtained from the weighted mean of $N^{\pm}_{net}$ at each value of V over the energy range shown as A in figure 4.7, i.e.:

$$N_{+/-} = \left\langle N^{\pm}_{net}(V) \right\rangle_A, \tag{4.9}$$

where < > represents the weighted mean.

Determination of $N_{Ps(scatt)}$:

The difference between the signal measured with ($N_{1,2}$) and without (N_1) gas in the scattering cell gives the number of Ps atoms scattered from the target gas, $N_{Ps(scatt)}$. For the e^+ and e^- data, this number was found for high values of V_{R2} where the data were flat, shown in figure 4.7 as region B. Thus, the number of Ps atoms scattered by the gas in the scattering cell was:

$$N_{Ps(scatt)} = \left\langle N_1(V) - N_{1,2}(V) \right\rangle_B, \tag{4.10}$$

where < > represents the weighted mean.

The number of scattered Ps atoms from the residual e^- spectra was computed from the attenuation of the incident Ps beam (N_1-N_V) i.e.:

$$N_{Ps(scatt)} = (N_1 - N_V)\left(1 - \exp\left(-\frac{Pl\sigma_T^{Ps}}{kT}\right)\right), \tag{4.11}$$

where P is the target gas pressure, l is the effective length of the scattering cell, k is the Boltzmann constant, T is the ambient temperature and σ_T^{Ps} is the Ps total cross-section determined as described in section 3.2.

Determination of the Survival Factor, S:

As Ps has a finite lifetime, there are more Ps atoms available to fragment within the scattering cell than are detected at CEMA. This is accounted for by using the survival factor, S, which is defined as the ratio of the probability that the incident Ps beam survives to be detected at CEMA to that of being available to fragment within the scattering cell, i.e.:

$$S = \frac{S(CEMA)}{\langle S(ScatteringCell)\rangle}, \tag{4.12}$$

where $S(CEMA)$ is the fraction of Ps atoms with energy, E_{Ps}, which survive to be detected at a given flight length, L, and is given by:

$$S(CEMA) = \exp\left(\frac{-1}{\tau} L\sqrt{\frac{m}{eE_{Ps}}}\right), \tag{4.13}$$

where τ is the ortho-Ps lifetime of 142ns, m is the e^+/e^- mass and L=(0.58±0.01)m for this study (see figure 4.10 for definition). The average value for the fraction of Ps atoms which survive and may fragment within the scattering cell, $\langle S(ScatteringCell)\rangle$ is:

$$\langle S(ScatteringCell)\rangle = \frac{1}{(l_2 - l_1)}\int_{l_1}^{l_2} \exp\left(\frac{-1}{\tau} x\sqrt{\frac{m}{eE_{Ps}}}\right) dx, \tag{4.14}$$

where x is the Ps flight length. l_1=(0.07±0.01)m and l_2=(0.12±0.01)m are defined in figure 4.10 and represent the upper and lower limits of the Ps flight length through the scattering cell. These correspond to the flight length from the centre of the production cell to the centre of the scattering cell, plus or minus half the effective length for this scattering cell (see section 4.2). In this way, at a Ps energy of 30eV, S= 0.22±0.04 and this value has been used in equations 4.5 and 4.6.

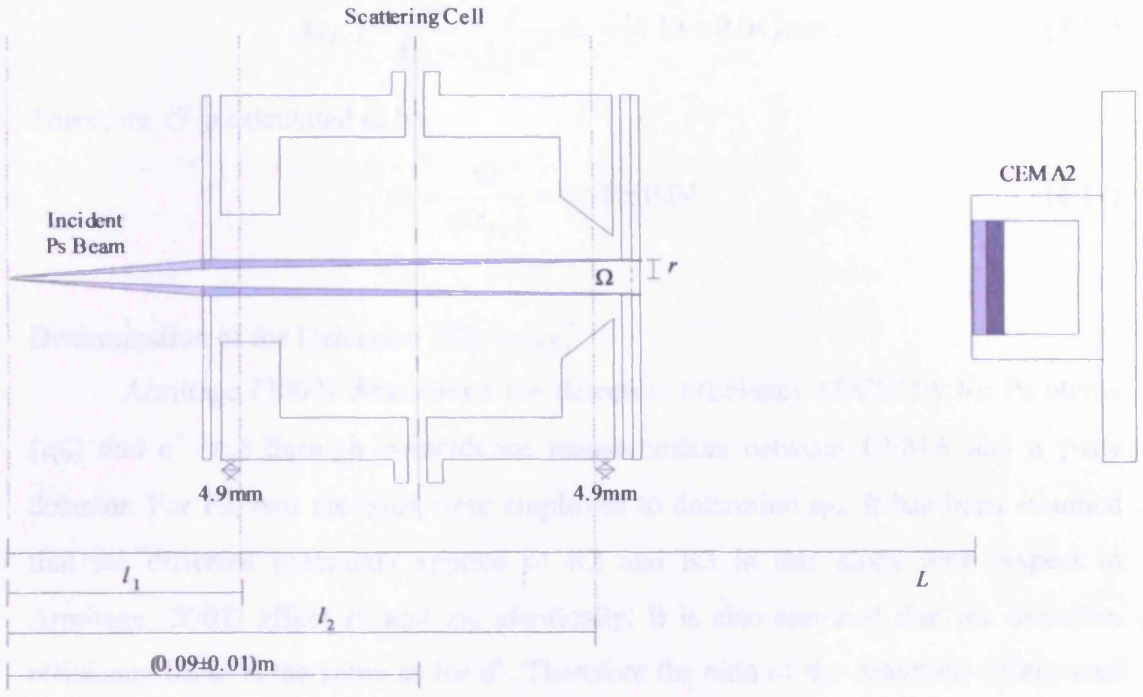

Figure 4.10: Geometry of the scattering cell (not to scale). The grey/purple region represents Ps outside the detection solid angle.

Determination of the Geometric Factor, *G*:

The Ps detection solid angle, Ω, indicated in figure 4.10, is defined by the radius of the exit aperture of the scattering cell earth disc (r) and the flight length to the end of the scattering cell (l_2) such that:

$$\Omega = \frac{\pi r^2}{(l_2)^2} = (2.38 \pm 0.62) msr \,. \tag{4.15}$$

Only Ps atoms within this angle will be detected at CEMA.

As discussed in Armitage *et al* (2002), Ps atoms may enter the scattering cell outside the Ps detection solid angle (the grey/purple region in figure 4.10) and upon fragmenting give rise to a e^+ and e^-, which are then magnetically confined and detected at CEMA. This will lead to a greater fragmentation signal than that possible from the detectable Ps. To correct for this effect, a geometric factor was introduced, this is given by the ratio of the Ps detection solid angle to the average solid angle of the Ps beam along the cell, $\langle \Omega_{Ps} \rangle$, obtained by integrating over the length of the scattering cell, i.e.:

$$\langle \Omega_{Ps} \rangle = \frac{\pi r^2}{(l_2 - l_1)} \int_{l_1}^{l_2} \frac{1}{x^2} dx = (4.13 \pm 0.04) msr . \quad (4.16)$$

Therefore, G is calculated to be:

$$G = \frac{\Omega}{\langle \Omega_{Ps} \rangle} = 0.58 \pm 0.04 . \quad (4.17)$$

Determination of the Detection Efficiency:

Armitage (2002) determined the detection efficiency of CEMA for Ps atoms (ε_{Ps}) and e^+ (ε_+) through coincidence measurements between CEMA and a γ-ray detector. For Ps, two methods were employed to determine ε_{Ps}. It has been assumed that the different potentials applied to R2 and R3 in this study with respect to Armitage (2002) affect ε_+ and ε_{Ps} identically. It is also assumed that the detection efficiency for e^- is the same as for e^+. Therefore the ratio of the detection efficiencies for Ps atoms and e^+/e^- by CEMA, ($\varepsilon_{Ps}/\varepsilon_{+/-}$), is 0.33±0.01 for a Ps energy of 30eV.

The integrated cross-section, calculated using equations 4.5 and 4.6, was used to convert $\frac{dN_{+/-}}{dE}$ to absolute differential cross-sections $\frac{d\sigma_{+/-}}{dE}$, as mentioned in section 4.3. These were then corrected for possible attenuation of the residual particles within the scattering cell as per equation 4.4 (assuming the longitudinal energy to be equal to the total energy of the ejected e^+/e^-) and finally the area under the corrected absolute differential cross-sections was used to compute the final integrated cross-section, according to:

$$\sigma_{I+V}(Ps) = \int_0^E \frac{d\sigma_+(E)}{dE} dE \text{ and} \quad (4.18)$$

$$\sigma_{I+III+V}(Ps) = \int_0^E \frac{d\sigma(E)}{dE} dE . \quad (4.19)$$

4.5 Results and Comparison with Theory

4.5.1 Longitudinal Energy Distributions

The longitudinal energy distributions for the residual particles from Ps, fragmenting on Xe atoms at an impact energy of 30eV, have been measured. As discussed within section 4.3, these distributions were also corrected for possible attenuation of the residual particles within the scattering cell. Figure 4.11 shows the results for the residual e^+ before and after this correction indicating a correction factor in the range of 1.1 and 1.6. The true longitudinal energy distribution for the residual e^+ would be somewhere between the corrected and uncorrected data. The longitudinal energy distribution before correction, shown in figure 4.11, agrees fairly well with the theoretical data of Starrett *et al* (2005), although the errors on the experimental results are rather large. The theoretical results were determined using an impulse approximation for target elastic collisions only. There is a peak at just below half the residual energy, $E_r/2$, ($E_r/2 = 11.6eV$, where $E_r = E_{Ps} - 6.8eV$) before decreasing towards zero at E_r~21eV. After correction, the experimental data might indicate an extra contribution from the doubly inelastic process but in this case the systematic uncertainties are significant.

Figure 4.12 shows the results for the residual e^- before and after correction for attenuation in the scattering cell, along with the impulse approximation data of Starrett *et al* (2005). The longitudinal energy distribution after correction is approximately a factor of 1.0 to 1.5 higher than before correction for the lowest residual e^- energies (below 15eV). As for the residual e^+, the true longitudinal energy distribution would be somewhere between the corrected and uncorrected data. At 1eV, there is virtually no attenuation as the e^- total cross-section (Dababneh *et al*, 1980) is close to the Ramsauer-Townsend minimum (see section 1.5).

At energies greater than 15eV, the longitudinal energy distribution for the residual e^- agrees within errors with the Starrett *et al* (2005) data. Below 15eV, before and after correction, it is considerably higher than Starrett *et al* (2005). This might be due to target ionization (channel III, IV and V), as low energy e^- are predicted to dominate the target ionization spectrum. The experimental results decrease rapidly towards zero at just above half the residual energy ($E_r/2 = 11.6eV$).

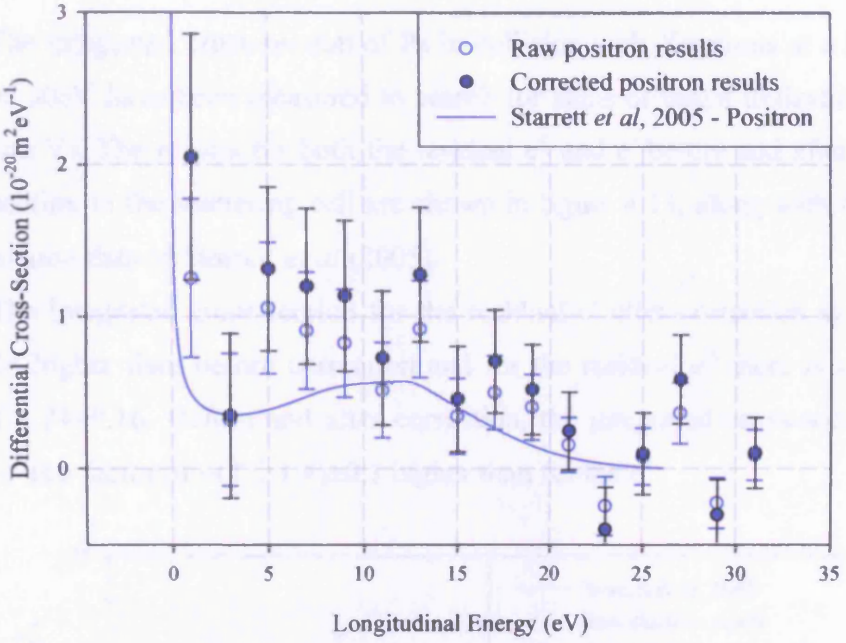

Figure 4.11: Longitudinal energy distribution for the residual e^+ from Ps fragmenting on Xe atoms compared with theory.

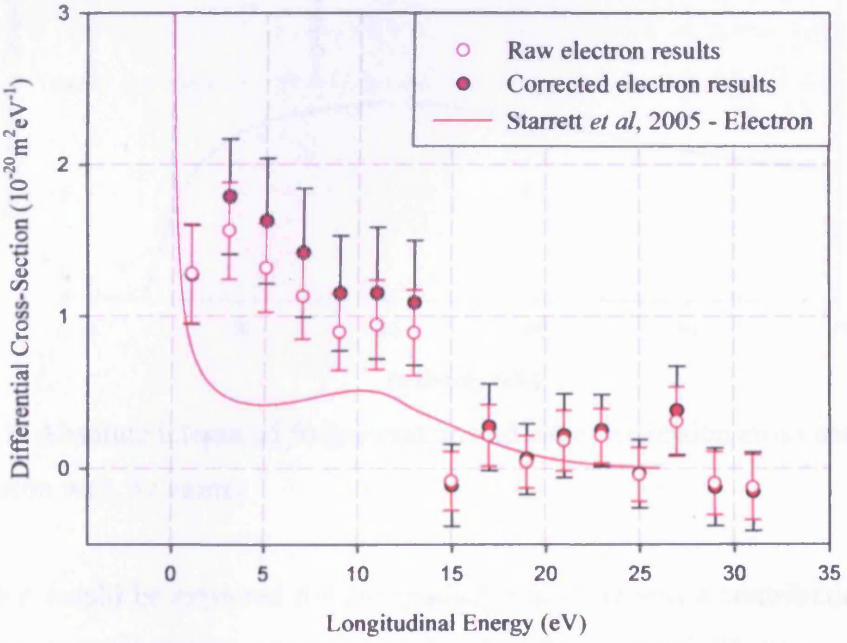

Figure 4.12: Longitudinal energy distribution for the residual e^- from Ps fragmenting on Xe atoms and possible target ionization compared with theory.

4.5.2 Integrated Cross-Section

The integrated cross-section of Ps in collision with Xe atoms at a Ps incident energy of 30eV have been measured to search for signs of target ionization (channel III, IV and V). The results for both the residual e^+ and e^- before and after correction for attenuation in the scattering cell are shown in figure 4.13, along with the impulse approximation data of Starrett *et al* (2005).

The integrated cross-section for the residual e^- after correction is a factor of 1.15±0.14 higher than before correction and for the residual e^+ there is a correction factor of 1.24±0.16. Before and after correction, the integrated cross-section for the residual e^- is a factor of ~(1.5/1.4)±0.1 higher than for the e^+.

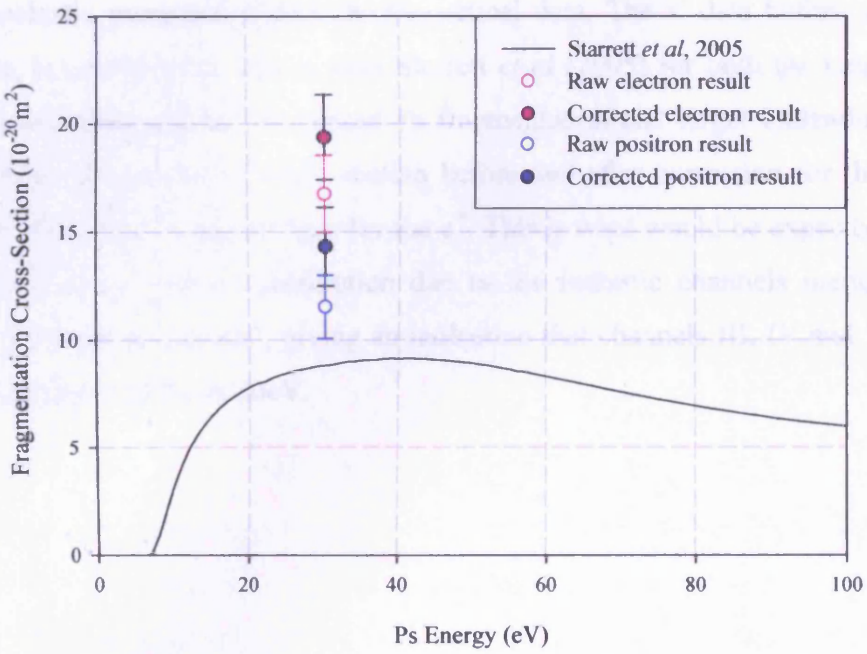

Figure 4.13: Absolute integrated fragmentation and target ionization cross-section for Ps in collision with Xe atoms.

This is what would be expected for the residual e^- if there was a contribution due to the inelastic channels mentioned in section 4.1 (target ionization). There appears to be a discrepancy between the experimental data for the uncorrected and corrected e^+ and the theoretical data of Starrett *et al* (2005), suggesting a possible over correction due to statistical uncertainties. This could also be due to the theory only looking at target

elastic collisions and partly due to the rather large errors in the longitudinal energy distribution. For completeness Starrett *et al* (2005) would need to take into account inelastic processes.

4.6 Summary

The Integrated cross-section of Ps in collision with Xe atoms at a Ps incident energy of 30eV and the longitudinal energy distributions have been measured for both the residual e^+ and e^-. The possible attenuation of the residual particles within the scattering cell was also considered. The e^+ experimental data agrees fairly well with the impulse approximation of Starrett *et al* (2005) for the longitudinal energy distribution but not for the integrated cross-section. This could be partly due to the rather large errors in the longitudinal energy distribution and implies that they need to include inelastic processes within the theoretical data. The e^- data before and after correction, is considerably higher than Starrett *et al* (2005) for both the longitudinal energy distribution, and the integrated Ps fragmentation and target ionization cross-section. Also, the integrated cross-section before and after correction for the e^- is a factor of $\sim(1.5/1.4)\pm0.1$ higher than for the e^+. This is what would be expected for the residual e^- if there was a contribution due to the inelastic channels mentioned in section 4.1 (target ionization), giving an indication that channels III, IV and V play a part for Ps impact on Xe at 30eV.

Chapter 5: Doubly Differential Ionization Cross-Sections for Positrons in Collision with Water Molecules

5.1 Introduction and Motivation

Water (H_2O) is an important polyatomic molecule, as it makes up the bulk of living organisms and provides the medium for a host of chemical reactions. Its vapour has been observed in the atmosphere of the Sun and of several planets both within and outside the Solar System (Wallace *et al*, 1995; and Tinetti *et al*, 2007) and within the Earth's atmosphere, H_2O is a key greenhouse gas (Taylor, 2002).

H_2O molecules may be ionized by positron (e^+) impact through direct ionization, electron (e^-) capture or annihilation and it is therefore important to understand these interactions. However, there is a lack of data for e^+ impact with H_2O and these are confined to total cross-section measurements, as discussed in chapter 3 and the measurements performed by Arcidiacono (PhD thesis, 2006). Arcidiacono (2006) obtained preliminary values for the total single ionization cross-section, σ_t^+, the direct single ionization cross-section, σ_i^+, and the positronium (Ps) formation cross-section, σ_{Ps}, for impact energies from 4 to 1000eV. The total single ionization cross-section is given by:

$$\sigma_t^+ = \sigma_i^+ + \sigma_{Ps} + \sum HO, \tag{5.1}$$

where HO represents the higher order cross-sections. It was found that the ionization probability for e^+ collisions is greater than that for e^- by up to a factor of two and that Ps formation makes an important contribution to the total ionization cross-section from threshold up to 40eV.

To complement this work, Arcidiacono (2006) commenced the measurements of the ejected e^- spectra. These types of studies are sensitive to correlation and interference effects. One such manifestation is a cusp, seen in doubly differential ionization by ion-impact, at a position which corresponds to the velocity of the e^- matching that of the ion. This is referred to as the Electron Capture to the Continuum

(ECC) (e.g. Lucas and Harrison, 1972; Rødbro and Anderson, 1979; Schultz *et al*, 1991; and references therein) and has been discussed also in section 1.5.

For the case of ionization by e^+ impact, different theoretical determinations exist concerning the prominence of the ECC cusp structure in the doubly differential cross-section (DDCS) (Mandal *et al*, 1986; Brauner *et al*, 1989; Schultz and Reinhold, 1990; Bandyopadhyay *et al*, 1994; Sparrow and Olson, 1994; and Brauner and Briggs, 1991), and several measurements were performed at UCL (Moxom *et al*, 1992; Kövér *et al*, 1993, 1994, and 1998), which did not reveal the expected enhancement at around half the residual kinetic energy ($E_r/2=(E^+-I)/2$), where I is the ionization energy and E^+ is the e^+ incident energy (see figure 1.11 in section 1.5).

As mentioned in section 1.5, Kövér and Laricchia (1998) observed a small ECC cusp in a triply differential cross-section (TDCS) spectrum for 100eV e^+ impact with molecular hydrogen (H_2). This work was recently extended to 50eV impact energy (Kövér *et al*, 2001; Fiol *et al*, 2001; and Arcidiacono *et al*, 2005), where an unexpected energy share between the ejected e^- and the scattered e^+ after ionization was observed. The origin of this asymmetry is not fully understood but hypotheses include a strong post-collision interaction between the e^+/e^- and the recoiling ion target and/or competition from Ps formation, which is more important at lower energies (Walters, 2004). Interestingly, for 10 and 20keV proton impact energy, which corresponds to approximately the same velocity as in the e^+ study, the Belfast group observed a similar shift of the ECC peak (Shah *et al*, 2003), although Sarkadi and Barrachina (2005) believe this shift to be an artefact of the angular resolution of the experimental system.

In order to complete the work of Arcidiacono (2006) and complement the e^+ and Ps collision studies with H_2O as presented in chapter 3, the DDCS of H_2O molecules by 100 and 153eV e^+ impact have been measured in the forward direction (~0°). The branching ratios for OH^+/H_2O^+ and H^+/H_2O^+ have also been determined. As mentioned in section 3.4.4, H_2O has a large dipole moment (0.73au), which results in significant forward elastic and inelastic scattering effects (e.g. Jung *et al*, 1982; and Itikawa and Mason, 2005) for collisions with e^-. The presence of the long-range dipole interaction could therefore significantly influence the DDCS. The data were measured using an electrostatic e^+ beam.

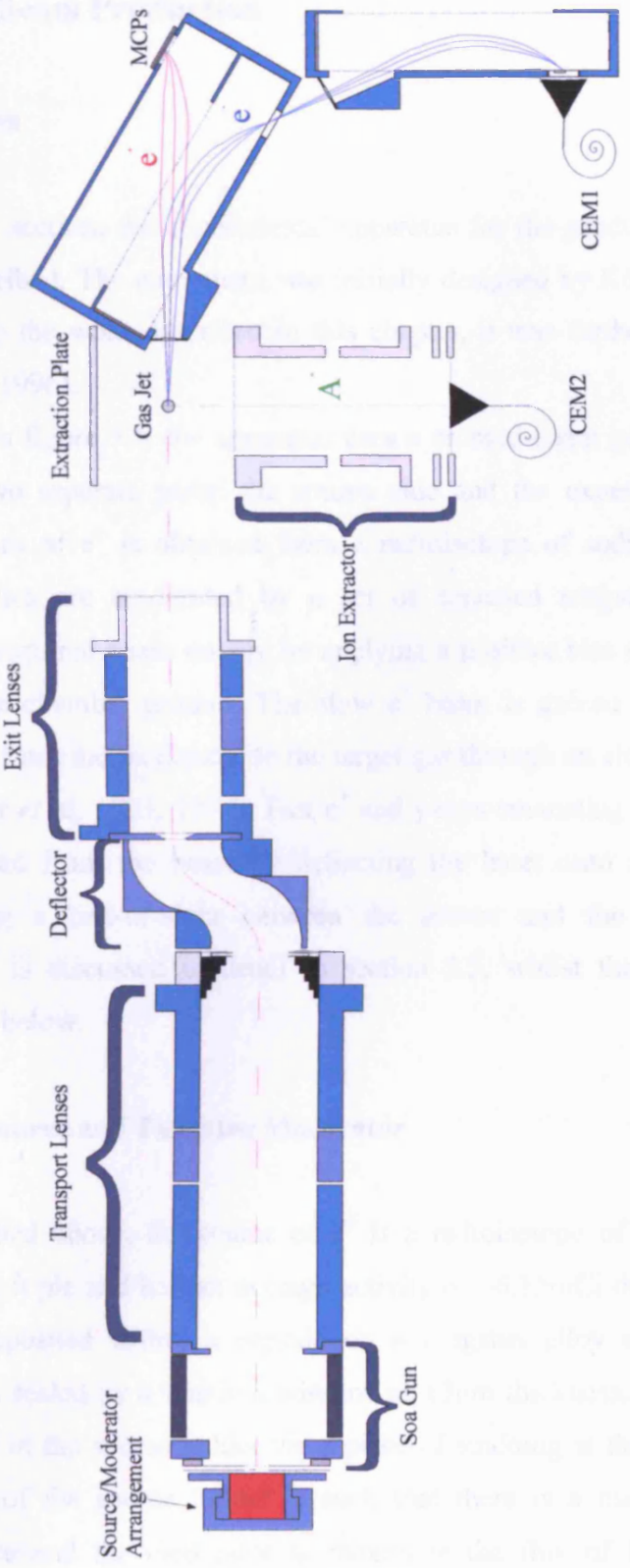

Figure 5.1: Schematic of the experimental arrangement.

Descriptions of the experimental methods used to obtain the results are included and the data are compared with theoretical calculations where possible.

5.2 Positron Beam Production

5.2.1 Introduction

Within this section, the experimental apparatus for the production of a slow beam of e^+ is described. The equipment was initially designed by Kövér *et al* (1993, 1994) and, prior to the work described in this chapter, it was further developed by Finch (PhD thesis, 1996).

As shown in figure 5.1, the apparatus uses a crossed-beam geometry and can be divided into two separate parts: the source side and the experimental side. A monoenergetic beam of e^+ is obtained from a radioisotope of sodium (^{22}Na). The resulting β^+ particles are moderated by a set of annealed tungsten meshes and accelerated to the required beam energy by applying a positive bias to the moderator with respect to the chamber ground. The slow e^+ beam is guided and focused by electrostatic fields from the moderator to the target gas through an electrostatic optics lens system (Kövér *et al*, 1993, 1994). Fast e^+ and γ-rays emanating from the source region are separated from the beam by deflecting the latter onto a different axis, thereby preventing a line-of-sight between the source and the detectors. The experimental side is discussed in detail in section 5.3, whilst the source side is discussed in detail below.

5.2.2 Positron Source and Tungsten Moderator

As mentioned above, the source of e^+ is a radioisotope of ^{22}Na. This was supplied by Du Pont plc and had an average activity of ~6.15mCi during this study. The isotope is deposited within a capsule on a tungsten alloy disc of 12.7mm diameter, which is sealed by a titanium window of 13μm thickness. The source and capsule are placed in the source holder via a piece of studding at the end of a brass plug. The design of the source holder is such that there is a minimum distance between the source and the moderator to maximize the flux of fast β^+ particles incident on the moderator. PTFE washers are used to provide electrical isolation between the source/moderator and the moderator/earth grid. Figure 5.2 shows the assembly for the source and tungsten moderator holder.

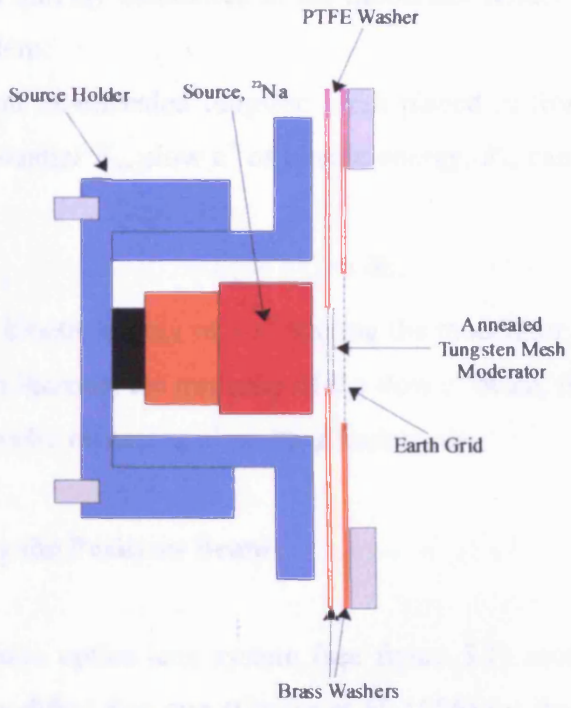

Figure 5.2: Schematic of the source and moderator arrangement.

For the electrostatic beam, a tungsten moderator is used to moderate the e^+. It consists of four superimposed layers of annealed 90% transmission tungsten mesh, each piece having an area of $15mm^2$. As shown in figure 5.2, the meshes are held in place by two brass washers with an internal diameter of 4mm. To ensure an optimum yield of slow e^+, an annealing process was performed. This is described in detail by Zafar *et al* (1988, and 1989) and Zafar (PhD thesis, 1990) and involves heating the meshes resistively in a tungsten foil oven in a vacuum of ~$5x10^{-2}$Torr (~7Pa) in order to relax their lattice structure and to remove any contaminants (i.e. absorbed oxygen (O_2) and H_2O) from the surface. Firstly, a constant low current is passed through the oven until the pressure in the chamber has risen (due to water evaporation from the meshes and oven) and returned to base level. The tungsten foil is then gradually heated to higher temperatures, resulting in a pressure increase as further contaminants are removed. This heating is carried out in 5s bursts to prevent contaminants within the electrode assembly from overheating, whilst also preventing electrical breakdown by ensuring the pressure in the chamber remains below $1x10^{-1}$Torr (13.3Pa). Annealing is empirically considered completed when the meshes can be heated quickly at a temperature of ~2000°C without a substantial pressure increase. On cooling, the tungsten re-crystallises with fewer defects, which would act as e^+ traps.

The meshes are then quickly assembled in the moderator holder in air and placed in the experimental system.

By earthing an un-annealed tungsten mesh placed in front of the moderator, which is held at a potential V_m, slow e^+ of kinetic energy, E_+, can be extracted, where E_+ is given by:

$$E_+ = eV_m + \delta E, \tag{5.2}$$

and δE is the initial kinetic energy of a e^+ leaving the moderator and is usually of the order of a few eV. To increase the intensity of the slow e^+ beam, the source was biased to ~9V above V_m, thereby reflecting e^+ emitted backwards.

5.2.3 Transporting the Positron Beam

The electrostatic optics lens system (see figure 5.1) used to transport the e^+ beam comprises a modified Soa gun (Canter *et al*, 1986) for the extraction of the e^+ beam and standard beam transport and deflection devices, including double and triple cylinder lenses (Harting and Read, 1976). These lenses are characterized by cylindrical symmetry. Kövér *et al* (1992) and Finch (1996) simulated the performance of the beam transport.

The double cylinder lens comprises two cylindrical electrodes held at two different voltages to focus and change the energy of the traversing e^+, whilst the triple cylinder lens changes the acceleration ratio of the e^+ without varying their image position. As mentioned above, a modified Soa Gun is used to focus the slow e^+ after they have been emitted from the moderator and accelerated by the grid. This is composed of three electrodes, where two of the lenses are held at the same voltage and a third lens is held at an independent voltage.

The transport lens, after the Soa Gun, consists of three cylindrical elements and works as an Einzel lens, as two of the elements are held at the ground potential of the chamber. This serves to produce a focusing effect without changing the beam energy. The potential applied to the mid-electrode is varied according to the energy of the beam and two apertures, located at each end of the transport lens, provide a reduction in the angular spread of the beam.

A double cylindrical condenser is used as the deflector to separate the slow e^+ beam from the fast β^+ particles and γ rays. It deflects the e^+ beam upwards by 20mm

before it continues to travel parallel to its original trajectory towards the interaction region under the influence of the applied negative potential.

Finally, an exit lens which consists of an aperture, an electrode (usually grounded) and a three element lens system is employed to provide a final focusing of the beam before it enters the interaction region. The diameter of the e^+ beam at the centre of the collision chamber is estimated to be less than 4mm.

5.2.4 Vacuum System

The lens system and interaction region are enclosed in a vacuum chamber, which is internally encased in mu-metal. The mu-metal gives an adequate shield from the Earths magnetic field, which is reduced to ~0.3μT throughout the system, except at the two connecting regions where it is 10μT. The two connecting regions lie between the Soa gun and the transport lens, and between the exit lens and the interaction region.

A high vacuum of ~$1x10^{-6}$Torr (0.1mPa) is maintained in the vacuum chamber through the use of an Edwards vapour diffusion pump (type 250/2000C), which evacuates the entire chamber via a 160mm diameter port. The diffusion pump is backed by an Edwards rotary pump (ED250).

A Pirani gauge situated between the diffusion pump and backing pump is used to monitor the backing line pressure, and both magnetic and manual isolation valves are placed between the two pumps, such that the backing pump may be isolated if required. If the level on the Pirani gauge rises above ~$1x10^{-1}$Torr (13.3Pa), then a system-protection device is triggered, which cuts the power to the diffusion pump and closes the magnetic valve, thereby helping to prevent backstreaming and isolating the system. This system protection device is also activated if the flow of H_2O for cooling the diffusion pump is interrupted.

5.3 Detection of Positrons and Ions

5.3.1 Introduction

Within this section, the experimental apparatus for the detection of e^+ and ions is described. It comprises a gas nozzle, an ion extractor, a tandem parallel plate analyzer (PPA), and detectors. The PPA allows either scattered e^+ or e^- which are ejected in the forward direction (~0°), following impact ionization, to be energy analyzed. A time-of-flight (T-o-F) technique has been used in order to achieve an enhanced signal-to-noise ratio (see section 1.6.3), to analyze the energy of the scattered e^+ and to carry out charge-to-mass analysis on the residual ions.

The measurements were obtained via coincidences between two detectors discussed below: two channel electron multipliers (CEM1 and CEM2), one situated at the end of the second part of the PPA and the other at the end of the ion extractor.

5.3.2 Tandem Parallel Plate Analyzer

A schematic of the PPA is shown in figure 5.3. This was developed by Kövér and Laricchia (2001) to study the energy and angular distribution of scattered e^+ and ejected e^- from e^+-atom and molecule ionizing collisions. The main advantage of the PPA is its time focussing, whereby e^+/e^- entering the analyzer at different angles arrive at the detector, located at the end of the second part of the PPA, at the same time. This is useful for enhancing signal-to-noise ratios at low energies.

The PPA consists of two identical aluminium analyzers arranged so that the angle between the base plates is 120°. The base and backplates are separated by a gap of 18mm. The large entrance and exit apertures are covered with a fine copper mesh (95% transmission) and all the metal surfaces are coated with graphite to reduce the emission of secondary electrons and to provide equipotential surfaces. On each side of the PPA, ten guard electrodes, consisting of copper bands mounted on a printed circuit board, are connected via a resistor chain to ensure that there are no fringing effects, by maintaining a uniform electric field at the edges. At the end of the second section of the PPA, CEM1 detects the energy-selected e^+/ e^- and fixed to the back plate of the

first section, a multi-channel plate detector (MCP) detects the incident e^+ beam (see figure 5.3).

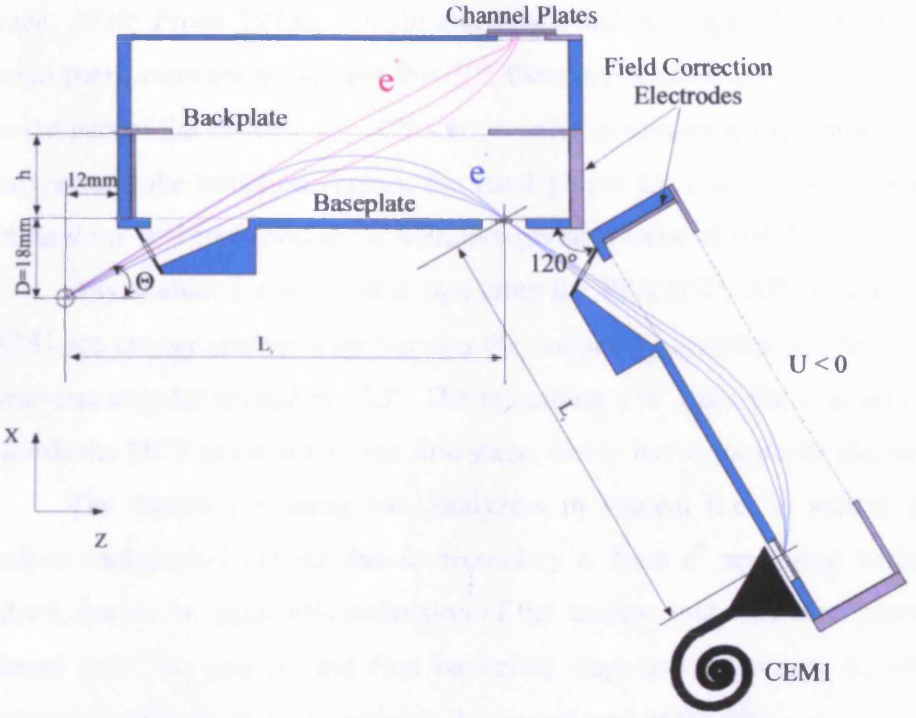

Figure 5.3: Schematic diagram of the cross-section of the Parallel Plate Analyzer (not to scale).

From the work of Kövér and Laricchia (2001), it is apparent that the focal length of a single PPA comprises three parts: the distance a particle travels in a field-free region, from the interaction region to the slit on the baseplate; the trajectory of the particle in the supposed uniform field between the plates to the earth plate; and the flight-path of the particle to the detector in a straight line.

The total focal length along the z-axis may therefore be expressed as:

$$L(\Theta,c) = (d_1 + d_2)\cot(\Theta) + 2\frac{Eh}{qU}\sin(2\Theta) = d\cot(\Theta) + \frac{2h}{c}\sin(2\Theta), \qquad (5.3)$$

where $d=d_1+d_2$ and d_1 and d_2 are the distances of the starting point and the focal point with respect to the baseplate, respectively; Θ is the entrance angle of the analyzer and h is the separation distance between the plates. $c = qU/E$ is a constant of the spectrometer, where q and E are the charge and energy of the particles, respectively, and U is the applied potential difference between the plates. As the baseplates are permanently grounded, U corresponds to the voltage, V_{ppa}.

The PPA was determined to have second order focusing properties at 30°, where the angular aberration has a minimum (Green and Proca, 1970; Proca and Green, 1970; Proca 1973a, 1973b; and Proca and Rüdinger, 1973) and as such the design parameters are set so that $\Theta = 30°$, therefore rendering the entrance angle to the second part of the PPA to $\Theta_2 = 60° - \Theta$. In order to maximise the distance between the analyzer and the collision region, the focal points are situated on the baseplates by setting $d_1=d=h=18$mm and $d_2=0$, therefore giving a value of $c=0.5$.

Any scattered e^+/ejected e^- that enter the PPA at 0° (±5°) and are detected by CEM1 are energy analyzed by varying the voltage V_{ppa} applied to the backplate. The transverse angular spread is ±15°. The remaining e^+/e^- from the collision is deflected towards the MCP at the top of the first stage, due to having opposite charge.

The reason for using two analyzers in tandem (i.e. in series) is to reduce random background counts due to secondary e^- from e^+ scattering within the PPA. Indeed, due to the parabolic deflection of the tandem analyzer, most secondary e^- are filtered out. The grid on the first backplate stops any secondary e^-, which mainly escape from the MCP, from entering the second part of the PPA.

5.3.3 Channeltron (CEM1)

A channeltron (model X919BL) supplied by Philips Ltd, shown in figure 5.3, is used to detect e^+/e^- whose energies correspond to the so-called 'pass-energy' of the PPA. This is set by the constant of the spectrometer (see section 5.3.2) as $E=qV_{ppa}/c$. CEM1 was also employed to measure the intensity of the direct beam and therefore to find the optimum electrostatic lens voltages for beam transport. The intensity of the beam was monitored for 10s before and after each run to check the stability of the incident e^+ count rate.

5.3.4 Energy Calibration for the Parallel Plate Analyzer

In order to energy calibrate the PPA, a procedure previously used by Kövér and Laricchia (1998) is employed. This is achieved by determining the ratio between the potential on the backplate of the PPA (V_{ppa}) and the energy of the particles passing through the analyzer. The energy of the e^+ emerging from the moderator is the sum of eV_m (where V_m is the moderator potential) and the initial energy of the ejected e^+, δE,

as discussed in section 5.2.2. By scanning with the potential V_{ppa}, the energy profile of the e^+ beam passing through the PPA could be determined. An example of which is shown in figure 5.4 for V_m ranging from 28 to 150V. The maximum of these energy profiles was taken as the correspondent e^+ energy.

A linear fit to these maximum values (see figure 5.5) gives V_{ppa} in terms of V_m, the spectrometer constant and the initial kinetic energy. For these e^+, the equation of the line was found to be:

$$V_{ppa} = 0.505(\pm 0.005)\times(V_m + 1.324(\pm 0.399)), \tag{5.4}$$

where the spectrometer constant is 0.505 and the e^+ emitted from the moderator have an average initial kinetic energy of 1.324eV. Therefore the impact energy of the e^+ beam is:

$$E_+ = eV_m + 1.324eV\,. \tag{5.5}$$

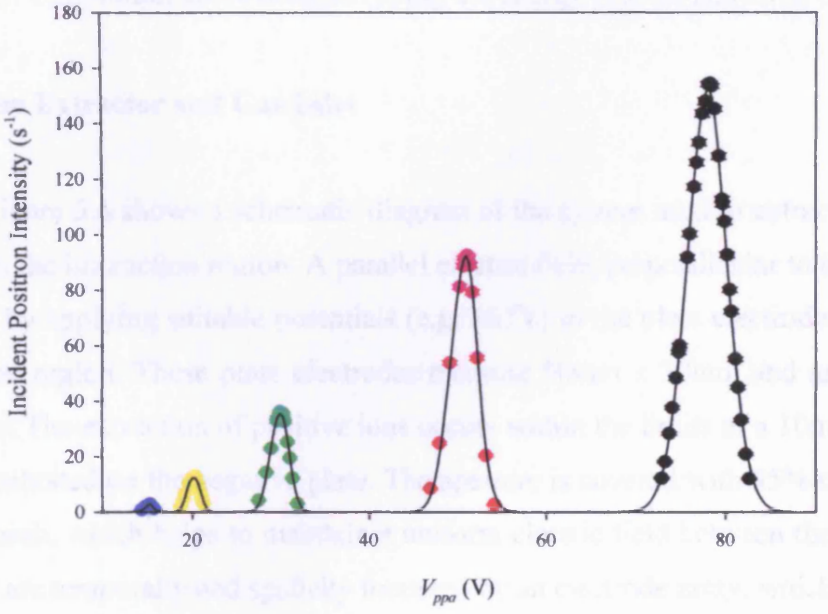

Figure 5.4: Beam energy profiles for 150.4, 97.4, 56.8, 37.8 and 27.8V moderator potentials.

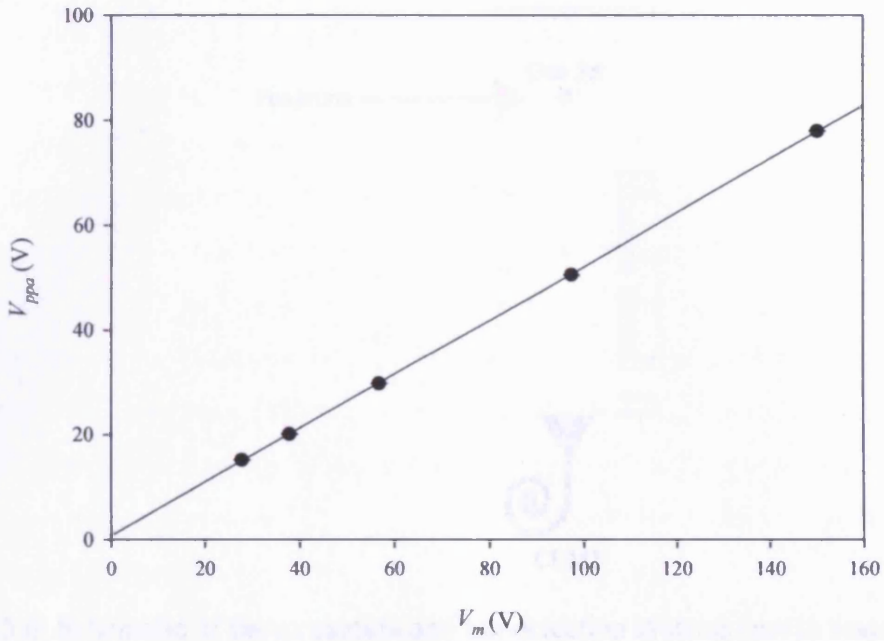

Figure 5.5: Calibration curve obtained using the energy profiles shown in figure 5.4.

5.3.5 Ion Extractor and Gas Inlet

Figure 5.6 shows a schematic diagram of the system used to extract and detect ions from the interaction region. A parallel electric field, perpendicular to the e^+ beam, is set up by applying suitable potentials (e.g. ±65V) to the plate electrodes across the interaction region. These plate electrodes measure 50mm x 30mm and are separated by 20mm. The extraction of positive ions occurs within the limits of a 10mm diameter aperture situated on the negative plate. The aperture is covered with 95% transmission copper mesh, which helps to maintain a uniform electric field between the electrodes. The ions are temporally and spatially focussed by an electrode array, which consists of a cylindrical lens with an external diameter of 20mm and internal diameter of 10mm, held at a potential of -130V. These ions are then accelerated by a 95% transmission copper grid held at a potential of -2.6kV before hitting the cone of the second channel electron multiplier detector (CEM2, Philips model X951BL) held at -2.5kV. The grid also caused secondary electrons to be reflected back towards the cone of the channeltron. The back of CEM2 is held at -500V and the signal pulses are decoupled from the high DC voltage by a 1nF capacitor.

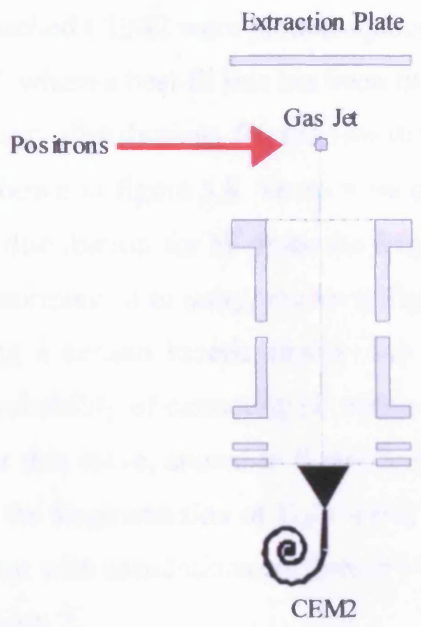

Figure 5.6: Schematic of the extraction and ion detection systems (not to scale).

In order to avoid the condensation of H_2O vapour on the gas outlet, a graphite nozzle (1mm diameter and 10mm length) is used to inject the gas beam into the system. The distance between the end of the gas inlet and the axis of the positron beam is 7.5mm. A home-made pressure controller was used to allow for the fine adjustment of the target gas flow by opening/closing a leak valve with feedback. The pressure of the target gas was measured directly above the nozzle using a capacitance manometer (MKS 127-AA). This pressure remained at ~0.65Torr (86.66Pa) throughout this study.

In order to correct the DDCS for protons (H^+) for the ion extraction efficiency, computer simulations of the trajectories for singly charged ions originating from the ionization (both dissociative and non-dissociative) of H_2O have been performed using CPO-3D (CPO Ltd). Unlike the parent ion, which has mostly thermal energies, the H^+ ions have energies ranging from thermal to a few eV. This means that the higher kinetic energy fragments are acquired less efficiently than the thermal ones (Maerk and Dunn, 1985). Therefore, the extraction efficiency was obtained by finding, from the simulation, the probability of extracting protons with a given kinetic energy from the system and convoluting this with the H^+ kinetic energy distributions for the two different states of water (i.e. 2-body final state: H^++OH, and 3-body final state: H^++O+H) measured by Cordaro *et al* (1986) for e^- impact. The simulated H^+ were taken to have both thermal energy and kinetic energies of 2 and 7eV and the intensity

of the simulated H^+ that reached CEM2 were plotted against their respective energies. This is shown in figure 5.7, where a best-fit line has been fitted to the data.

The H^+ kinetic energy distributions for the two different states of H_2O from Cordaro *et al* (1986) are shown in figure 5.8. These were convoluted together to find the overall kinetic energy distribution for H^+ from the fragmentation of H_2O and the area under this curve was normalised to unity, shown in figure 5.9a. This curve of the probability of a H^+ having a certain kinetic energy was then convoluted with the simulated results for the probability of extracting H^+ with a given kinetic energy from the system. The area under this curve, shown in figure 5.9b, represents the extraction efficiency for all H^+ from the fragmentation of H_2O within the system and the results found are in good agreement with simulations conducted by Arcidiacono (2006) using the ion optics program Simion 7.

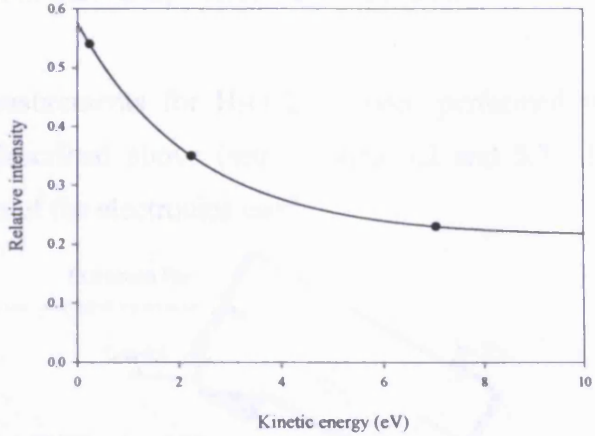

Figure 5.7: Probability of extracting H^+ with a given kinetic energy.

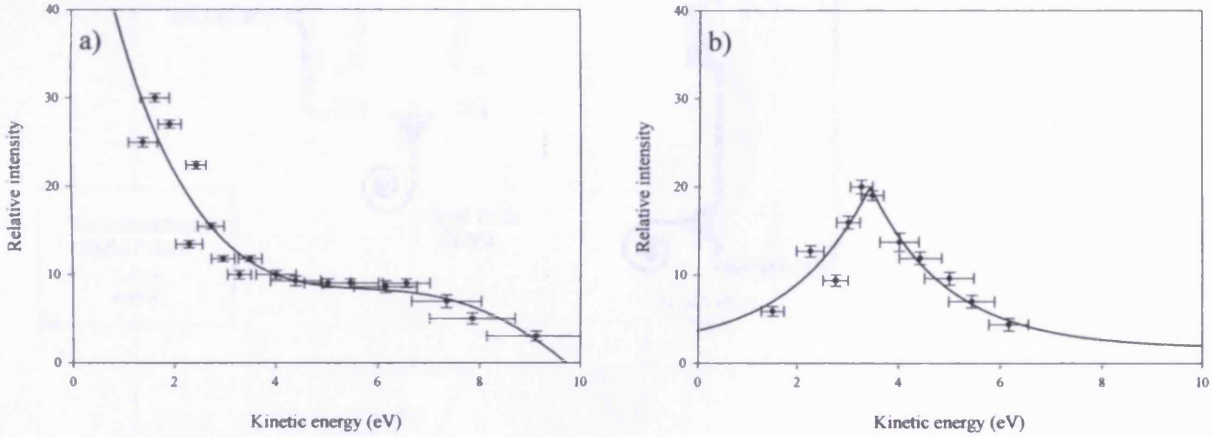

Figure 5.8: H^+ kinetic energy distributions from two states of H_2O that undergo dissociative autoionization: a) H^++OH state and b) H^++O+H state (Cordaro *et al* 1986).

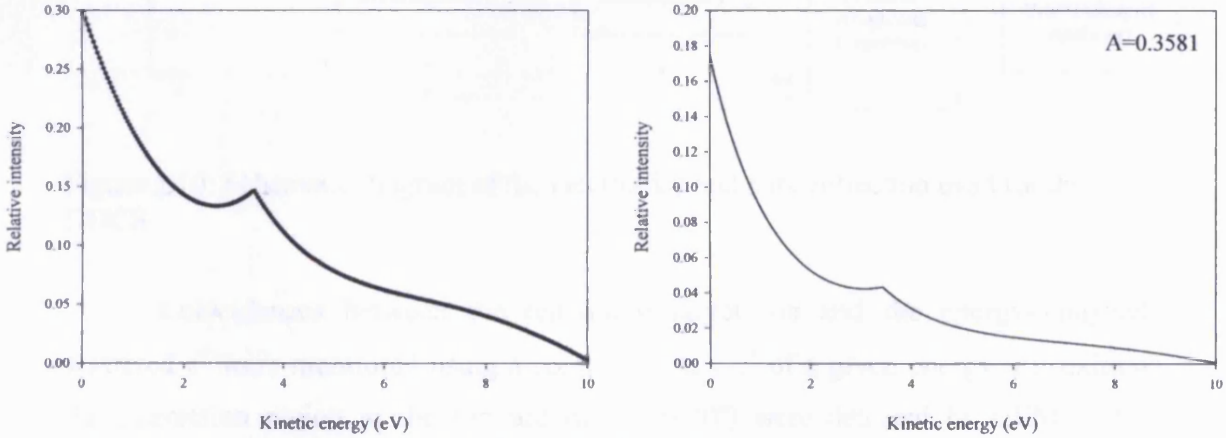

Figure 5.9: a) The convoluted H^+ kinetic energy distribution from the two states of H_2O of Cordaro *et al* (1986) and b) the extraction efficiency for H^+ within the electrostatic system.

5.4 Electronics and Experimental Method

DDCS measurements for H_2O have been performed with the electrostatic beam apparatus described above (see sections 5.2 and 5.3). Figure 5.10 shows a schematic diagram of the electronics used.

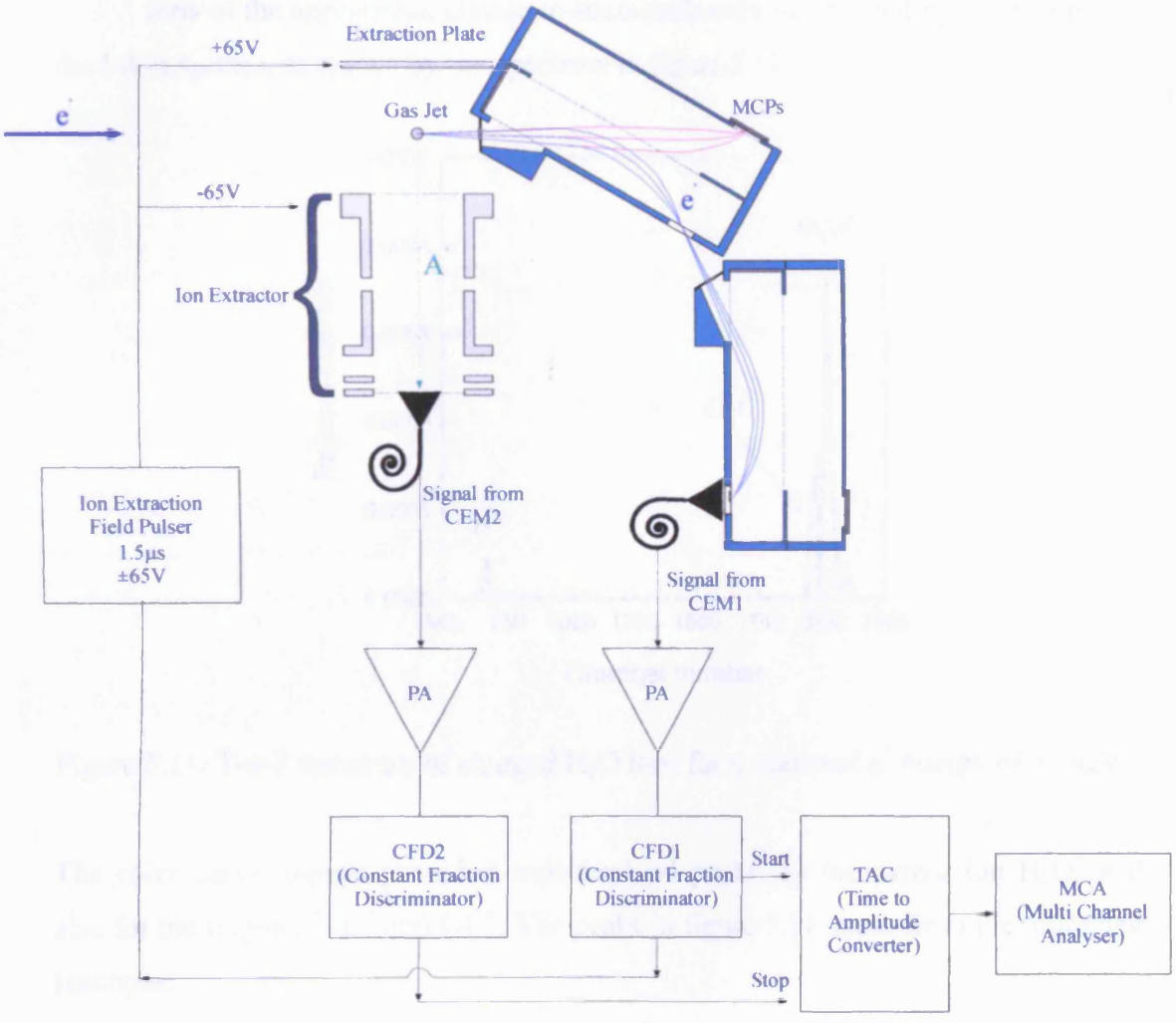

Figure 5.10: Schematic diagram of the electronics and data collection used for the DDCS.

Coincidences between the remaining target ion and the energy-analyzed scattered e^+ were monitored using a computer. Any e^+ of a given energy, E_+, exiting the interaction region in the forward direction (0^o) were detected by CEM1 after passing through the PPA. The amplified signal from the detected e^+ was fed into an Ortec 584 Constant Fraction Discriminator (CFD1), before being used as the start pulse for an Ortec 567 Time to Amplitude Converter (TAC). The signal from the ions

detected by CEM2 was amplified and fed into an Ortec 584 (CFD2), before being used as the stop pulse for the TAC, which in turn was fed into a PC-based multichannel analyzer (Ortec MCA). The ion extraction field between the two parallel plates was established using pulses of ±65V with a width of 1.5μs supplied by a multipulser (Carroll & Meynell Ltd), which were applied once the e^+ was detected.

Ions of the appropriate charge-to-mass ratio may be selected by their T-o-F on the MCA spectra, as shown by the spectrum in figure 5.11.

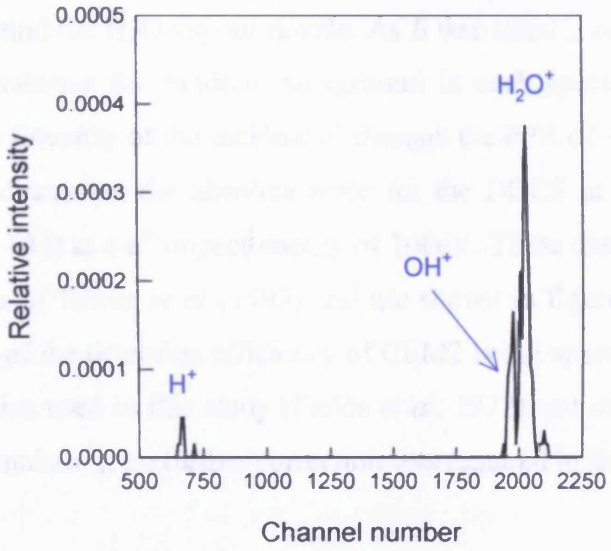

Figure 5.11: T-o-F spectrum of charged H_2O ions for a scattered e^+ energy of 37.4eV.

The coincidence signals provided well-resolved peaks for the parent ion H_2O^+ and also for the fragments H^+ and OH^+. The peaks in figure 5.11 occur from the following reactions:

$$e^+(100eV) + H_2O \rightarrow e^- + e^+(0°, 37.4eV) + H_2O^+ \quad (E_{th} = 12.6eV), \tag{5.6}$$

$$e^+(100eV) + H_2O \rightarrow e^- + e^+(0°, 37.4eV) + OH + H^+ \quad (E_{th} = 16.95eV), \tag{5.7}$$

$$e^+(100eV) + H_2O \rightarrow e^- + e^+(0°, 37.4eV) + H + OH^+ \quad (E_{th} = 18.116eV), \tag{5.8}$$

where E_{th} corresponds to the threshold energy.

To extract the DDCS from the measured coincidences, the following procedure was employed: following subtraction of the random background, the areas under the peaks seen in the T-o-F spectra were integrated to find the yields;

$$Y_{DDCS} \propto \frac{C-B}{pN_{+}E_{+}}, \tag{5.9}$$

where C and B are the total number of e^+-ion coincidences in gas and vacuum, respectively, N_+ is the total number of incident e^+, E_+ is the e^+ energy selected by the PPA (to correct for the variation of the analyzer transport efficiency) and p is the driving pressure behind the H_2O vapour nozzle. As B was usually close to zero, it was only necessary to subtract the random background in each spectrum, leading to a typical value for the intensity of the incident e^+ through the PPA of ~$100s^{-1}$.

In order to determine the absolute scale for the DDCS of H_2O, yields were measured for argon (Ar) at a e^+ impact energy of 100eV. These data were normalised to the previous data of Kövér *et al* (1993) and are shown in figure 5.13. Due to the energy dependence of the detection efficiency of CEM2 being approximately constant at the impact energies used in this study (Fields *et al*, 1977) and close to 50% for all ions (i.e. H^+, H_2O^+ and Ar^+), no further correction was required in the normalization.

5.5 Results

The absolute DDCS around 0° for non-dissociative and dissociative ionization reactions are shown in figure 5.12 for 100eV and 153eV e^+ impact energies. The cross-section for the parent ion, H_2O^+, for 100 and 153eV impact energy exhibits a similar pattern to those of the fragment ions, OH^+ and H^+, although the statistical uncertainty for the fragment ions is greater than the parent ion at present. Each DDCS curve is characterised by a slow rise, followed by a monotonic decrease from the peak at the ionization limit. No significant structure which may be attributed to ECC is seen in the results. The DDCS for the parent ion have a maximum of ~$0.11x10^{-20}m^2$/sr/eV and ~$0.09x10^{-20}m^2$/sr/eV for 100eV and 153eV, respectively. This is a factor of seven times higher than for the production of OH^+, whereas the magnitude for the production of H^+ and OH^+ at these energies are comparable, within statistical uncertainties. It is also apparent that the peak for H_2O^+ is slightly broader for 153eV.

In figure 5.13, the DDCS for 100eV e^+ impact on H_2O is compared with that for Ar (Kövér *et al*, 1993). The shape of the DDCS for H_2O vapour is similar to that measured for Ar, but is greater in magnitude. Indeed, the ratio between the area of each DDCS to its corresponding direct ionization cross-section for 100eV e^+ impact (Arcidiacono *et al*, 2007; Moxom *et al*, 1996) has been determined to be a factor of ~1.5 higher for H_2O than for Ar. This indicates a higher probability for forward inelastic scattering of the projectile at an acceptance polar angle of ±5°.

In figures 5.14 and 5.15, the branching ratios for OH^+/H_2O^+ and H^+/H_2O^+ from 100eV and 153eV e^+ impact, respectively, are shown. Due to the lack of corresponding DDCS data for e^- impact, the branching ratios from the integral ionization cross-section for e^- incident at the same energy (Lindsay and Mangan, 2003) are also indicated within the figures.

The ratios for OH^+/H_2O^+ have values similar to those for e^- impact for the two e^+ impact energies: ~32% in each case, whilst the ratios for H^+/H_2O^+ are a factor of 3.4 and 2.6 lower than for e^- impact: 27% and 31%, respectively. However, correcting the branching ratios for H^+/H_2O^+ for the probability of extracting the H^+ fragments from the interaction region (~36%, see section 5.3.5 for details), also shown in figure 5.14 and 5.15, renders the values similar to those for e^- impact.

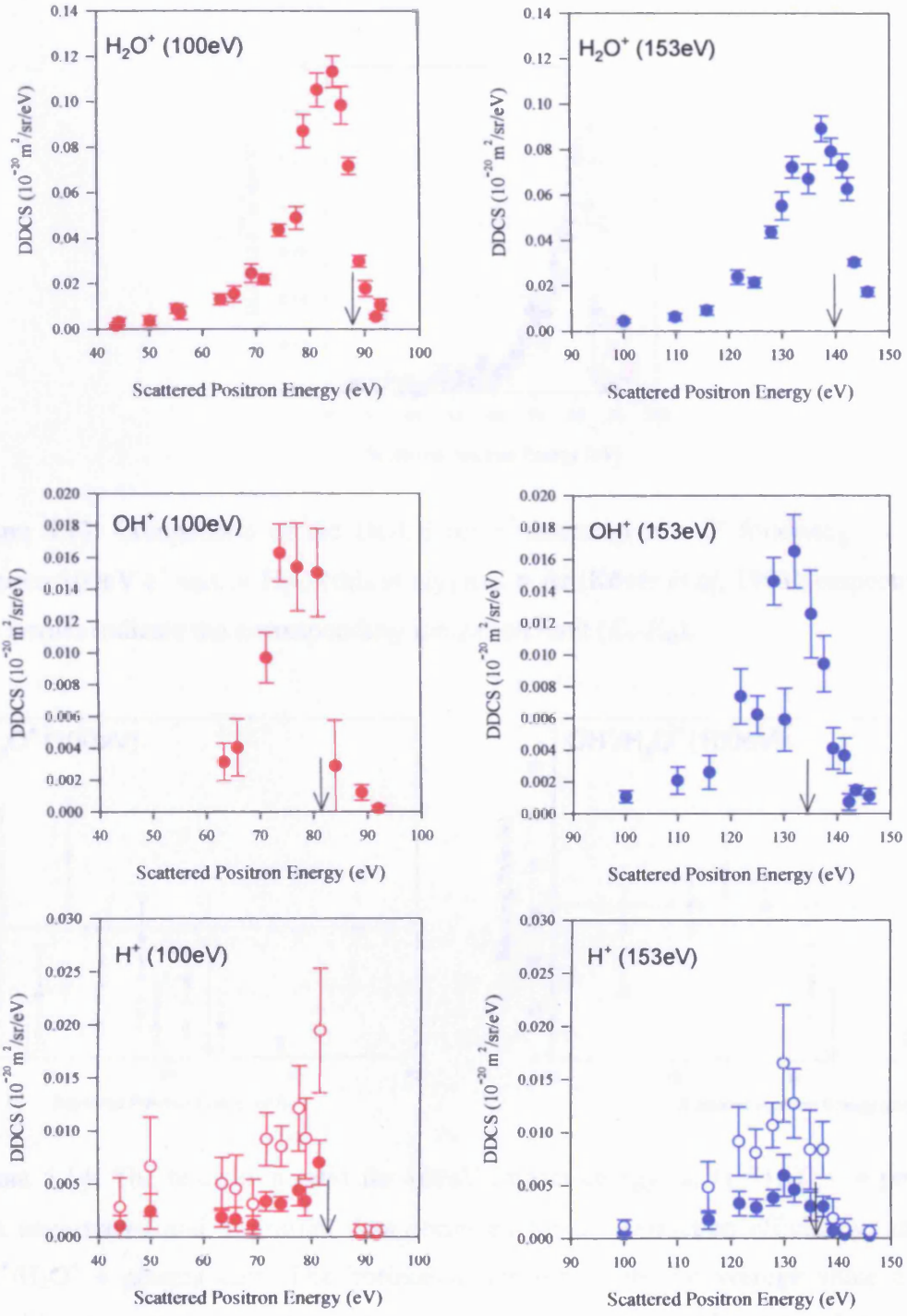

Figure 5.12: DDCS at 0° for e^+ (100 and 153eV) – H_2O collisions of the following ions: H_2O^+, OH^+, H^+. ○ and ○ represent the H^+ DDCS corrected for the extraction efficiency. The arrows indicate the corresponding ionization limit (E_+-E_{th}).

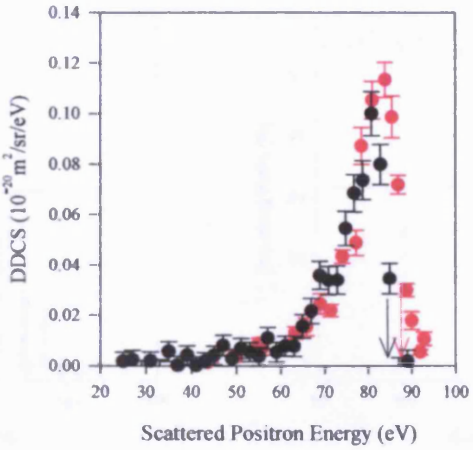

Figure 5.13: Comparison of the DDCS for e^+ scattered at ~ 0° following collision between 100eV e^+ and: ● H_2O (this study) and ● Ar (Kövér *et al*, 1993), respectively. The arrows indicate the corresponding ionization limit (E_+-E_{th}).

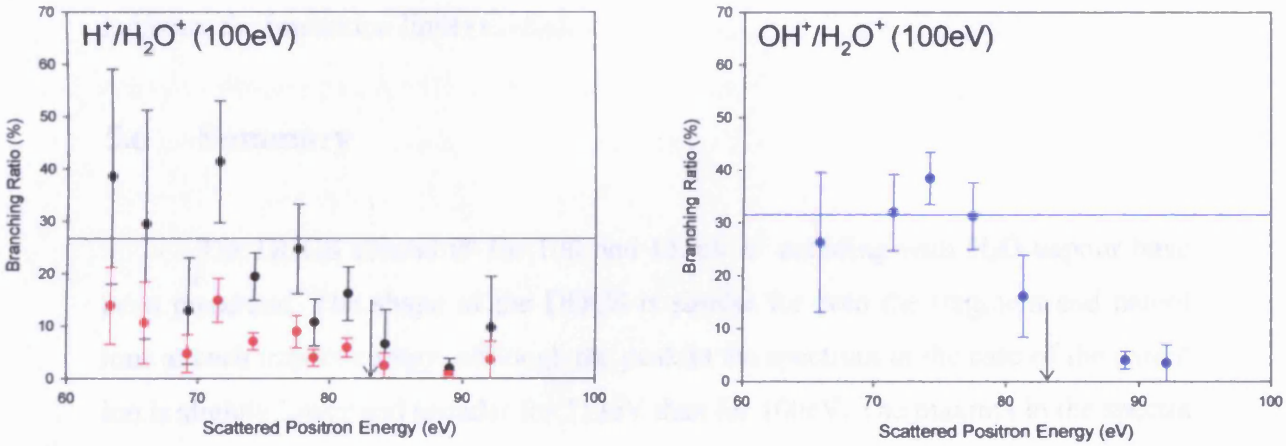

Figure 5.14: The branching ratio for 100eV impact energy: a) H^+/H_2O^+ – ● present data uncorrected and ● present data corrected for the extraction efficiency, and b) OH^+/H_2O^+ ● present data. The horizontal line represents the average value of the branching ratio from the integral ionization cross-section for e^- impact and the arrow indicates the ionization limit (E_+-E_{th}).

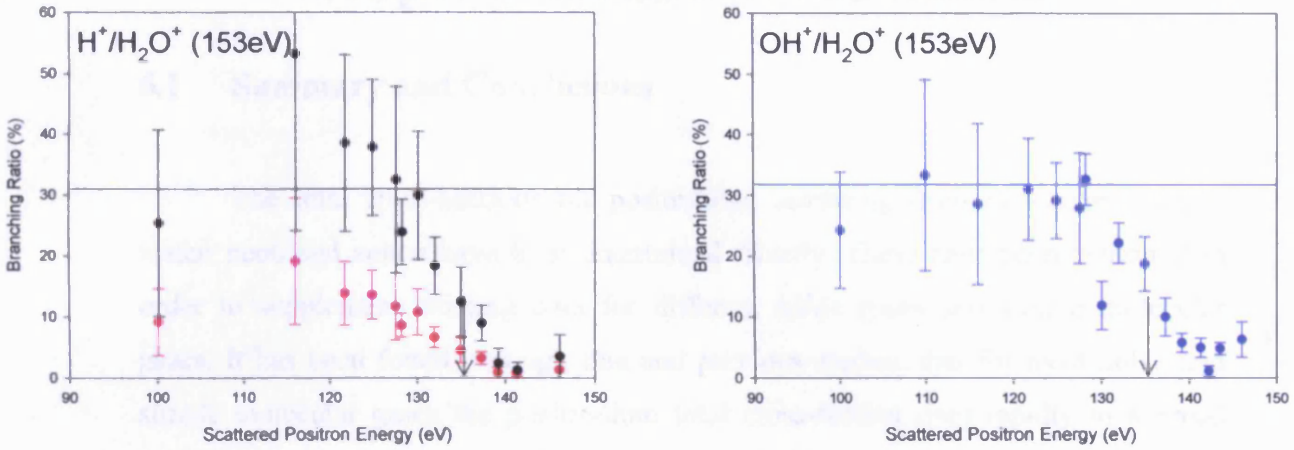

Figure 5.15: The branching ratio for 153eV impact energy: a) H^+/H_2O^+ – ● present data uncorrected and ● present data corrected for the extraction efficiency, and b) OH^+/H_2O^+ – ● present data. The horizontal line represents the average value of branching ratio from the integral ionization cross-section for e^- impact and the arrow indicates the ionization limit (E_+-E_{th}).

5.6 Summary

The DDCS around 0° for 100 and 153eV e^+ colliding with H_2O vapour have been presented. The shape of the DDCS is similar for both the fragment and parent ions at each impact energy, although the peak in the spectrum in the case of the parent ion is slightly lower and broader for 153eV than for 100eV. The maxima in the spectra from the fragment ions are also similar within statistical uncertainties, but are a factor of six to seven less than that of the parent ion. At 100eV, the DDCS near 0° for e^+ colliding with H_2O vapour has also been found to be greater in magnitude than in the case of Ar, despite a larger integral cross-section for Ar. This implies that the forward inelastic scattering of the projectile is higher for H_2O than for Ar. However, as in the DDCS for Ar, the present data show no significant structure due to the ECC phenomenon. Finally, the branching ratios of the DDCS for OH^+/H_2O^+ and H^+/H_2O^+ have been obtained and are found to be similar to those by e^- impact after correcting for the extraction efficiency for H^+.

Chapter 6: Conclusions and Outlook

6.1 Summary and Conclusions

The total cross-sections for positronium scattering from molecular oxygen, water, neon and xenon have been determined directly. These have been measured in order to supplement existing data for different noble gases and simple molecular gases. It has been found, through this and previous studies, that for most noble and simple molecular gases the positronium total cross-section rises rapidly to a broad peak before decreasing again at the higher energies. The magnitude and width of the broad peak is found to grow with increasing complexity of the target gas. For water and possibly neon the total cross-section is roughly constant across the energy range investigated.

The positronium total cross-sections have been compared with corresponding data for hydrogen, positron and electron impact, as well as available theoretical calculations and momentum transfer cross-section data. For molecular oxygen, water and neon, the total cross-section has been found to lie closer to the corresponding electron total cross-section (uncorrected for forward scattering) rather than that of the positron, whilst results for atomic hydrogen are similar in magnitude to those for positronium. Positron total cross-sections for water vapour have also been measured so as to ascertain the general performance of the system with respect to water vapour. These measurements were compared with other positron total cross-sections for water vapour where they were found to follow closely the results of Sueoka *et al* (1986), whilst lying below those of Kimura *et al* (2000), who corrected the data of Sueoka *et al* (1986) for forward scattering effects using electron differential cross-sections. The data of Kimura *et al* (2000) are found to be a lot higher than all the other positron data.

The absolute integrated cross-section for positronium in collision with xenon atoms, along with the longitudinal energy distributions of the residual positrons and electrons for an impact energy of 30eV, have been determined using a retarding field analyzer and a floating scattering cell. These have been measured to probe possible contributions from target ionization through positronium impact. The positron data have been found to agree fairly well with the impulse approximation of Starrett *et al*

(2005) for the longitudinal energy distribution, but not for the integrated cross-section. This is partly due to the rather large errors in the longitudinal energy distribution and also implies that the calculation may require inclusion of doubly inelastic processes. The electron data follows the theoretical determination of Starrett *et al* (2005) for the longitudinal energy distribution at energies greater than 15eV, but not at the lowest energies where it is higher. The uncorrected/corrected electron integrated cross-section is a factor of (1.5/1.4)±0.1 higher than for the positron data. This gives a clear indication of the occurrence of target ionization.

Finally, the doubly differential ionization cross-section for positron-water scattering around 0° has been determined at impact energies of 100 and 153eV using an electrostatic system. These have been measured for their intrinsic interest and to check for any evidence of Electron Capture to the Continuum (ECC) within the doubly differential ionization cross-section of a polar target. The shape of the doubly differential ionization cross-section for water has been found to be similar for both the fragment and parent ions at each of the two impact energies. The cross-sections for the fragment ions exhibit maxima which have also been found to be similar in shape, within statistical uncertainties, to those seen in the case of the parent ion, but are a factor of ~six to seven lower. The peak in the cross-section for the parent ion has been found to be slightly lower and broader for 153eV than for 100eV. At 100eV, the doubly differential ionization cross-section near 0° for positrons colliding with water vapour has also been found to be greater in magnitude than in the case of argon, despite a larger integral cross-section for argon. This implies that the forward inelastic scattering of the projectile is higher for water than for argon.

As in the doubly differential ionization cross-section for argon, the present data show no significant structure due to the ECC phenomenon, which would be at around half the residual energy. Finally, the branching ratios of the doubly differential ionization cross-section for OH^+/H_2O^+ and H^+/H_2O^+ have been obtained and are found to be similar to those for electron impact, after correction for the extraction efficiency for protons.

6.2 Outlook and Suggestions for Future Work

Further work is needed to finalise the total cross-section results for positronium- molecular oxygen and to verify the reproducibility of the observed scatter. Also, measurements may be made from krypton to compare the noble gases and to investigate whether it lies in between the electron and positron total cross-section at the lowest velocities, as is the case for xenon. The uncertainty on the positronium total cross-section at the lowest energies may be reduced by an improvement of the energy resolution and intensity of the positronium beam by installing a new source and improving the efficiency of the rare gas solid moderator (i.e. by using krypton and neon as the rare gas).

The investigation into the detection of residual positrons and electrons from the fragmentation of positronium in collision with xenon may be extended to higher energies to improve statistics and to check for convergence with theory. Also, the cell design for use in the fragmentation studies has been found to be a good extractor of ions and therefore it would be possible to carry out coincidence measurements between the residual particle/positronium and the ions.

Finally, it would be of interest to investigate the doubly differential cross-section for positron impact ionization of other polar molecules, such as NH_3, SO_2 and H_2S and to study biomolecules as it may aide in quantifying radiation damage in the human body when subjected to positron emission tomography (Champion and Le Loirec, 2006).

Appendix A

Determination of Detection Probability of Forward Scattered Positrons

The detection probability of forward scattered positrons (e^+), P_{fs}, was calculated by finding the maximum pitch angle at which elastically scattered e^+ would be detected at a given incident energy taking into account the magnetic field gradient:

$$\frac{B_{cell}}{B_{CEMA}} \propto \frac{\sin^2 \theta_{cell}}{\sin^2 \theta_{CEMA}}, \qquad \text{(A.1)}$$

where B_{cell} is the magnetic field in the region of the scattering cell (4mT), B_{CEMA} is the magnetic field at the detectors (22mT), and θ_{cell} and θ_{CEMA} are the corresponding pitch angles (see next page for calculating the angles). The calculation was performed, as in the experiment (see section 3.4.4), by using only the high energy part of the incident e^+ beam i.e. from eV_r to eV_r+3eV, where V_r is the retarding potential applied to R2/R3. The incident e^+ beam energy profile is shown in figure A.1 along with a detailed view of the region of interest.

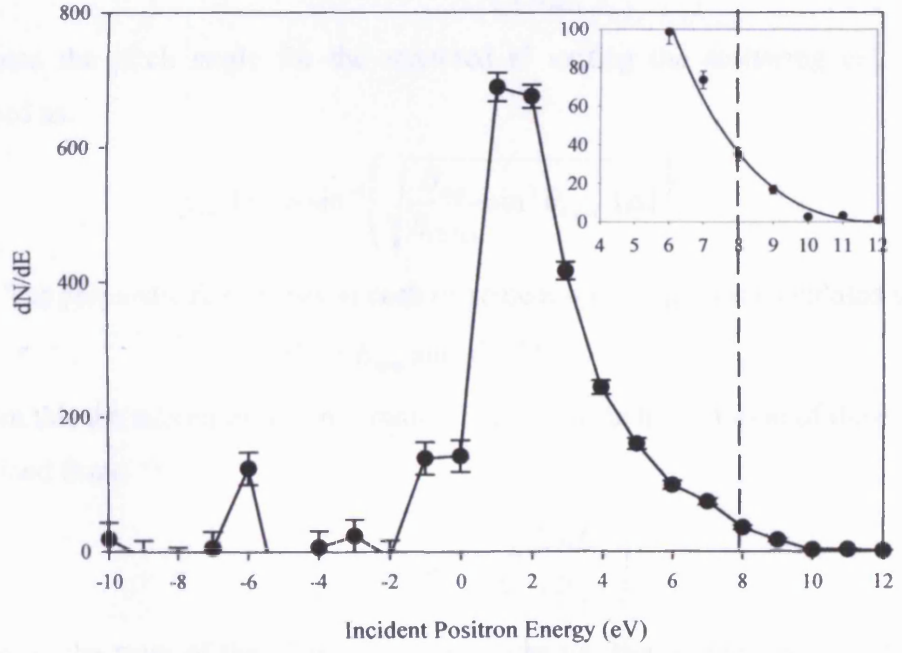

Figure A.1: The e^+ beam energy profile obtained with V_s=20V. Inset is an expanded view of the region of interest.

The energy range investigated was 8-11eV, which corresponds to eV_r (E_{min}) to eV_r+3eV (E_{max}) and the number of e^+ which were forward scattered at each incremental energy step of 0.0117eV within this energy range was calculated.

Due to some helical motion of the scattered e^+, the longitudinal energy ($E_{//}$) would be less than or equal to their maximum energy, E_{max} (see figure A.2).

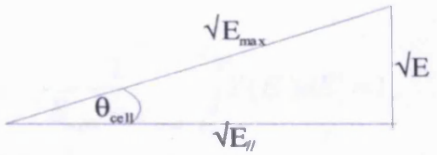

Figure A.2: Diagram to clarify pitch angle and the longitudinal energy of the scattered e^+ detected at CEMA.

Therefore, the longitudinal energy of the scattered e^+ for each incremental energy step (E) of 0.0117eV from E_{min} to E_{max} was defined as:

$$E_{//} \leq E_{max} - E\,. \tag{A.2}$$

From this, the angle of the helical motion of the e^+ at the detector was calculated using:

$$\theta_{CEMA}(E) = \cos^{-1}\left(\sqrt{\frac{E_{//}}{E_{max}}}\right) \tag{A.3}$$

and hence the pitch angle for the scattered e^+ exiting the scattering cell may be expressed as:

$$\theta_{cell}(E) = \sin^{-1}\left(\sqrt{\frac{B_{cell}}{B_{CEMA}}\sin^2\theta_{CEMA}(E)}\right) \tag{A.4}$$

The perpendicular energy at each increment up to E_{max} was calculated using:

$$E_{\perp} = E_{max}\sin^2\theta_{cell}(E) \tag{A.5}$$

and from this the maximum Larmor radius, r_{max}, of the helical motion of the e^+ was determined from:

$$r_{max}(E) = \sqrt{\left(\frac{2mE_{\perp}}{eB_{cell}^2}\right)} \tag{A.6}$$

where m is the mass of the e^+ and e is the e^+ charge. Hence, the fraction of forward scattered e^+ which may be detected can be expressed as:

$$F(E) = \frac{(r_{cell} - r_{\max}(E))^2}{r_{cell}^2} \tag{A.7}$$

where r_{cell} is the radius of the exit aperture for the scattering cell i.e. 4mm (see section 3.3.2).

The beam profile shown in figure A.1 was then fitted to a curve $Y(E')$ such that:

$$\frac{1}{E_{\max} - E_{\min}} \int_{E_{\min}}^{E_{\max}} Y(E'')dE'' = 1, \tag{A.8}$$

Therefore, the overall probability for detection of forward scattered e^+ over all angles from the minimum pitch angle (i.e. E_{min}) to the maximum pitch angle (i.e. E_{max}) is given by:

$$P_{fs}(E) = F(E) \int_{E}^{E_{\max}} Y(E')dE', \tag{A.9}$$

where $\int_{E}^{E_{\max}} Y(E')dE'$ is the fraction of incident e^+ at each energy within the energy range E to E_{max}.

The final results are displayed in figure A.3 (also shown in chapter 3) where they are plotted with respect to the pitch angle, θ_{cell}.

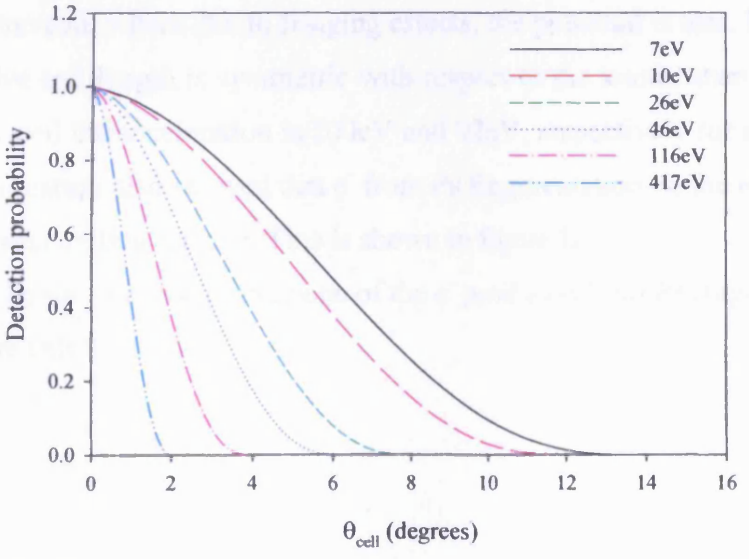

Figure A.3: Dependence of the detection probability upon pitch angle at each incident e^+ energy investigated.

Appendix B

CPO Simulation of the Scattering Cell used for Positronium Fragmentation Studies:

To ensure that the background due to secondary electrons was kept to a minimum, a new scattering cell was designed for the positronium (Ps) fragmentation and target ionization study (as discussed in chapter 4). This cell was biased in order to accelerate the residual electrons (e^-) from Ps fragmentation and target ionization out of the cell, as well as to repel secondary e^-. The cell was also designed to allow the incident Ps beam to enter the cell without intercepting the entrance aperture and to stop any electrons released from Ps fragmenting on the exit aperture from escaping the cell (see section 4.2). Therefore, using the simulation program CPO-3D (CPO Ltd), a number of different designs were tried and tested. The final cell design is shown in figure 4.1.

The variation of the applied potential with respect to the distance along the cell body is shown in figure 4.2, for an applied potential of -100V, calculated from the simulation. Within this figure, the residual e^- are accelerated by 100eV, except at the very edges of the cell, where due to fringing effects, the potential is less. By assuming that the effective cell length is symmetric with respect to the x-axis, then at the edges of the effective cell the acceleration is 100eV and 92eV, respectively for a potential of -100V. The simulation also showed that e^- from Ps fragmentation on the exit apertures were stopped from exiting the cell. This is shown in figure B.1.

As can be seen in this figure, none of the e^- produced from Ps fragmentation on the exit aperture exit the cell.

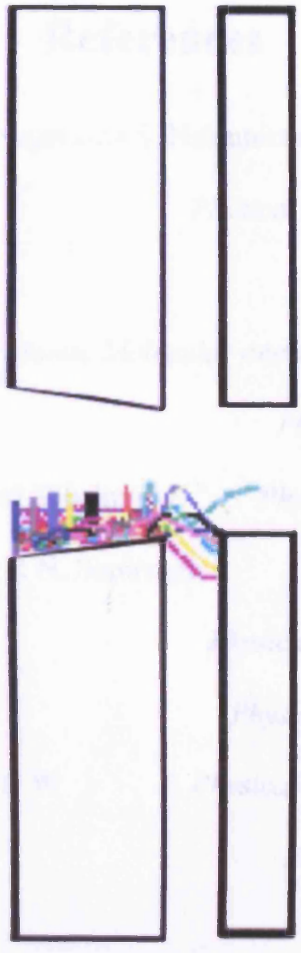

Figure B.1: CPO-3D simulation of Ps fragmentation on the exit aperture of the cell (scaled by 1.75): e^- start from exit aperture and are shown by the coloured paths; simulated for an applied potential of -100V on the cell and the apertures are held at ground.

References

Adachi S, Chiba M, Hirose T, Nagayama S, Nakamitsu Y, Sato T and Yamada T

Physical Review Letters ***65*** *(1990) 2634*

Adhikari S K and Mandal P

Journal of Physics B: Atomic Molecular and Optical Physics ***33*** *(2000) L761*

Adkins G S *Physical Review A* ***27*** *(1983) 530*

Adkins G S, Salahuddin A A and Schalm K E *Physical Review A* ***45*** *(1992) 7774*

Adkins G S, McGovern N, Fell R N, Sapirstein J

Physical Review A ***68*** *(2003) 032512-1*

Adkins G S *Physical Review A* ***72*** *(2005) 032501*

Al-Ramadhan A H and Gidley D W *Physical Review Letters* ***72*** *(1994) 1632*

Anderson C D *Physical Review* ***41*** *(1932a) 405*

Anderson C D *Science* ***76*** *(1932b) 238*

Anderson C D *Physical Review* ***43*** *(1933) 491*

Arcidiacono C, Kövér A and Laricchia G *Physical Review Letters* ***95*** *(2005) 223202*

Arcidiacono C *PhD Thesis (2006) University College London*

Arcidiacono C, Kövér Á, Pešić Z D, Beale J and Laricchia G

Radiation Physics and Chemistry ***76*** *(2007) 431*

Armitage S *PhD Thesis (2002) University College London*

Armitage S, Leslie D E, Garner A J and Laricchia G

Physical Review Letters ***89*** *(2002) 173402-1*

Armitage S, Leslie D E, Beale J and Laricchia G

Nuclear Instruments and Methods in Physics Research B ***247*** *(2006) 98*

Armitage S, Beale J, Brawley S, Leslie D E and Laricchia G *In preparation (2007)*

Baluja K L and Jain A *Physical Review A* ***45*** *(1992) 7838*

Bandyopadhyay A, Roy K, Mandal P and Sil N C

Journal of Physics B: Atomic Molecular and Optical Physics **27** *(1994) 4337*

Basu A, Sinha P K and Ghosh A S *Physical Review A* **63** *(2001) 052503*

Bellotti E, Corti M, Fiorini E, Liguori C, Pullia A, Sarracino A, Sverzellati P and Zanotti L *Physics Letters B* **124** *(1983) 435*

Berakdar J *Physical Review Letters* **81** *(1998) 1393*

Biswas P K and Adhikari S K *Physical Review A* **59** *(1999) 363*

Biswas P K and Adhikari S K

Journal of Physics B: Atomic Molecular and Optical Physics **33** *(2000) 1575*

Blackett P M S and Occhialini G P S

Proceedings of the Royal Society of London A **139** *(1933) 699*

Blackwood J E, Campbell C P, McAlinden M T and Walters H R J

Physical Review A **60** *(1999) 4454*

Blackwood J E, McAlinden M T and Walters H R J

Journal of Physics B: Atomic Molecular and Optical Physics **35** *(2002) 2661*

Bransden B H *"Case study in atomic collision" eds. McDaniel and McDowell (North Holland) (1969) 171*

Brauner M and Briggs J S

Journal of Physics B: Atomic Molecular and Optical Physics **19** *(1986) L325*

Brauner M, Briggs J S and Klar H

Journal of Physics B: Atomic Molecular and Optical Physics **22** *(1989) 2265*

Brauner M and Briggs J S

Journal of Physics B: Atomic Molecular and Optical Physics **24** *(1991) 2227*

Canter K F, Lippel P H, Crane W S and Mills A P Jr *Positron Studies of Solids, Surfaces and Atoms (1986) (Singapore: World Scientific) 199*

Champion C and Le Loirec C *Physics in Medicine and Biology* **51** *(2006) 1707*

Chang T, Li Q. Wang Y and Li Y *"Positron Annihilation" eds. Coleman P, Sharman S C and Diana L M (North Holland: Amsterdam) (1982) 32*

Chang T, Li Q. Wang Y and Li Y *"Positron Annihilation" eds. Jain P C, Singru R M and Gopinathan K P (Singapore: World Scientific) (1985) 212*

Charlton M *Reports on the Progress in Physics* **48** *(1985) 737*

Charlton M and Laricchia G *Journal of Physics B: Atomic Molecular and Optical Physics* **23** *(1990) 1045*

Charlton M and Humberston J W *'Positron Physics' (Cambridge University Press) (2001)*

Coleman P G, Griffith T C, Heyland G R and Killeen T L *Journal of Physics B: Atomic Molecular and Optical Physics* **8** *(1975) L185*

Coleman P G, Rayner S, Jacobsen F M, Charlton M and West R N *Journal of Physics B: Atomic Molecular and Optical Physics* **27** *(1994) 981*

Coleman P G *Nuclear Instruments and Methods in Physics Research B* **192** *(2002) 83*

Cordaro R B, Hsieh K C and McIntyre L C Jr *Journal of Physics B: Atomic Molecular and Optical Physics* **19** *(1986) 1863*

Czernin J and Phelps M E *Annual Review of Medicine* **53** *(2002) 89*

Dababneh M S, Kauppila W E, Downing J P, Laperriere F, Pol V, Smart J H and Stein T S *Physical Review A* **22** *(1980) 1872*

Dababneh M S, Hsieh Y-F, Kauppila W E, Pol V and Stein T S *Physical Review A* **26** *(1982) 1252*

Dababneh M S, Hsieh Y-F, Kauppila W E, Kwan C K and Smith S J *Physical Review A* **38** *(1988) 1207*

Dale J M, Hulett L D and Pendyala S *Surface and Interface Analysis* **2** *(1980) 199*

De-Heng S, Jin-Feng S, Xiang-Dong Y, Zun-Lue Z and Yu-Fang L

Chinese Physics ***13*** *(2004) 1018*

De-Heng S, Yu-Fang L, Jin-Feng S, Zun-Lue Z and Xiang-Don Y

Chinese Physics ***14*** *(2005) 964*

Deutsch M *Physical Review* ***82*** *(1951) 455*

Dirac P A M *Proceedings of the Royal Society of London A* ***126*** *(1930a) 360*

Dirac P A M *Proceedings of the Cambridge Philosophical Society* ***26*** *(1930b) 361*

Dugdale S B, Alam M A, Fretwell H M, Biasini M and Wilson D

Journal of Physics: Condensed Matter ***6*** *(1994) L435*

Dupasquier A *POS81 (1981) 510*

Dupasquier A and Zecca A *Rivista Del Nuovo Cimento* ***8*** *(1985) 2276*

Ferrell R A *Physical Review* ***110*** *(1958) 1355*

Fields S A, Burch J L and Oran W A *Review of Scientific Instruments* ***48*** *(1977) 1076*

Finch R M *PhD Thesis (1996) University College London*

Fiol J, Rodriguez V D and Barrachina R O

Journal of Physics B: Atomic Molecular and Optical Physics ***34*** *(2001) 933*

Fulton T and Martin P C *Physical Review* ***95*** *(1954) 811*

Gao R S, Johnson L K, Smith K A and Stebbings R F

Physical Review A ***40*** *(1989) 4914*

Garner A J, Laricchia G and Özen A

Journal of Physics B: Atomic Molecular and Optical Physics ***29*** *(1996) 5961*

Garner A J, Özen A and Laricchia G

Nuclear Instruments and Methods in Physics Research B ***143*** *(1998) 155*

Garner A J, Özen A and Laricchia G

Journal of Physics B: Atomic Molecular and Optical Physics ***33*** *(2000) 1149*

Gianturco F A, Mukherjee T and Occhigrossi A *Physical Review A* ***64*** *(2001) 032715*

Gorfinkiel J D, Morgan L A and Tennyson J

Journal of Physics B: Atomic Molecular and Optical Physics ***35*** *(2002) 543*

Greaves R G and Surko C M *Canadian Journal of Physics* ***74*** *(1996) 445*

Greaves R G, Gilbert S J and Surko C M *Applied Surface Science* ***194*** *(2002) 56*

Green T S and Proca G A *Review of Scientific Instruments* ***41*** *(1970) 1409*

Gullikson E M and Mills A P Jr. *Physical Review Letters* ***57*** *(1986) 376*

Harting E and Read F H *Electrostatic Lenses (1976) (Amsterdam: Elsevier)*

Hautojärvi P *Positron in Solids, Topics in Current Physics No. 12 (Springer, Berlin) (1979)*

Heyland G R, Charlton M, Griffith T C and Wright G L

Canadian Journal of Physics ***60*** *(1982) 503*

Hodges C H *Physical Review Letters* ***25*** *(1970) 284*

Hoffman K R, Dababneh M S, Hsieh Y-F, Kauppila W E, Pol V, Smart J H and Stein T S *Physical Review A* ***25*** *(1982) 1393*

Hutchins S M, Coleman P G, Stone R J and West R N

Journal of Physics E: Scientific Instrumentation ***19*** *(1986) 282*

Itikawa Y and Mason N

Journal of Physical and Chemical Reference Data ***34*** *(2005) 1*

Jain A *Journal of Physics B: Atomic Molecular and Optical Physics* ***21*** *(1988) 905*

Johnson L K, Gao R S, Smith K A and Stebbings R F

Physical Review A ***38*** *(1988) 2794*

Jung K, Antoni Th, Müller R, Kochem K-H and Ehrhardt H

Journal of Physics B: Atomic Molecular and Optical Physics ***15*** *(1982) 3535*

Kakimoto M, Hyodo T, Chiba T, Akahane T and Chang T B

Journal of Physics B: Atomic Molecular and Optical Physics **20** *(1987) L107*

Kakimoto M, Hyodo T and Chang T B

Journal of Physics B: Atomic Molecular and Optical Physics **23** *(1990) 589*

Karwasz G P, Barozzi M, Brusa R S and Zecca A

Nuclear Instruments and Methods in Physics Research B **192** *(2002) 157*

Kauppila W E, Stein T S and Jesion G *Physical Review Letters* **36** *(1976) 580*

Kauppila W E, Stein T S, Smart J H, Dababneh M S, Ho Y K, Downing J P and Pol V

Physical Review A **24** *(1981) 725*

Kauppila W E and Stein T S *Comparison of Positron and Electron Scattering by Gases (Academic Press Inc.) (1990)*

Khatri R, Charlton M, Sferlazzo P, Lynn K G, Mills A P Jr. and Roellig L O

Applied Physics Letters **57** *(1990) 2374*

Khriplovich I B and Yelkhovsky A S *Physics Letters B* **246** *(1990) 520*

Kimura M, Sueoka O, Hamada A and Itikawa Y

Advanced Chemical Physics **111** *(2000) 537*

Kimura M, Sueoka O, Makochekanwa C, Kawate H and Kawada M

Journal of Chemical Physics **115** *(2001) 7442*

Kinzer R L, Milne P A, Kurfess J D, Strickman M S, Johnson W N and Purcell W R

The Astrophysical Journal **559** *(2001) 282*

Klein M L and Venables J A *Rare Gas Solids (Academic Press 1977) ch. 10*

Klemperer O *Proceedings of the Cambridge Philosophical Society* **30** *(1934) 347*

Knudsen H and Reading J F *Physics Reports* **212** *(1992) 107*

Kögel G, Schödlbauer D, Triftshäuser W and Winter J

Physical Review Letters **60** *(1988) 1550*

Kövér A, Laricchia G and Charlton M *Materials Science Forum* **105-110** *(1992)1919*

Kövér Á, Laricchia G and Charlton M

Journal of Physics B: Atomic Molecular and Optical Physics **26** *(1993) L575*

Kövér A, Laricchia G and Charlton M

Journal of Physics B: Atomic Molecular and Optical Physics **27** *(1994) 2409*

Kövér Á and Laricchia G *Physical Review Letters* **80** *(1998) 5309*

Kövér A, Laricchia G and Finch R

Nuclear Instruments and Methods in Physics Research B **143** *(1998) 100*

Kövér A and Laricchia G *Measurement Science and Technology* **12** *(2001) 1875*

Kövér A, Paludan K and Laricchia G

Journal of Physics B: Atomic Molecular and Optical Physics **34** *(2001) L219*

Kwan Ch K, Hsieh Y-F, Kauppila W E, Smith S J, Stein T S, Uddin M N and

Dababneh M S *Physical Review A* **39** *(1989) 2752*

Kwan Ch K, Kauppila W E, Lukaszew R A, Parikh S P, Stein T S, Wan Y J and

Dababneh M S *Physical Review A* **44** *(1991) 1620*

Laricchia G and Zafar N *Solid State Phenomena* **28 & 29** *(1992) 347*

Laricchia G, Zafar N, Charlton M and Griffith T C

Hyperfine Interactions **73** *(1992) 133*

Laricchia G, Armitage S, Leslie D E, Szłuińska M and Van Reeth P

Radiation Physics and Chemistry **68** *(2003) 21*

Laricchia G, Armitage S and Leslie D E

Nuclear Instruments and Methods in Physics Research B **221** *(2004) 60*

Leslie D E, Armitage S and Laricchia G

Journal of Physics B: Atomic Molecular and Optical Physics **35** *(2002) 4819*

Leslie D E *PhD Thesis (2005) University College London*

Leventhal M *American Journal of Physics* **60** *(1992) 856*

Lindsay B G and Mangan M A *Photon and Electron Interactions with Atoms, Molecules and Ions, Landolt-Bornstein I/17C (2003) (New York: Springer)*

Linert I and Zubek M *Chemical Physics Letters* **429** *(2006) 395*

Lucas M W and Harrison K G

Journal of Physics B: Atomic Molecular and Optical Physics **5** *(1972) L20*

Lucas M W and Steckelmacher W *Lecture Notes in Physics: Proceedings of the 3rd Workshop on High-Energy Ion-Atom Collisions* **294** *(1988) 229*

Ludlow J and Walters H R J '*Many-Particle Spectroscopy of Atoms, Molecules, Clusters, and Surfaces' eds. Berakdar J and Kirschner J (Kluwer, New York) (2001) 319*

Lynn K G, Frieze W E and Schultz P J *Physical Review Letters* **52** *(1984) 1137*

Maerk T D and Dunn G H *Electron Impact Ionization (1985) (Wien: Springer Verlag)*

Mandal P, Roy K and Sil N C *Physical Review A* **33** *(1986) 756*

Massoumi G R, Hozhabri N, Lennard W N, Schultz P J, Baert S F, Jorch H H and Weiss A H *Review of Scientific Instruments* **62** *(1991) 1460*

McAlinden M T, MacDonald F G R S and Walters H R J

Canadian Journal of Physics **74** *(1996) 434*

Middleton A G, Teubner P J O and Brunger M J

Physical Review Letters **69** *(1992) 2495*

Mills A P Jr., Platzman P M and Brown B L *Physical Review Letters* **41** *(1978) 1076*

Mills A P Jr. and Gullikson E M *Applied Physics Letters* **49** *(1986) 1121*

Milne P A *New Astronomy Reviews* **50** *(2006) 548*

Milstein A I and Khriplovich I B *JETP* **79** *(1994) 379*

Mitroy J and Ivanov I A *Physical Review A* **65** *(2002) 012509*

Mitroy J and Bromley M W J *Physical Review A* **67** *(2003) 034502*

Mitroy J and Novikov S A *Physical Review Letters* **90** *(2003) 183202*

Mohorovicic S *Astronomische Nachrichten* **253** *(1934) 94*

Moxom J, Laricchia G, Jones G O, Charlton M and Kövér A

Journal of Physics B: Atomic Molecular and Optical Physics **25** *(1992) L613*

Moxom J, Ashley P and Laricchia G *Canadian Journal of Physics* **74** *(1996) 367*

Murray C A and Mills A P Jr. *Solid State Communications* **34** *(1980) 789*

Nagashima Y, Kakimoto M, Hyodo T, Fujiwara K, Ichimura A, Chang T, Deng J, Akahane T, Chiba T, Suzuki K, McKee B T A and Stewart A T

Physical Review A **52** *(1995) 258*

Nagashima Y, Hyodo T, Fujiwara K and Ichimura A

Journal of Physics B: Atomic Molecular and Optical Physics **31** *(1998) 329*

Newman J H, Chen Y S, Smith K A and Stebbings R F

Journal of Geophysical Research **91** *(1986) 8947*

Okamoto Y, Onda K and Itikawa Y

Journal of Physics B: Atomic Molecular and Optical Physics **26** *(1993) 745*

Ott B *Contemporary Physics* **44** *(2003) 1*

Özen A, Garner A J and Laricchia G

Nuclear Instruments and Methods in Physics Research B **171** *(2000) 172*

Palathingal J C, Asoka-Kumar P, Lynn K G, Posada Y and Wu X Y

Physical Review Letters **67** *(1991) 3491*

Paul J *Nuclear Instruments and Methods in Physics Research B* **221** *(2004) 215*

Perkins A and Carbotte J P *Physical Review B* **1** *(1970) 101*

Petkov M P, Lynn K G and Roellig L O

Journal of Physics: Condensed Matter **8** *(1996) L611*

Petkov M P, Lynn K G, Roellig L O and Troev T D

Applied Surface Science **116** *(1997) 13*

Proca G A and Green T S *Review of Scientific Instruments* **41** *(1970) 1778*

Proca G A *Review of Scientific Instruments* **44** *(1973) 1365*

Proca G A *Review of Scientific Instruments* **44** *(1973) 1376*

Proca G A and Rüdinger C *Review of Scientific Instruments* **44** *(1973) 1381*

Ramsauer C *Annalen der Physik* **369** *(1921) 513*

Ramsauer C *Annalen der Physik* **377** *(1923) 345*

Ramsauer and Kollath *Annalen der Physik* **395** *(1929) 536*

Ray H *Journal of Physics B: Atomic Molecular and Optical Physics* **35** *(2002) 3365*

Rødbro M and Anderson F D

Journal of Physics B: Atomic Molecular and Optical Physics **12** *(1979) 2883*

Ruark A E *Physical Review* **68** *(1945) 278*

Rudd M E, Goffe T V, DuBois R D and Toburen L H

Physical Review A **31** *(1985) 492*

Sağlam Z and Aktekin N

Journal of Physics B: Atomic Molecular and Optical Physics **23** *(1990) 1529*

Saito F, Nagashima Y and Hyodo T

Journal of Physics B: Atomic Molecular and Optical Physics **36** *(2003) 4191*

Saito H and Hyodo T *Physical Review Letters* **97** *(2006) 253402*

Sarkadi L *Physical Review A* **68** *(2003) 032706*

Sarkadi L and Barrachina R O *Physical Review A* **71** *(2005) 062712*

Schultz D R and Reinhold C O

Journal of Physics B: Atomic Molecular and Optical Physics **23** *(1990) L9*

Schultz D R, Olson R E and Reinhold C O

Journal of Physics B: Atomic Molecular and Optical Physics **24** *(1991) 521*

Schultz P J and Lynn K G *Reviews of Modern Physics* ***60*** *(1988)* 701

Shah M B, McGrath C, Illescas C, Pons B, Riera A, Luna H, Crothers D S F, O'Rourke S F C and Gilbody H B *Physical Review A* ***67*** *(2003) 010704*

Shearer J W and Deutsch M *Physical Review* ***76*** *(1949) 462*

Shinohara N, Suzuki N, Chang T and Hyodo T *Physical Review A* ***64*** *(2001) 042702*

Shyn T W and Sweeney C J *Physical Review A* ***47*** *(1993) 1006*

Sil N C, Roy K and Mandal P *Proceedings of the 17th International Conference on the Physics of Electronic and Atomic Collisions, Brisbane (Bristol, Hilger) (1991) 354*

Skalsey M, Engbrecht J J, Bithell R K, Vallery R S and Gidley D W *Physical Review Letters* ***80*** *(1998) 3727*

Skalsey M, Engbrecht J J, Nakamura C M, Vallery R S and Gidley D W *Physical Review A* ***67*** *(2003) 022504*

Sparrow R A and Olson R E *Journal of Physics B: Atomic Molecular and Optical Physics* ***27*** *(1994) 2647*

Starrett C, McAlinden M T and Walters H R J *Physical Review A* ***72*** *(2005) 012508*

Stein T S, Kauppila W E, Pol V, Smart J H and Jesion G *Physical Review A* ***17*** *(1978) 1600*

Stein T S, Jiang J, Kauppila W E, Kwan Ch K, Li H, Surdutovich A and Zhou S *Canadian Journal of Physics* ***74*** *(1996) 313*

Sueoka O and Mori S *Journal of Physics B: Atomic Molecular and Optical Physics* ***19*** *(1986) 4035*

Sullivan J P, Gilbert S J, Buckman S J and Surko C M *Journal of Physics B: Atomic Molecular and Optical Physics* ***34*** *(2001) L467*

Sullivan J P, Gilbert S J, Marler J P, Greaves R G, Buckman S J and Surko C M *Physical Review A* ***66*** *(2002) 042708*

Surko C M, Gribakin G F and Buckman S J

Journal of Physics B: Atomic Molecular and Optical Physics **38** *(2005) R57*

Szmytkowski C *Chemical Physics Letters* **136** *(1987) 363*

Taylor F W *Reports on Progress in Physics* **65** *(2002) 1*

Tinetti G, Vidal-Madjar A, Liang M-Ch, Beaulieu J-P, Yung Y, Carey S, Barber R J, Tennyson J, Ribas I, Allard N, Ballester G E, Sing D K and Selsis F

Nature **448** *(2007) 169*

Tong B Y *Physical Review B* **5** *(1972) 1436*

Townsend J S and Bailey V A *Philosophical Magazine* **43** *(1922) 593*

Trajmar S, Cartwright D C and Williams W *Physical Review A* **4** *(1971) 1482*

Vallery R S, Zitzewitz P W and Gidley D W *Physical Review Letters* **90** *(2003) 20*

Wallace L, Bernath P, Livingston W, Hinkle K, Busler J, Guo B and Zhang K

Science **268** *(1995) 1155*

Walters H R J *Private Communication (2004)*

West R N *Advances in Physics* **22** *(1973) 263*

Wheeler J A *Annals of the New York Academy of Sciences* **48** *(1946) 221*

Yang C N *Physical Review 77 (1950) 242*

Yuan J and Zhang Z *Physical Review A* **45** *(1992) 4565*

Zafar N, Chevallier J, Jacobsen F M, Charlton M and Laricchia G

Applied Physics A-Materials Science & Processing **47** *(1988) 409*

Zafar N, Chevallier J, Laricchia G and Charlton M

Journal of Physics D: Applied Physics **22** *(1989) 868*

Zafar N *PhD Thesis (1990) University College London*

Zafar N, Laricchia G, Charlton M and Griffith T C

Journal of Physics B: Atomic Molecular and Optical Physics **24** *(1991) 4661*

Zafar N, Laricchia G, Charlton M and Garner A J

Physical Review Letters **76** *(1996) 1595*

Zecca A, Karwasz G, Oss S, Grisenti R and Brusa R

Journal of Physics B: Atomic Molecular and Optical Physics **20** *(1987) L133*

Zecca A, Sanyal D, Chakrabarti M and Brunger M

Journal of Physics B: Atomic Molecular and Optical Physics **39** *(2006) 1597*

Zhou S, Li H, Kauppila W E, Kwan C K and Stein T S

Physical Review A **55** *(1997) 361*